UCL Université catholique de Louvain

École polytechnique de Louvain (EPL)

Physical aspects of the artificial ovary

Characterization of human ovarian tissue and fibrin scaffolds

Dissertation presented by
Lucie MORTIAUX

for obtaining the Master's degree in
Biomedical Engineering

Supervisors
Christiani AMORIM , Sophie DEMOUSTIER

Readers
Evelyne VAN RUYMBEKE, Christine DUPONT

Academic year 2015-2016

Abstract

While the number of girls and young women reached by cancer increases year upon year, improvements in cancer treatments allow to cure most of them. However, these treatments can result in premature ovarian failure. To solve this problem, several fertility preservation and restoration techniques are already available. Nevertheless, for patients at prepubertal stage or that cannot postpone their cancer treatment, cryopreservation and transplantation of ovarian tissue is the only available option. Eventhough this technique has shown to be successful, it is not advisable for patients with certain types of cancer, since there is a risk of reintroducing malignant cells present in the cryopreserved tissue, which could lead to the recurrence of the primary disease. For these patients, research teams worldwide have been working on the development of a transplantable artificial ovary, which consists in the encapsulation of isolated ovarian preantral follicles and cells by a 3D matrix.

As this matrix should ideally mimic the natural human ovary, the goal of the present study is to characterize and compare the morphological and physical properties of both human ovary and the matrix that yielded best results so far, i.e., fibrin. To this end, samples of human ovarian cortex and different fibrin formulations (F12.5/T1, F30/T50, F50/T50 and F75/T75) were analyzed using a scanning electron microscope and a shear rheometer. According to these analyzes, the fibrin hydrogels made of 30 mg/ml fibrinogen and 50 U/ml thrombin showed to be the most similar to human ovarian tissue and therefore seem to be the best candidate to encapsulate isolated preantral follicles.

Acknowledgements

This page is dedicated to all the persons that helped me during this year, and without which this work would not have been achieved.

First, I would like to thank Marie-Madeleine Dolmans for allowing me to perform my master thesis in GYNE laboratory, along with the research team members for their warm welcome, kindness and sens of humor. In particular, I also thank Diego Manavella for accompanying me to the slaughterhouse, which was quite an experience!

Secondly, I would like to thank my promotors, Sophie Demoustier and Christiani Amorim. Sophie Demoustier, for her disponibility, advices and encouragements toward this master thesis, which initially seemed quite challenging. And Christiani Amorim, for accepting me in her working team, for her kindness and patience considering my tons of questions all year long, and for teaching me all I needed to know about the artificial ovary, being a complete discovery for me.

I am also very grateful toward Costanza Maria Chiti, for all the time that she took for showing me how to perform biological experiments, and for answering all my questions with patience. I would also like to thank her for her daily good mood, positivism and kindness.

Moreover, I would like to thank Evelyne van Ruymbeke for allowing me to perform rheological tests in her lab, but more particularly, for her kindness, disponibility and precious advices. Indeed, without Mrs. van Ruymbeke and her strong compe-

tences in rheology, this innovative study would never have been possible. Along with her, I am very grateful toward Flanco Zhuge for all the hours that he took for teaching me everything about rheology, as it was, once more, completely new for me, and for answering all my questions.

I would also like to thank Delphine Magnin for communicating to me her strong skills regarding the SEM, for her precious advices, disponibility and sens of humor. Along with her, I would like to thank Pascale Lipnik and Loic Germain for their help, time and advices.

I thank all jury members for the time they will spend reading my work: Christiani Amorim, Sophie Demoustier, Evelyne van Ruymbeke and Christine Dupont.

Last but not least, I would like to thank my family and friends for their support all year long and, especially my parents and grandma for encouraging me during those five years. Thank you for listening to me talking about ovaries during a all year, without complaining!

Contents

List of abbreviations

#Pt./dec	**Number** of **P**oints **Per** **D**ecade
3D	**Three**-**D**imensional
AS	**A**mplitude **S**weep
AS[x2]	**Double** **A**mplitude **S**weep
AMH	**A**nti-**M**üllerian **H**ormone
Col	**Col**lagen
De	**De**borah number
COS	**C**ontrol **O**varian **S**timulation
DMSO	**Dim**ethyl **S**ulf**o**xide
DOM	**D**ecellularized **O**varian extracellular **M**atrix
CPD	**C**ritical **P**oint **D**rying/**D**ryer
ECM	**E**xtra**C**ellular **M**atrix
F100	**F**ibrinogen solution of concentration **100** mg/ml
FR	**F**irst **R**ound
FS	**F**requency **S**weep
FSH	**F**ollicle-**S**timulating **H**ormone
G	α-L-**G**uluronate
IVF	**I**n **V**itro **F**ertilization
LH	**L**uteinizing **H**ormone
LP	**L**ast **P**oint
M	β-D-**M**annuronate
MEM	**M**inimal **E**ssential **M**edium
NA	**N**on **A**pplicable
NGF	**N**on-**G**rowing **F**ollicles

PBS	**P**hosphate-**B**uffered **S**aline
PEG	**P**oly**E**thylene **G**lycol
POF	**P**remature **O**varian **F**ailure
RT	**R**oom **T**emperature
SEM	**S**canning **E**lectron **M**icroscopy/**M**icroscope
SR	**S**econd **R**ound
T500	**T**hrombin solution of concentration **500** U/ml
TAO	**T**ransplantable **A**rtificial **O**vary
TS	**T**emperature **S**weep

List of symbols

Ar	Argon	/
Au	Gold	/
Ca^{+2}	Calcium cation	/
$CaCl_2$	Calcium chloride	/
CO_2	Carbon dioxide	/
Cr	Chromium	/
CrO	Chromium oxide	/
δ	Phase angle	[°]
F	Fibrinogen	[mg/ml]
G'	Elastic/Storage modulus	[Pa]
G''	Viscous/Loss modulus	[Pa]
γ	Shear strain	[%]
$\dot{\gamma}$	Shear rate	$[s^{-1}]$
M	Mole per liter	[mol/l]
η	Viscosity	[Pa.s]
$NaCl$	Sodium chloride	/
OsO_4	Osmium tetraoxide	/
p_c	Critical pressure	[bar]
T	Thrombin	[U/ml]
T_c	Critical temperature	[°C]
τ	Shear stress	[Pa]
τ_{obs}	Observation time	[s]
τ_{rel}	Relaxation time	[s]
ω	Frequency	[rad/s]

Chapter 1

Introduction

While the number of children, adolescents and young adults affected by cancer increases year upon year, the number of patients dying from the disease continues to fall. Indeed, chemo/radiotherapeutic treatments are becoming more and more effective, but the collateral damage of this improvement is their negative impact on fertility in cancer survivors, causing loss of both endocrine and reproductive functions. It is widely acknowledged that such treatments often decrease the ovarian reserve and trigger early menopause. [1, 2, 3]

For female patients, a number of fertility preservation and restoration strategies are available, depending on the type of malignancy, patient age, relationship status and administered treatment. Nevertheless, when gonadotoxic treatment cannot be delayed or in prepubertal girls, ovarian tissue cryopreservation and transplantation constitutes the only option to preserve and restore fertility. This technique has resulted in more than 60 successful pregnancies to date [4]. However, it cannot be used in some types of cancer because of the risk of reimplanting malignant cells, which could lead to recurrence of the primary disease. Table 1.1 shows the risk of ovarian involvement in different types of cancer. [1, 2]

For patients affected by such moderate- to high-risk cancers, no solution is currently available to restore their fertility. For this reason, research teams have been working on two different strategies, namely in vitro maturation and construction of a transplantable artificial ovary (TAO). Since it is believed that long periods of in vitro culture required to grow follicles could interfere with epigenetic mechanisms,

and particularly genomic imprinting, the attention has been focused primarily on development of the TAO. However, in order to create this artificial organ, the first step is to understand some important physical aspects of the natural human ovary. [1, 2]

The goal of the present study was therefore to assess the properties of the natural human ovary and attempt to mimic these characteristics in a suitable matrix that would replace the natural organ. To do so, this master thesis is composed of two parts, namely, the theoritical background and the experimentation. The first one covers all the notions necessary to tackle the experimental one, including chapters on the natural ovary, techniques of fertility preservation and restoration and on the transplantable artificial ovary. Besides, as introduction to the experimental work, a chapter is devoted to the description of the technical instruments and techniques used in this study. As this work stands between the medical and engineering worlds, and considering the jury composition of this master thesis, some informations may seem obvious or pointless for you, for that I apologize in advance.

High risk (>11%)	Leukemia
	Neuroblastoma
	Burkitt lymphoma
Moderate risk (0.2-11%)	Breast cancer (stage IV infiltrating lobular subtype)
	Colon cancer
	Adenocarcinoma of the cervix
	Non-Hodgkin's lymphoma
	Ewing sarcoma
Low risk (<0.2%)	Breast cancer (stage I-II infiltrating ductal subtype)
	Squamous cell carcinoma of the cervix
	Hodgkin's lymphoma
	Osteogenic carcinoma
	Non-genital rhabdomyosarcoma
	Wilms' tumor

Table 1.1: Risk of ovarian metastasis according to cancer. Table adapted from [5].

Part I

Theoretical Background

Chapter 2

The natural ovary

In order to create a more suitable TAO, it is necessary to know, as much as possible, the characteristics of the human natural ovary, to better mimic it. Therefore, before plunging in the principal subject of this study, here is a summary of what is known about the structure and functions of the natural human ovary, the ovarian reserve and the folliculogenesis.

2.1 Structure and functions

The female body is provided with two ovaries located on either side of the uterus within the ovarian ligaments (Fig. 2.1) and next to the Fallopian tubes.

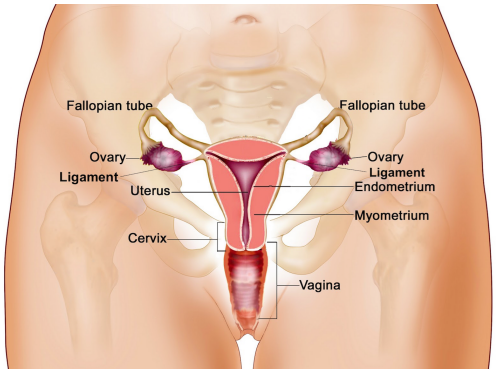

Figure 2.1: Female reproductive anatomy. [6]

These small oval organs ($\sim$5×4×1.5 cm^3) have two major functions, one endocrine and another exocrine: the production of sex hormones and the oogenesis

(storage and development of the follicles and releasing of ova), respectively. Indeed, the ovarian hormones are very important, not only for the reproductive function, but also for other parts of the body, like skin, bones, breast, vessels and other endrocrine tissues. Those two functions are regulated via pituitary gonadotropic hormones: the luteinizing hormone (LH) and the follicle-stimulating hormone (FSH). [3, 7, 8, 9, 10, 11]

Ovaries are basically composed of follicles at different stages of development and their surrounding environment, called the extracellular matrix (ECM). This matrix varies in composition and cells according to growth factors, cells and hormones activity. The ovaries are also organized into two parts, an internal one, the medulla, and an external one, the cortex (Fig. 2.2). Those regions have different structures and compositions but also different roles. Indeed, the central medulla exhibits a random organization and is full of blood and lymphatic vessels, nerves, collagen and embryologic remnants. This soft structure plays more a role of supply for the ovary. On the other hand, the ovarian cortex is less vascularized but more dense and is also collagen-rich, full of follicles at different stages of development and stromal cells. This more rigid region plays an important role in the survival and growth of the follicles. [3, 7, 8, 9, 10, 11]

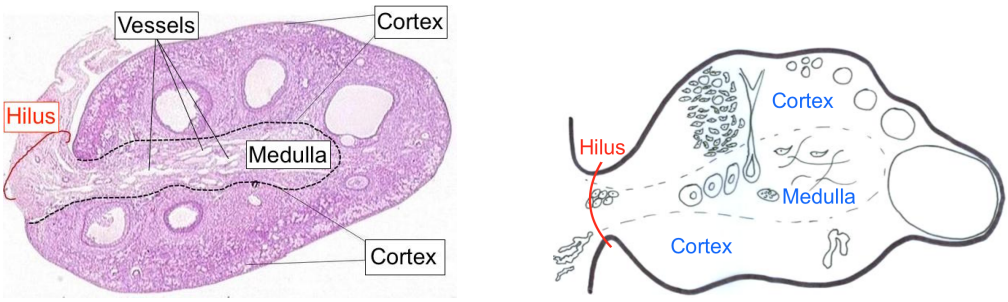

(a) (b)

Figure 2.2: Structure of a human ovary showed in a (a) histological slide [12] and (b) schematic representation [10]. The two sections are clearly visible namely the internal part (the medulla) dotted with vessels and linked to the hilus and the external one (the cortex).

Finally, the functional unit of the ovary is the follicle. Its structure and composition depends on its stage of development, but this small rond structure is at least

composed of an oocyte (the female gamete) and somatic cells. These differentiation steps occur during the folliculogenesis. This mecanism is explained in a later section (section 2.3). [3, 7, 8, 9, 10, 11]

2.2 The ovarian reserve

The term "ovarian reserve" refers to the stock of female reproductive cells, namely the primordial follicles and is sometimes called the "true ovarian reserve". Indeed, unlike men in whom the spermatozoids are continually produced and during all their life, the female reproductive organ contains a fixed number of non-growing follicles (NGF), established before birth. Indeed, at mid-gestation, this reserve reaches the number of 6-7 x 10^6 of primordial follicles. However, by birth, 85% of this initial stock will be lost, leaving around 10^6 of them. From birth to puberty, they will drop to approximately 300 000. Among those remaining follicles, only 400-500 really ovulate during the reproductive life of women. The remaining follicle population undergo atresia during their growth phase. These ovulatory cycles go on until the end of the reproductive life, commonly called the menopause, in which the follicle stock is reduced to $\sim$ 1000. The evaluation of the ovarian reserve is a very important factor for patients at risk of premature ovarian failure (POF) due to cancer treatments. [5, 9, 13, 14]

Wallace and Kelsey [15] developed the first mathematical model of ovarian reserve from conception to menopause (Fig. 2.3), which shows the NGF population in the human ovaries and their rate of recruitment.

2.3 Folliculogenesis

Folliculogenesis is a complex process regulated by endocrine, paracrine and autocrine factors where a primordial follicle develops to a preovulatory one, which will either ovaluate a fertilizable occyte (in less than 0.1% of the cases) or will undergo atresia (in 99.9% of the cases) [3, 9, 11]. The folliculogenesis takes around 200 days and

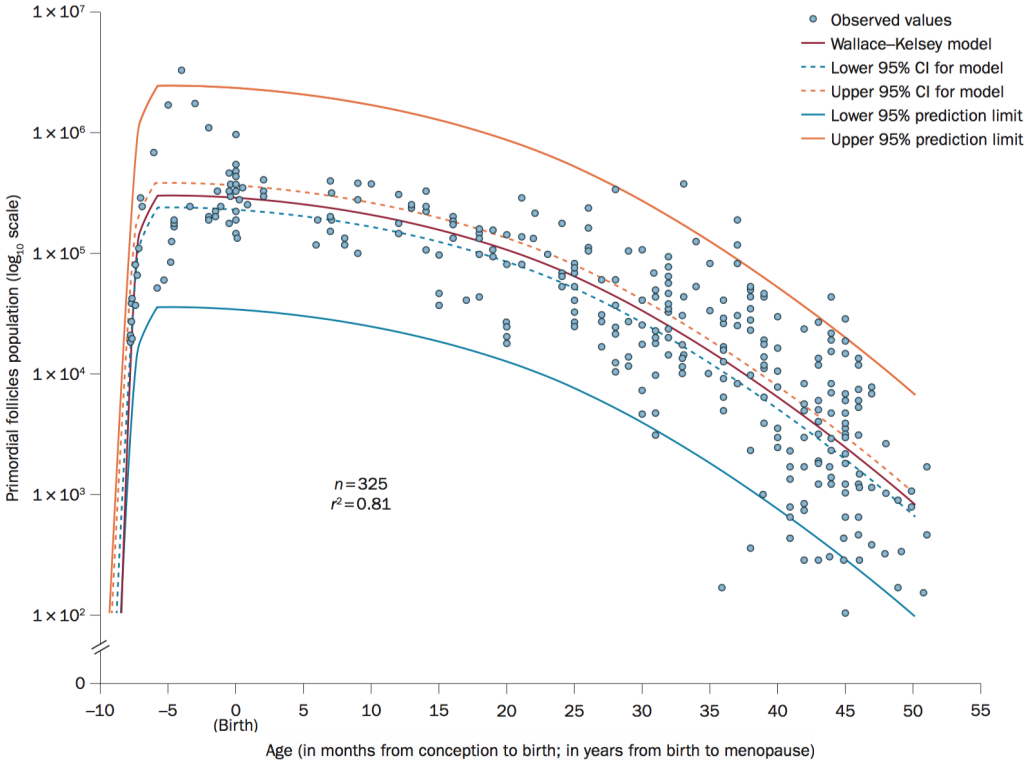

Figure 2.3: Mathematical model computing the human ovarian reserve from conception to menopause. Number of non-growing follicles population in logarithmic scale versus age (in months from conception to birth and in years from birth to menopause). Figure adapted from [5, 15].

can be divided in different steps: [9]

1. Formation of primordial follicles,
2. Recruitment of primordial follicles from the ovarian reserve,
3. Follicle growth,
4. Selection and maturation of the preovulatory follicle,
5. Ovulation of the dominant follicle.

The following sections describe in details each one of these steps.

2.3.1 Formation of primordial follicles

The first stage of folliculogenesis is the formation of primordial follicles and, in humans, takes place during the fetal development. Some of these follicles start to grow almost immediately while the majority remain quiescent. Primordial follicles

(Fig. 2.4) have a diameter around 35 μm. They are composed of a single oocyte surrounded by a pregranulosa layer envelopped in a basal lamina in order to separate the follicle from the surrounding cells, blood vessels and nerves. [9]

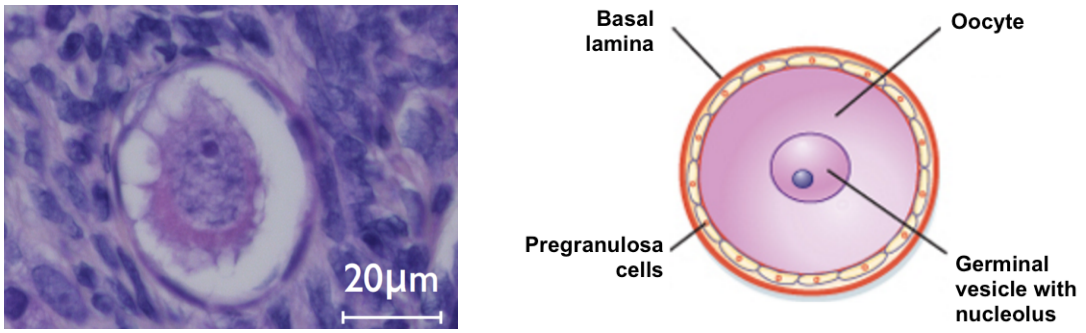

(a) (b)

Figure 2.4: Structure of a human primordial ovarian follicle composed of an oocyte and flattened granulosa cells envelopped in a basal lamina showed in a (a) histological slide [9] and (b) schematic representation [16].

2.3.2 Recruitment of primordial follicles

The recruitment of primordial follicles, also called primordial follicle activation, is the process by which a dormant follicle of the ovarian reserve is activated and enters the pool of growing follicles. The mecanisms controlling this activation process remain elusive but seem to be under the control of both inhibitory and stimulatory signals. Indeed, locally produced factors might promote this follicle transition from primordial to primary, while anti-Müllerian hormone (AMH) secreting by adjacent growing follicle might negatively regulate it. Finally, it is important to keep in mind that ovarian follicles are continually recruited from fetal life to menopause. [9, 17]

2.3.3 Follicle growth

The majority of the NGF lie in the ovarian cortex and will progressively move from the cortex toward the medulla during their growth. After their recruitment, primordial follicles will turn into primary, then into secondary and finally into antral follicle and complete their development at the ovarian surface or undergo atresia. The different stages of follicle development are described as follows. [17]

Primary stage

Once the selected primordial follicle is activated, its oocyte begins to enlarge, surrounded by a zona pellucida newly formed. The pregranulosa layer transforms into a single layer of cuboidal granulosa cells. This implies a global increasing of the follicle size from 35 to approximately 46 μm, due to protein synthesis and organelle multiplication. Those transformations give rise to a primary follicle (Fig. 2.5). [9, 13]

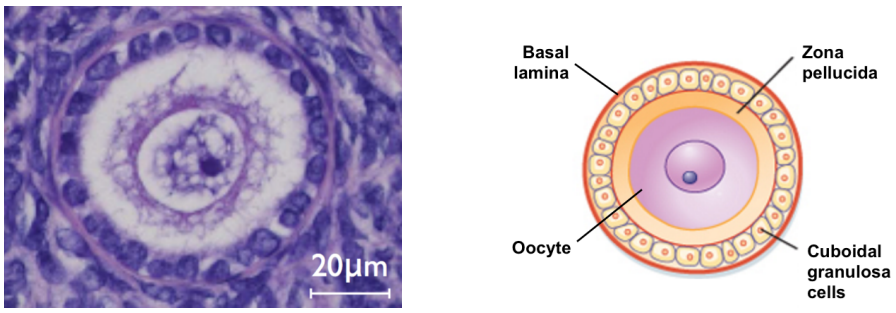

(a) (b)

Figure 2.5: Structure of a human primary ovarian follicle composed of an oocyte, a zona pellucida and a membrane of cuboidal granulosa cells showed in a (a) histological slide [9] and (b) schematic representation [16].

A major consequence of this follicular development is the formation of intercellular connections between the oocyte and the granulosa cells, allowing the diffusion of ions, metabolites and signaling molecules. These gap junctions are essential for further follicular development. [9]

Secondary stage

The next stage of development is the secondary follicle (Fig. 2.6), measuring around 120-200 μm. This transition implies the division of the granulosa cells, which organize themselves in multiple layers. At this stage, it is also possible to observe the development of a supplementary layer of cells, called the theca. As the follicle size increases, this theca stratifies and differentiates in two distinct parts composed of cells of different nature: an outer one, called the theca externa and an inner one, called the theca interna. Besides, compared to earlier stages, a capillary network

is formed just outside the basal lamina in order to provide blood supply to the secondary follicle. [9]

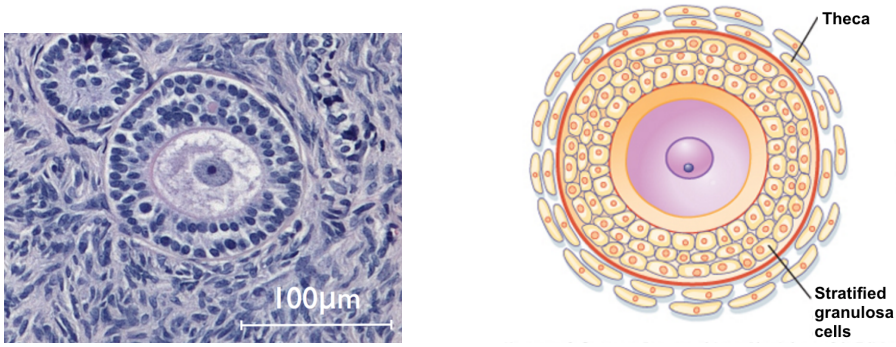

(a) (b)

Figure 2.6: Structure of a human secondary ovarian follicle composed of an oocyte, a zona pellucida, stratified granulosa cells and of a theca showed in a (a) histological slide [9] and (b) schematic representation [16].

Antral stage

From the primordial to secondary stage, follicles can be also classified as preantral. Once the follicles start developing a cavity containing follicular fluid, called antrum, they can be defined as antral follicles (Fig. 2.7), which measure around 0.2-5 mm. Antral follicles are then classified into tertiary, containing small antral cavities that will progressively form a single large one, and at this point, the follicle is called preovulatory. This fluid is very important for follicular development as it contains water, electrolytes, serum proteins and high concentrations of steroid hormones. As represented on figure 2.7(b), with further follicle development, granulosa cells surrounding the oocyte form a cluster of cells called the cumulus. [9]

2.3.4 Selection and maturation of the preovulatory follicle

Most follicles reaching the antral stage will undergo atresia, while the remaining part will survive and grow to the next stage, namely, the preovulatory follicle. The process of selection of the dominant follicle is still under debate, but there is increasing evidences suggesting the recruitment of multiple cohorts of antral follicles during each menstrual cycle, along with the rise in circulating FSH concentration. This selection process will end up with the choice of a dominant follicle, which will

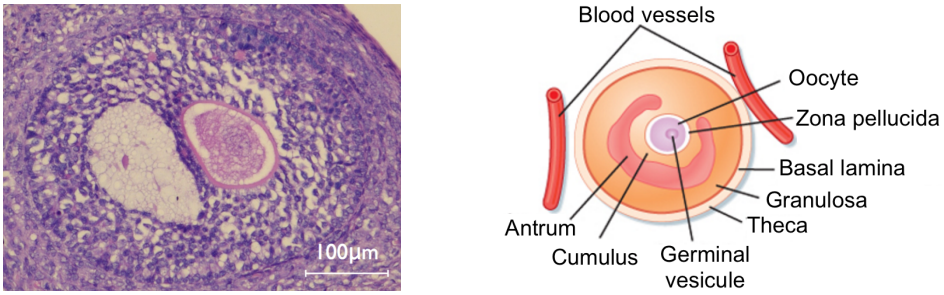

(a) Histological slide. [9] (b) Schematic representation. [16]

Figure 2.7: Structure of a human antral ovarian follicle composed of an oocyte, a zona pellucida, a small antrum, granulosa and cumulus cells, a theca and surrounded by a capillary network showed in a (a) histological slide [9] and (b) schematic representation [16].

grow and become the only ovulatory follicle. Besides, suppositions are made about the fact that each preovulatory follicle possesses a FSH threshold that must be surpassed in order to pursue its development. Those follicles are found in the ovary at any time during the menstrual cycle. [9]

The dominant follicle (Fig. 2.8) will thus grow and undergo morphological changes, such as its enlargement up to 20 mm in diameter (at this moment, the follicle is defined as mature) due to granulosa cells proliferation, theca cells vascularization and further fluid accumulation in the antrum. This mature follicle is also commonly called the Graafian follicle. [9]

2.3.5 Ovulation of the dominant follicle

When this preovulatory follicle becomes mature and that a LH surge occurs (depending on the menstrual cycle), the ovulation is triggered, causing the oocyte expulsion in the Fallopian tube (Fig. 2.9(a)). During this step, the oocyte undergoes several modifications through a process called the oocyte maturation. Following the ovulation step, the follicle walls collapse and its remnants transform into the corpus luteum, a hormone secretion unit (Fig. 2.9(b)). [9]

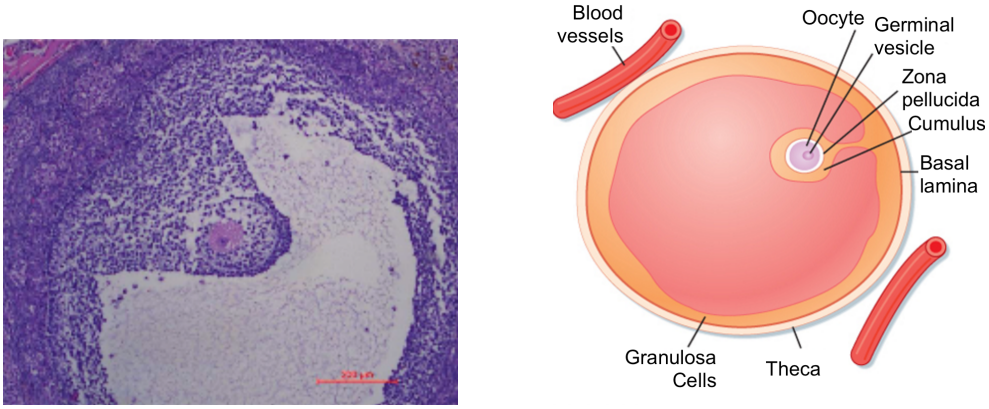

(a) Histological slide. [9] (b) Schematic representation. [16]

Figure 2.8: Structure of a human preovulatory follicle composed of an oocyte, a zona pellucida, a large antrum, granulosa and cumulus cells, a theca and surrounded by a capillary network showed in a (a) histological slide [9] and (b) schematic representation [16].

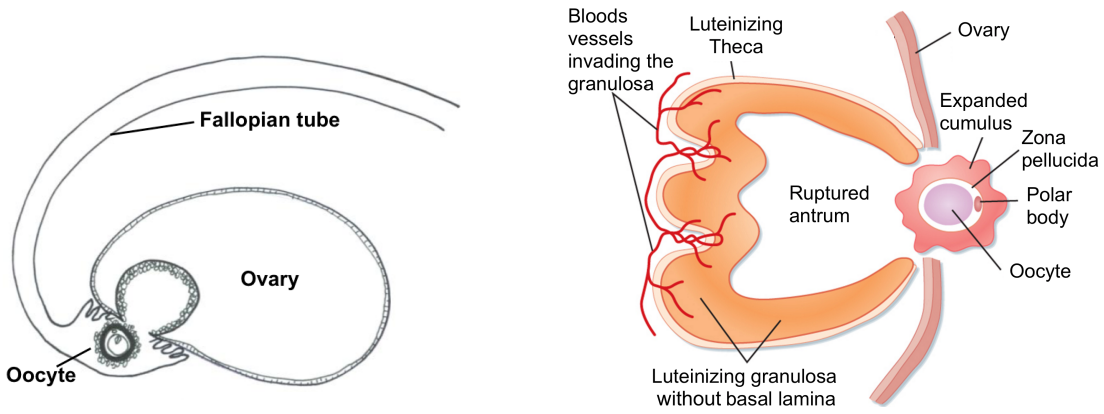

(a) (b)

Figure 2.9: Schematic representation of the ovulation process during which (a) the oocyte is expelled in the Fallopian tube [10] and (b) the remnants of the follicle are transformed in a secretory unit, called the corpus luteum [16].

Chapter 3

Fertility preservation and restoration in cancer patients

3.1 Alternatives of fertility preservation

When a patient is diagnosed with cancer, the risk of POF must first be assessed according to the required treatment. Then, the oncologist has to inform the patient about the different techniques of fertility preservation available. As previously explained, the choice of the most appropriate option depends on the age of the patient, its pubertal status, the presence or not of a partner, the administrated treatment and finally the emergency to start this treatment depending on the cancer's type. Indeed, several techniques of fertility preservation and restoration are already available (Fig. 3.1), such as ovarian transposition, embryo cryopreservation, oocyte cryopreservation or ovarian tissue cryopreservation and transplantation. [1, 5, 9]

The chosen fertility preservation alternative needs to be performed before the beginning of the treatment and might have a variable duration according to the selected technique. Indeed, embryo and mature oocytes cryopreservations can take 2-6 weeks and can thus be chosen only if the beginning of the treatment can be delayed, while ovarian transplantation along with immature oocytes and ovarian tissue cryopreservations can be immediately performed. Besides, unlike the other techniques, ovarian tissue cryopreservation is the only one that can be proposed to prepubertal girls. [1, 5, 9]

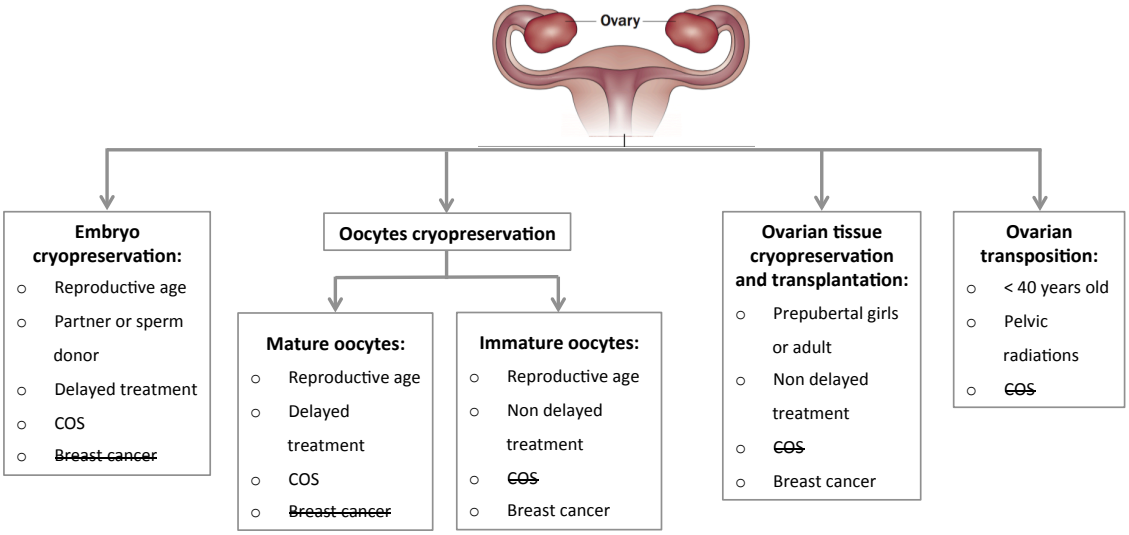

Figure 3.1: Techniques of fertility preservation and restoration in women at risk of premature ovarian failure depending on several factors, such as the age, marital and pubertal status of the patient, the cancer's type (allowing or not controlled ovarian stimulation (COS)), the cancer treatment and whether it can be delayed or not. Picture adaptated from [5].

The following sections offer an overview of all alternatives to preserve fertility in cancer female patients.

3.1.1 Ovarian transposition

Ovarian transposition corresponds to the shifting by laparoscopy of the ovaries outside of the irradiation field when pelvic radiations need to be undertaken for cancer treatment. This technique is thus advised to all patients requiring this treatment being, most of the time, patients of more than 40 years with advanced cervical cancer (Fig. 3.1). Besides, it is strongly suggested to remove a large biopsy of ovarian tissue at the same time for cryopreservation, as the risk of POF due to pelvic radiations can go from 15 to 40%. [5]

3.1.2 Embryo cryopreservation

Embryo cryopreservation is a safe and well established technique which consists in the stimulation of the ovaries with gonadotropins (glycoprotein polypeptide hormones), in order to collect mature oocytes that will then be fertilized in vitro. This

controlled ovarian stimulation (COS) has to be repeated more than once to have enough amount of mature oocytes and thus, ensure the success of the in vitro fertilization (IVF) and the sufficient number of embryos. Once the fertilization done, the embryos are cryopreserved either by slow-freezing or vitrification. [1, 5, 9, 18]

This technique is thus reserved to women of reproductive age, having an available partner (or willing to use donor sperm) and able to delay their cancer treatment of 2-6 weeks considering the time required to realize the entire process (Fig. 3.1). Besides, in case of cancers sensitive to sexual hormones stimulations, like breast cancer, this option is considered as not safe, as it can induce tumor growth acceleration. [1, 5, 9, 18]

3.1.3 Oocytes cryopreservation

Oocytes cryopreservation is similar to the embryo cryopreservation technique and can be divided into two categories, depending on the stage of the extracted oocyte, namely, mature or immature oocytes cryopreservation. [5, 9]

Mature oocytes cryopreservation uses the same COS protocol as embryo cryopreservation, excepting that no IVF is performed. Therefore, it can be proposed to all postpubertal women since there is no need of a partner nor donor sperm. Nevertheless, as this technique still requires COS, it is also not advised to patients with breast cancer or other hormone responsive cancers (Fig. 3.1). [5, 9]

In order to avoid the COS and if the adult patient cannot delay the start of its gonadotoxic cancer treatment, immature oocytes cryopreservation (Fig. 3.1) can be suggested. This second technique consists in the retrieval of immature oocytes followed by in vitro maturation (IVM) and cryopreservation. [5, 9]

3.1.4 Ovarian tissue cryopreservation and transplantation

Currently, ovarian tissue cryopreservation is the only available option for prepubertal girls and is more used than immature oocytes cryopreservation for patients who cannot postpone their cancer treatment or with hormone responsive malignancies (Fig. 3.1). The principle is to remove either one whole ovary or an ovarian biopsy

before the beginning of cancer treatment, by minimally invasive laparoscopy surgery, and then to cryopreserve it. No consensus has been reached according to the quantity of ovarian cortex that needs to be harvested. Indeed, this factor is very important and depends on the estimated risk of POF linked to the treatment, the age of the patient and the ovarian volume. Usually, 4-5 ovarian cortical biopsies of $10\times5\times1$ mm^3 are generally collected in adult patients. For young girls, an entire ovary is generally harvested considering their very small size because, even if biopsies might be sufficient due to the large follicles content, coagulation generally occurs after the surgery, inevitably damaging the cortex. [5, 7, 9]

When patients have completely recovered from their cancer, it is generally advised to wait a period of 5 years before the transplantation due to the risk of disease recurrence. Only after this time, the frozen-thawed ovarian fragments are transplanted either onto the remaining atrophic ovary if one ovary is still present, or in the peritoneal site if both ovaries have been removed. [9]

This technique does not need any COS, avoiding thus its side effects, and is even more successful in prepubertal patients as their ovarian cortex contains many more follicles.

Although this alternative has already lead to more than 60 births to date, it is important to highlight that it cannot be applied to all cancer patients, as in some types of malignancies, there is a risk of the presence of cancer cells in the ovarian tissue. Thus, in these cases, transplantation of cryopreserved ovarian tissue could reintroduce these cells, which could lead to recurrence of the primary disease. As previously mentioned, this risk depends on the cancer's type (see section 1, Table 1.1). Hence, for patients having these kind of moderate to high risk cancers, no option is available for the time being. For this reason, several research groups worldwide have been working on two novel strategies, namely the in vitro and the transplantable artificial ovary (Fig. 3.2). The goal is to avoid reintroduction of malignant cells, either by performing the whole folliculogenesis outside of the patient (in vitro artificial ovary), or by isolating the preantral follicles from cryopreserved ovarian fragments, as they are surrounded by a basement membrane, which protects them from cancer contamination. Their reimplantation (transplantable artificial

ovary) in the patient's body can be considered as a safer procedure. The following sections explain in brief these two alternatives. [7, 19, 20]

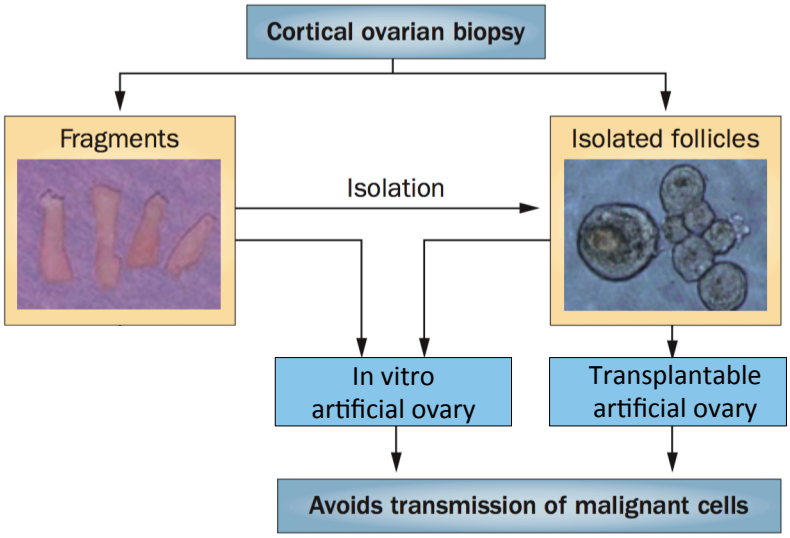

Figure 3.2: Considering the risk of reintroducing malignant cells in the patient while transplanting thawed ovarian fragments, safer alternatives need to be developed. Experimental techniques based on the reimplantation of isolated ovarian follicles have emerged, namely, the in vitro and the transplantable artificial ovary. [5]

3.1.5 In vitro artificial ovary

The concept of in vitro artificial ovary resides in cultivating primordial ovarian follicles up to the preovulatory stage. The final goal of this technology would be to obtain mature oocytes capable of producing embryos, which would then be transplanted in the mother's body. However, this process, namely the folliculogenesis, as explained in chapter 2, takes around six months in humans, is not fully understood yet and relies on both inhibitory, stimulatory and maintenance factors. Therefore, this system has never been achieved at present. Moreover, it has two main drawbacks : (1) the long period of in vitro culture and (2) the risk of interfering with epigenetic mechanisms, such as genomic imprinting. [5, 21]

3.1.6 Transplantable artificial ovary

Since ex vivo folliculogenesis is not feasible at the time being, a safer alternative would be the TAO. This technique consists in the encapsulation of the isolated

ovarian follicles into a scaffold, which would allow their survival and development. This new technology is the main subject of this study and will be fully detailled in the next chapter.

Chapter 4

Transplantable artificial ovary: development of a new technology to preserve and restore fertility

4.1 Goal

The goal of tissue engineering strategies is to replace or repair the defective organ or damaged tissue by an artificial system [9]. To do so, different aspects must be taken into account: a cellular component, a biocompatible and stable scaffold and bioactive factors to promote cells differentiation and maturation [9].

This definition is therefore applicable to the TAO. The principle of this technology is shown in Fig. 4.1.

First, fragments of ovarian tissue need to be removed and cryopreserved before cancer treatment. Then, once the patient is cured and that a period of 5 years has passed with no sign of the disease, the frozen fragments should be thawed and the follicles, isolated. These follicles are not the only cellular component that should be added to the TAO. Indeed, ovarian cells (stromal and endothelial) obtained from the remaining ovary after cancer treatment should also be grafted in order to regulate follicular growth and development. [9, 20, 21]

As previoulsy mentioned, bioactive factors, such as growth factors or hormones, could also be added to the TAO in order to regulate follicular survival and

growth. These factors could be progressively used if there were charged into micro/nanoparticles in order to control their release in time. [21]

Finally, all those elements should be put in a biocompatible and biodegradable three-dimensional (3D) matrix, which would then be grafted in the patient's remaining ovary, as described for cryopreserved ovarian tissue in chapter 3. This scaffold should also progressively degrade, while being replaced by natural structures. [9, 18, 22]

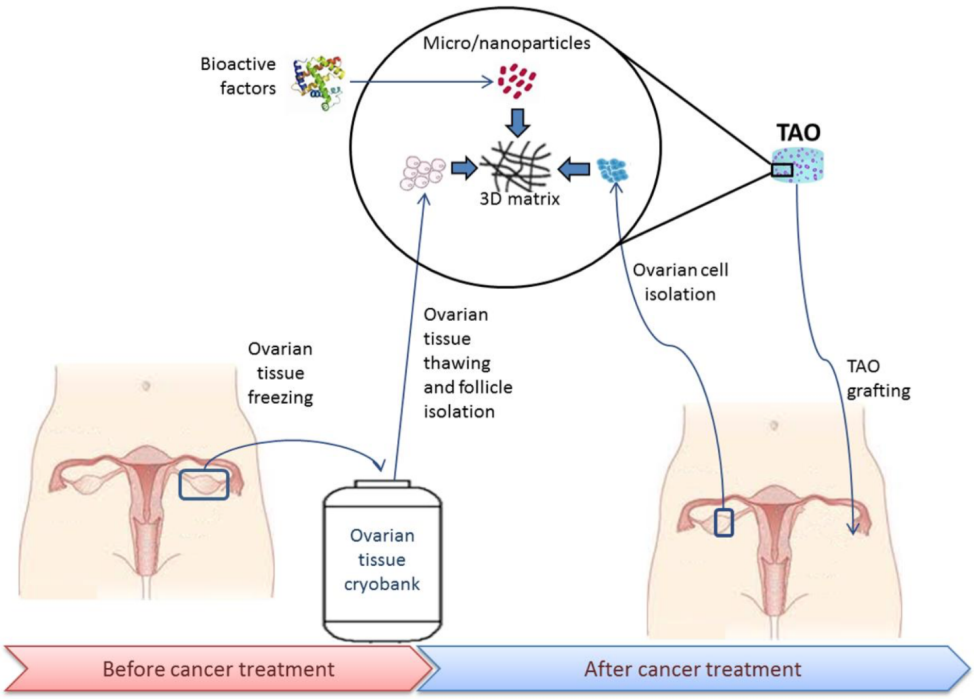

Figure 4.1: Grafting of the transplantable artificial ovary containing isolated follicles from the frozen-thawed ovarian fragments, isolated ovarian cells from the remaining ovary, bioactive factors prealably encapsulated in micro/nanoparticules and a biocompatible and biodegradable scaffold. [21]

The next sections will be devoted to the description of those three elements, namely, (1) the cellular components: the isolated human follicles and the ovarian cells, (2) the scaffold and the different matrices that have already been tested and finally, (3) the bioactive factors.

4.2 TAO biological features: cells

As mentioned above, two cellular compounds should be added in the TAO namely, the isolated human follicles, necessary for fertility function, and ovarian cells, which would help the survival and development of the implanted follicles. First, the isolation process of the human follicles will be described, followed by some explanations concerning the roles and advantages of the addition of ovarian cells aside the human follicles.

4.2.1 Isolation of human follicles

Due to the dense and fibrous nature of the human ovarian cortex, the isolation process of human preantral follicles remains, at present, quite challenging. This step is performed by mechanical dissection followed by enzymatic digestion [23]. First, the biopsies are gently cut and then incubated into a solution containing an enzyme, called the liberase, in order to digest the tissue and free the follicles. The suspension solution is pippetted several times in order to mechanically disrupt the digested tissue. The solution is then placed under a stereomicroscope and the follicles are picked up with a micropippette. [9, 24]

4.2.2 Ovarian cells

As previously mentioned, the addition of ovarian cells in the TAO is fundamental for follicles survival and development.

Ovarian stromal cells are essential for folliculogenesis to occur for many reasons: first, they help to maintain the follicles 3D structure, then they also have paracrine interactions with follicles and those adjacent to primary follicles are recruited to differentiate into theca cells, which allow androgens secretion (necessary for further follicular development). As previously cited, the stromal cells should be extracted from fresh ovarian tissue once the patient is disease-free. The reason is that, if they were extracted before cancer treatment, they should undergo malignant cell purging which is more hard-working and risky. [21]

Endothelial cells appear to be helpful for the revascularization process after

grafting, which is primordial for follicles and cells survival, as it can decrease the hypoxia period, and for the formation of an ovary-like structure. [21]

In summary, ovarian cells are likely to be added in the TAO in order to promote angiogenesis, follicular survival and development and structural support. Nevertheless, at present, no consensus has been reached according to the most appropriate amount of ovarian cells that need to be embedded in the TAO in order to ensure correct follicular development and fast neovascularization. Indeed, if only a few ovarian cells are introduced, they risk to be far apart from each other and from follicles, without correct cell-cell interactions and, on the contrary, if a large amount of cells are added, there is a risk of starving the follicles of oxygen and nutrients, leading to apoptosis. [3, 9, 21]

4.3 TAO physical properties: matrix

The TAO matrix should ideally mimic spatially and temporally the ECM of the natural ovary. Thus, it should fulfil specific criteria, such as:

- encapsulate and protect the isolated human follicles [1],
- sustain the communication between isolated human follicles and ovarian cells, in order to ensure follicular growth and development [18, 20, 21, 22],
- maintain the 3D structure of the follicles to keep the contact between all the cells and to mimic physiological conditions in order to ensure the execution of natural processes, taking place exclusively in 3D environment [18, 20, 21, 22],
- preserve the interaction between cells and ECM [18, 20, 21, 22],
- supply bioactive factors involved in follicles survival and folliculogenesis [18, 20, 21, 22],
- be biodegradable to allow neovascularization, ovarian cells proliferation and follicles growth and to be gradually replaced by an ovary-like structure. Indeed, human follicles can grow to around 600 times their initial size during folliculogenesis. Nevertheless, scaffold degradation should be neither too fast

nor too low in order to allow new tissue synthesis, cells proliferation and folliculogenesis [20, 21],

- be biocompatible in order to avoid rejection or a strong inflammatory response. Moreover, it should also degrade into biocompatible products that can be easily eliminated [22],

- be porous to promote angiogenesis and cells invasion and migration. Revascularization is a crucial process, allowing oxygen and nutrients delivery and metabolic wastes removal. Indeed, the porosity and the pores distribution and interconnectivity are very important factors to ensure a uniform cells distribution, tissue ingrowth, delivery of signaling molecules, growth factors, nutrients, oxygen and also for metabolic wastes removal. Nevertheless, too large pores reduce the surface area, which decreases the mechanical properties of the scaffold and limits cellular attachment. Thus a compromise needs to be reached [18, 22],

- be stiff in order to be handled during surgery, but not to much to allow follicle expansion [2, 17, 22].

Several materials have been tested to create such a matrix and studies on transplantation of encapsulated ovarian follicles in different matrices are summarized in Table 1, Appendix A. These materials can be divided into two categories (Fig. 4.2), depending on their origin, namely natural or synthetic polymers. So far, several natural polymers as collagen, plasma clots, alginate, decellularized ovarian ECM (DOM) and fibrin have been used as matrix for the TAO. On the other hand, only one study tested a synthetic polymer, namely, the polyethylene glycol (PEG). All these matrices have a common particularity, which is to be highly water-soluble 3D polymer networks, called hydrogels. These polymers are well suited for this application due to their high water content, which mimics the natural ECM. Besides, their physical (porosity, degradation rate) and mechanical (stiffness, physical strength) properties can be modulated according to the TAO requirements, described in the following section. [1, 3, 22]

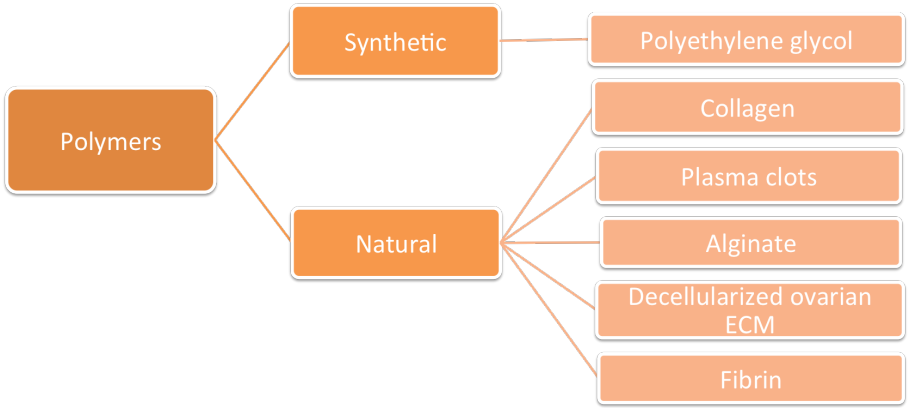

Figure 4.2: Classification of different types of polymer tested to create the TAO's scaffold. Picture adapted from [1].

4.3.1 Natural polymers

The first biomaterials tested for this clinical application were natural polymers. Indeed, they represent well suited materials for the TAO's scaffold for several reasons: (1) their structure is very similar to the ECM of the natural ovary, (2) they are biodegradable and their degradation products are relatively non-toxic, (3) they are often biocompatible due to the presence of biofunctional molecules and therefore, (4) have a better interaction with cells. Nevertheless, compared to synthetic polymers, they have poor mechanical properties and are thus, more difficult to handle. Moreover, their complex structure avoids them to be easily modified and their degradation rate is difficult to control. [1, 3, 22]

Collagen

As previously said, the human ovarian cortex is a collagen-rich tissue, collagen being the main extracellular protein of connective tissues. For this reason, this matrix was a logical option for the artificial ovary. In addition, this protein has widely been used in several biomedical applications due to its advantages, such as low immunogenicity, biocompatibility or ability to be combined with other molecules. [1, 3]

This scaffold has been tested only once to encapsulate murine preantral follicles, which were then cultured in vitro for 7 days and finally, allotransplanted. After 10 days of grafting, large oocytes were obtained and fertilized in vitro, allowing to obtain embryos (see Appendix A, Table 1). Despite these promising results, no other

study with collagen hydrogels was performed for this application. [1]

Plasma clots

Plasma clots are made of autologous plasma from the patient mixed with calcium chloride ($CaCl_2$) in order to create the hydrogel. This matrix has been chosen for the TAO assembly due to its qualities, such as: (1) the absence of immunogenicity considering its autologous origin, (2) its simple clinical procedure and (3) its rich composition in growth factors, which promotes cell adhesion, proliferation and differentiation. [1, 9, 21]

Despite the promising results obtained with plasma clots (see Appendix A, Table 1), this technique has several drawbacks. First, the plasma clots composition is unknown, depending on the patient and on the preparation procedure, which can lead to variable outcomes. Secondly, they are difficult to handle and degrade quickly, which can induce follicle loss. And finally, although growth factors may improve cells survival and development, the additional presence of plasmatic substances may inhibit growth, differentiation and cell function. [1, 9, 21]

Decellularized ovarian extracellular matrix

Recently, decellularized extracellular matrices have attracted much attention in regenerative medecine. Indeed, they have been tested to replace several tissues or even organs like heart, liver, lungs or kidney [1, 21]. The concept of such matrices consists in the decellularization of allogenic or xenogenic homologous tissues or organs, followed by the recellularization of the obtained scaffold with autologous cells [21]. The 3D resultant scaffold is principally made of component molecules of the ECM, preserved in their native architecture. Decellularized tissues can be also used to manufacture hydrogels. Indeed, the resultant matrix has shown some abilities to promote tissue regeneration, maintain the biological activity of remaining ECM proteins and preserve cytokines present in the tissue before decellularization. [1, 21]

As the maintenance of the 3D follicular structure is an essential criterion for the TAO's scaffold, DOM is a very interesting option for the conception of the TAO. Therefore, several studies (see Appendix A, Table 1) have tested bovine or human

DOM hydrogels grafted with mouse follicles. Although these preliminary studies obtained promising results, further researchs need to be undertaken. [1, 21]

Alginate

Alginate is a general term for a polysaccharides family derived from brown algae or bacteria. This block copolymer is made of two repeating monomer units, β-D-mannuronate (M) and α-L-guluronate (G) joined by β(1-4) linkage. These repeating units arrange in blocks either composed of consecutive G, consecutive M, or alterning G and M residues. Alginate can also form stable hydrogels with addition of calcium (Ca^{+2}) or other divalent cations which crosslinked with G-blocks. The physical properties of the resultant hydrogel is thus dependent on M/G ratio, G-block length and other factors. [1, 9, 3, 25]

Alginate has been widely used in biomedical applications due to its attractive characteristics, including, biocompatibility, biodegradability, ease of gelation, non-antigenicity, versatility, ease of cells encapsulation and low toxicity (depending on its purity). [1, 9, 20, 25]

Although alginate has been proved to offer a more natural physical environment to follicles by preserving their 3D structure, this matrix was found to have some limitations, such as low degradation rate, poor cell attachment and lack of neovascularization inside of the matrix when transplanted, due to the slowness of the degradation. Indeed, even though alginate is biodegradable, its degradation rate is difficult to regulate. The second important disadvantage of alginate is its lack of interaction with encapsulated cells. To overcome this limitation, alginate can be combined with ECM components like collagen, fibrin, laminin, or fibronectin, in order to improve follicle growth. [1, 20, 26]

Considering its advantages, alginate hydrogels appeared to be a great candidate as TAO scaffold. Therefore, transplantation of murine preantral follicles (see Appendix A, Table 1) has been performed, but despite these encouraging results, its limitations explicited above have turned research teams toward another option, a fibrin-based matrix.

Fibrin

It is important to highlight that since the scaffold tested in the present study is made of fibrin, its description will be more detailled than other matrices.

Fibrin is a natural polymer made from commercially purified fibrinogen and thrombin. Fibrin hydrogels have been widely used in many biomedical applications as bioadhesive, in surgery, or as scaffold, in tissue engineering, due to their interesting characteristics, such as low immunogenicity, high biocompatibility, ease to be handled, biodegradability and angiogenesis promotion. Besides, their physical properties like porosity, fibers diameter and rigidity can be modulated by fibrinogen and thrombin concentrations and polymerization conditions, which makes this matrix very versatile. [1, 9, 21, 27, 28]

Fibrin results from the interaction of two components, fibrinogen and thrombin. While fibrinogen (F) is a soluble plasma protein whose concentration unit is generally reported in mg/ml, thrombin (T) is an enzyme activated in presence of calcium quantified in U/ml[1]. The fibrinogen molecule is provided with two pairs of three peptide chains (Aα, Bβ and γ) held together by disulfide bonds, and three domains, two D-domains at the extremities and a central domain E composed, among others, of two fibrinopeptide sites A and B (Fig. 4.3). When active, thrombin is added to the fibrinogen solution to cleave the two peptide sites, resulting in the conversion of fibrinogen into unstable fibrin (Fig. 4.3, step A). The fibrin monomers assemble together first longitudinally, by formation of $\alpha - \gamma C$ interactions between domains E (site A) and D, forming two parallel strands, called together, protofibril (Fig. 4.4.(a)). When long enough, the protofibrils assemble together laterally and form bundles of twisted fibers by several weak protein-protein bonds (Fig. 4.4.(b)): (1) interactions $\gamma C - \gamma C$ between D domains, two kind of interactions between domain E (site B) and domain D, namely, (2) $\beta - \beta C$ to reinforce $\alpha - \gamma C$ linkages and (3) $\beta C - \beta C$ to reinforce $\gamma C - \gamma C$ bonds. After lateral aggregation, several branchments are made between the generally three fibrin fibers, creating a 3D network. This network, thanks to factor XIIIa activated first by thrombin and then by

[1]The unit U/ml describes the enzymatic activity of thrombin per volume of solution.

Ca^{+2} ions, is then stabilized by covalent bonds ($\gamma - \gamma$ and $\alpha - \alpha$) both within and between protofibrils, which creates stable fibrin (Fig. 4.3, step B and Fig. 4.4.(b)). This addition of covalent bonds stiffens the network and makes it more resilient to lysis. [9, 29, 30, 31, 32, 33, 34]

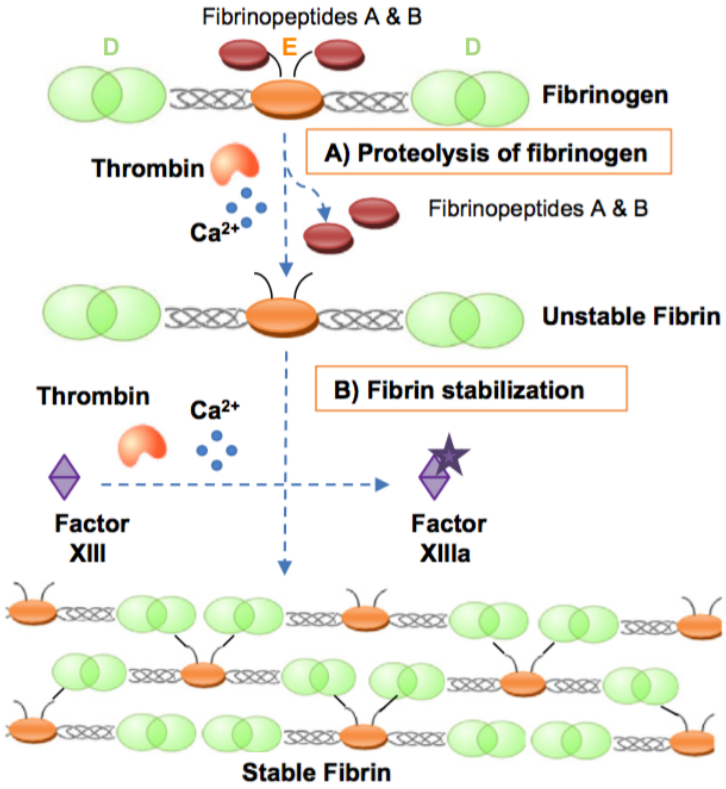

Figure 4.3: Formation process of a fibrin network. (A) Fibrinogen is lysed by thrombin at specific sites named fibrinopeptides A and B. (B) The protofibrils aggregate first longitudinally, then laterally. The obtained fibers crosslink and the resulting network is consolidated by factor XIIIa, activated beforehand by thrombin and calcium ions. [9]

As mentioned, an interesting property of fibrin hydrogels is the modularity of their physical characteristics by varying fibrinogen and thrombin concentrations. Indeed, studies showed that fibrin pore size is inversely correlated with fibrinogen and thrombin concentrations thus, the higher thrombin and fibrinogen concentrations, the smaller the porosity. Regarding the impact of fibrinogen concentration on the porosity, it is suggested that the porosity reduction results from the filling in of porous structures. Indeed, the pores might be closed by fibrin layer formation due

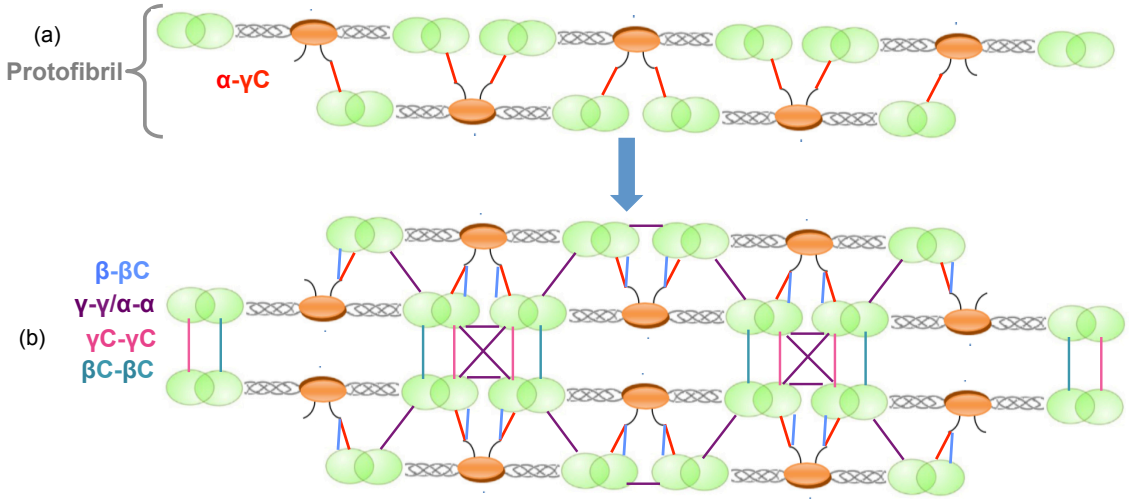

Figure 4.4: Schematic representation of the (a) intra and (b) inter bonds between protofibrils. Picture adapted from [9, 29].

to high fibrinogen concentration. [21, 27, 35, 36]

Besides, thrombin concentration also influences the fiber diameter: low thrombin concentration implies thick fibers while high concentration involves thin fibers. The reason can be easily explained: fiber diameter is controlled by the balance between the rate of lateral aggregation and the rate of fibrinogen cleavage. Thus, at low thrombin concentration, less thrombin is available to cleave fibrinogen molecules, reducing the cleavage rate of fibrinogen, which implies large protofibrils lateral aggregations and thicker fibers. [21, 27, 35, 36]

Finally, branch points density can also vary. The reticulation process is the opposite phenomenon of lateral aggregation. Indeed, during this later one, some protofibrils will diverge in three parts, which produces a branch point. Thus, conditions inhibiting lateral aggregation will favor the crosslinking process. Therefore, thin fibers, induced by high thrombin concentration, are generally associated with short fibers and many branch points. [32, 33]

Considering the numerous promising characteristics of this matrix, several research teams (see Appendix A, Table 1) tested different F/T ratios in order to find the best one for the survival and development of human follicles. The research team at UCL has tested combinations of fibrinogen and thrombin, and their results showed that the best fibrin formulation to encapsulate and graft isolate mouse fol-

licles was 12.5 mg/ml of fibrinogen and 1 U/ml of thrombin [9]. However, when this formulation was tested for human follicles (Amorim C.A., unpublished results), the results were very disappointing. This difference is probably due to the fact that human follicles need a stiffer environment to maintain their 3D structure, which is primordial for their survival and development. Therefore, this group decided to test more rigid matrices, with higher amount of fibrinogen. [2]

Despite these positive results, it is important to bear in mind the disadvantages of fibrin hydrogels as potential scaffold, such as (1) shrinkage of the gel with formation of flat fibrin sheets when using very high fibrinogen concentrations, (2) rapid degradation rate, which avoid proper formation of new tissue and (3) poor mechanical stiffness in the low fibrin concentration clots. Indeed, the major challenge of fibrin scaffold is to find a compromise to answer to the different requirements of the TAO scaffold, for example, being rigid enough to allow its handling during surgery and to maintain the 3D structure of follicles but also not too stiff, because it could negatively affect follicle growth. [21, 35]

4.3.2 Synthetic polymers

Synthetic polymers have been extensively used for bioengineering applications due their biocompatibility and modular properties. Indeed, their mechanical characteristics can be adapted to a specific clinical application. For example, they can be coated with different compounds to promote cells adhesion, proliferation and differentiation and their degradation rate can be controlled. Besides, they can be produced in large quantities and have a long shelf life, which can be useful for artificial systems which must not be degradable. Nevertheless, the disadvantages of these synthetic materials are that: (1) they might degrade into toxic products at high concentrations and (2) residual solvents used for their conception might dispersed in the body, which might both lead to inflammation and compromise the success of the transplant. [1]

For the specific application of the TAO, the only synthetic polymer tested was PEG.

Polyethylene glycol

PEG is a linear polymer used in many biomedical applications due to its versatility. Its structure is represented in Fig. 4.5 and can also be expressed as H-(O-CH_2-CH_2)$_n$-OH. One of its biggest advantages is its ability to be crosslinked with other polymers in order to create complex matrices with specific and controlled properties, such as degradation rate or adhesion capacity. [1, 37]

In the only study with follicles, PEG was modified with vinyl-sulfone groups, and then used to encapsulate murine primordial follicles (see Appendix A, Table 1). After 30 days of transplantation, antral follicles were found, the matrix was invaded by surrounding cells and new vessels and its degradation had begun. Nevertheless, no other transplantation study has been realized using this material. [1]

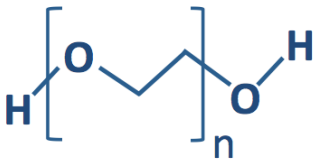

Figure 4.5: Structure of the polyethylene glycol molecule, also expressed as H-(O-CH2-CH2)$_n$-OH. Picture adapted from [37].

4.4 TAO biochemical signaling: bioactive factors

As explained in chapter 2, folliculogenesis is a complex process controlled by many factors, either inhibitory or stimulatory. As this process is still poorly understood, the ability to know which bioactive factors should be added in the TAO remains a big challenge. Although such factors could considerably help follicular survival and ensure correct follicular development, no studies are currently undertaken in order to better understand these mecanisms. [21]

Another problem linked to the addition of bioactive factors is their delivery. Indeed, ideally, they should be encapsulated in order to safeguard their activity and avoid their quick denaturation and degradation. Moreover, different factors should be delivered at different time points, as follicles need specific factors according to their developmental stage. For this, as previously shown in Fig. 4.1, the idea would

be to encapsulate them in degradable micro/nanospheres. In this way, their release could be modulated by the amount of factors charged in the micro/nanospheres, the number of micro/nanospheres placed in the TAO or their composition. [21]

As examples of interesting factors, inhibitory factors such as AMH could be added with the aim of ensuring the recruitment of just a few primordial follicles, preventing therefore the activation of the entire follicular pool at once. Another possibility could be to add growth factors, such as vascular endothelial growth factor, to increase vessel formation, and to improve oxygen, nutrients and wastes transport along with enhancing cells survival and development. Other factors like sex hormones, growth differentiation factor 9 or kit ligand could also be added to control follicle development. [21]

Chapter 5

Understanding the ovarian tissue to develop the artificial ovary matrix

5.1 Strategy

The goal of the TAO is to mimic the human ovarian cortex ECM in order to create an environment that promotes follicles survival and development, moreover it should degrade to be replaced by a new natural ovarian structure. To create such a scaffold, it is therefore necessary to know the physical and morphological properties of the human ovarian cortex. To this end, in the present study, the morphological properties and physical behaviors of the human ovarian cortex were characterized with the aid of a scanning electron microscope (SEM) and a rotational rheometer, respectively. Both experiments took place in the Boltzmann laboratory in Louvain-la-Neuve.

As rheological analyzes had never been done on biological samples in this lab and since human samples are quite small and not easily obtainable, tests on ovarian fragments of other animal species should first be performed to check if the results were consistent with the litterature. For this, bovine ovaries were used as they are very similar to human ones. Indeed, the size is an important factor in rhe-

ology because the rheometer used for the experiments needs samples of minimum 8 mm of diameter, which is nearly impossible to obtain from a young and alive woman. Although, removing such a large piece of ovary would not pose a problem for menopaused patients, performing rheological analyzes using these women would introduce a bias in our study because the rigidity of the ovary increases with the age due to multiple ovulations. It is therefore primordial to analyze young specimens in order to assess the ovary's rigidity during women reproductive life. Moreover, due to the impossibility to perform the rheological analyzes in the same day as the biopsy collection, the human samples should be cryopreserved. Therefore, tests on bovine samples will be carried out to evaluate if there are any difference, either morphological or physical, between fresh and frozen-thawed tissues. Once we certify that our results obtained with bovine ovarian tissue do not differ from the litterature and the findings from fresh and frozen-thawed fragments are similar, we can finally evaluate the human cortical ovarian tissue.

As previously stated, due to machines limitations, we do not know if rheological properties of smaller samples can be assessed. Therefore, a second study should be designed, this time to compare large and small samples in order to define a correction factor. To this end, two fragments of ovarian cortex from menopaused patients should be collected: one that fits the machine requirements (8 mm) and a smaller one that would represent the biopsy size that is usually obtained from young patients. After finding out this correction factor, ovarian cortex samples from our target group should be evaluated by the rheometer and its rigidity and other physical properties, calculated after applying the correction factor.

Finally, several fibrin matrices will be tested with the same procedure used for ovarian tissue to assess which formulation is the most similar to the natural human ovary.

In parallel, samples of bovine and human ovarian cortex and fibrin matrices will be evaluated by SEM in order to compare the morphological properties of the samples.

5.2 Introduction to the techniques used

To assure the understanding of the results in the following chapters, the several instruments and techniques used in this study are explained, namely the SEM, the critical point dryer (CPD), the sputter coater and rheology.

5.2.1 Scanning Electron Microscope

Briefly, the SEM has been invented to surpass the limitations of the optical microscope, principally the resolution, which is limited by the wavelenght of light. Indeed, this electron microscope reveals morphological informations about a sample at the nanometric scale by scanning it under vacuum with a focused beam of high-energy electrons, in place of a light beam as in an optical microscope. [38]

As described on Fig. 5.1, the principle is the following. The sample is mounted on a specimen stub and placed inside the microscope, more precisely in a high-vacuum chamber (*Sample Chamber*, Fig. 5.1). This stage allows the sample to stay stable or to be moved to a desired position. Indeed, the stability of the specimen is important for a better spatial resolution and to avoid the sample to fall in the chamber. [39]

An electron gun (*Electron Gun*, Fig. 5.1) emits a beam of electrons (*Electron Beam*, Fig. 5.1) which is focused by one to three electromagnetic lenses and an objective lens to reach the sample's surface at a specific site (*Condenser Lens, Objective Lens*, Fig. 5.1). In a typical SEM, the electron gun is constituted of a filament cathode, which is heated in order to emit the electron beam, and of an electron-accelerating chamber that accelerates the emitted electrons, in order to increase their energy. [39]

The incoming electrons, namely primary, when reaching the surface of the material, produces, among others, secondary and backscattered electrons and X-rays, which are detected by different specialized detectors (*Secondary Detector, Backscatter Detector, X-ray Detector*, Fig. 5.1). More specifically, the backscatters ones are primary electrons that are reflected by the specimen, whereas secondary particules result from the interaction between primary and atomic electrons. Indeed

the incoming particules give energy to the atomic ones, which is then released as secondary electrons [39]. While secondary electrons are the most important ones for showing morphology, backscattered electrons are responsible for illustrating chemical contrast [40]. In order to obtain an image of the sample, the surface is thus scanned at the same time in two perpendicular directions, and secondary electrons from each point of the surface are collected. [39]

The sample chamber is maintained at high-vacuum on one hand, to promote the beam alignment while avoiding the scattering of primary electrons by air particules and, on the other hand, to avoid, or at least slow, the filament oxidation. [40]

This technique has typically a resolution between $2-3$ nm and 10 nm, depending on the sample's nature, voltage, vacuum, detectors,...

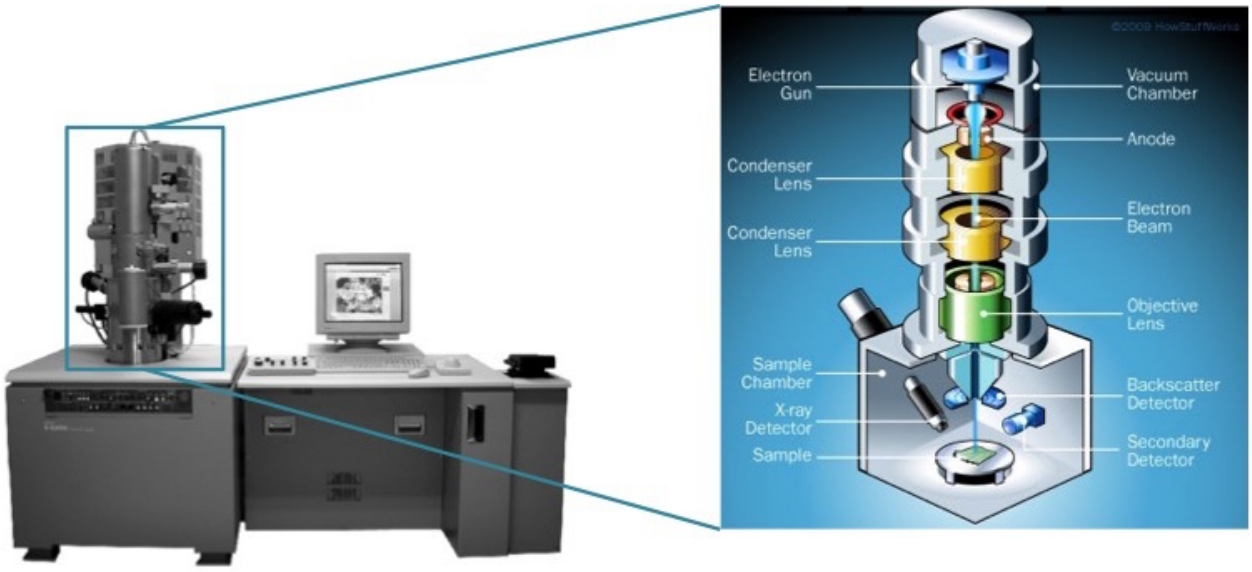

Figure 5.1: Picture and schematic representation of a scanning electron microscope and its components. Picture adapted from [39, 41].

To be analyzed by scanning electron microscopy, specimens must be:

1. Completely dry since the sample chamber is at high vacuum. Thus, for soft biological tissues, supplementary steps are needed in order to preserve and stabilize the structure, namely fixation and dehydration. The first one consists in the incubation of the sample in a solution of a buffered chemical fixative.

In this study, glutaraldehyde has been chosen. This agent is currently used with biological tissues as it fixes proteins, lipids, nucleic acids and sugars, by binding covalently their amino acids functions. Once the sample is fixed, it can be dehydrated. As air-drying would involve major collapsing and shrinkage of the specimen, this drying process is achieved by the replacement of water in the tissue with an organic solvent, such as ethanol or acetone, by critical point drying (see section 5.2.2). [39]

2. Electrically conductive and grounded to avoid accumulation of electrostatic charges at the surface. Thus, many conductive materials do not require a special treatment before being analyzed in the SEM. On the opposite, nonconductive samples tend to charge when reached by the electrons, which implies image artifacts and scanning faults. In order to avoid these problems, nonconductive samples are coated beforehand with a nanometric film of an electrically conducting material. In general, chromium (Cr) or gold (Au) are deposited by sputter coating (see section 5.2.3). Gold is preferred for the coating of biological samples because chromium tends to oxidize in chromium oxide (CrO), which is not conductive. In summary, to be made electrically grounded and conductive, a biological sample, after all the preparation steps, is mounted on a metallic stub using an electrically conductive double-sided adhesive tape and sputter-coated with gold. Moreover, postfixation with osmium is often used for biological tissues to increase the bulk conductivity of the material and to rigidify it. [39]

To be able to read the ouput images, several parameters must be kept in mind.

First, thicker regions will appear darker because they reflect more backscatter electrons. [39]

Moreover, heavy elements will be brighter because they have a higher probability to emit secondary electrons than lightweight elements. [40]

Thirdly, the highness of the samples will also affect the contrast. Indeed, if the sample is irregularly shaped, higher regions will appear darker because they occur to

be closer to the detectors. Therefore, more secondary electrons coming from these regions will be detected. [40]

Finally, if the sample's surface is not flat, the sputter coating will most probably not be uniform. Thus, some badly coated regions, being therefore less conductive, will accumulate primary electrons and, accordingly, appear darker than well coated areas because no secondary electrons will be emitted. [40]

5.2.2 Critical Point Dryer

As said in section 5.2.1, samples need to be dry before their introduction in the microscope. Nevertheless, air-drying can't be used due to the high water content of our samples, namely biological tissues and fibrin hydrogels which have both a fibrillar structures. Indeed, as represented on Fig. 5.2, as the water would evaporate, the fibrillar network of the samples would collapse and the natural structure would be lost. [38]

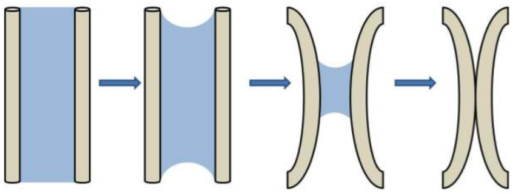

Figure 5.2: Schematic representation of the collapsing of the structure of two fibers with water evaporation [38].

To avoid this phenomenon, a specific instrument is commonly used, namely CPD. Its working principle is based on the use of supercritical fluids. More precisely, a supercritical fluid corresponds to a phase over specific temperature and pressure, called critical temperature (T_c, Fig. 5.3) and critical pressure (p_c, Fig. 5.3), respectively. While the first one is the temperature at which a gas can't liquefy, the second one is the minimal pressure needed to liquefy a gas at its critical temperature. Such a fluid shows both gas and liquid characteristics. Above this critical point ($T_c; p_c$), no matter the increase of temperature or pressure, the material will stay in its supercritical phase (*Supercritical Fluid Region*, Fig. 5.3). In this state, the interfacial

strength between liquid and gaseous phases disappears and those two phases are no longer distinguishable. [38, 42].

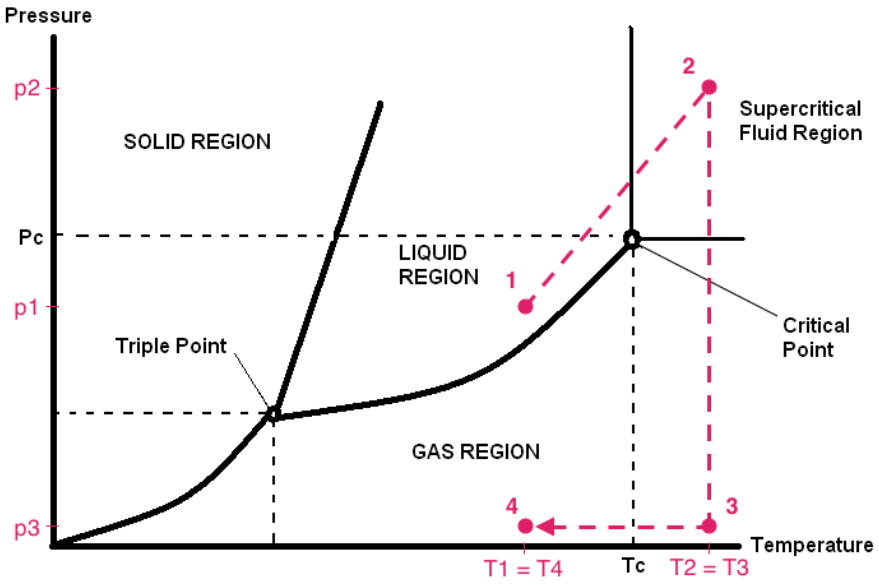

Figure 5.3: Phase diagram of CO_2. From 1 to 2: Increase of both temperature and pression, in order to exceed the critical point $(T_c; p_c)$. From 2 to 3: Opening of the chamber, to let the CO_2 escaped, and decrease of the pressure at constant temperature. From 4 to 3: Decrease of the temperature at constant pressure, to remove the dehydrated samples from the machine. Picture adapted from [38, 42].

The critical point is specific to each material, but appears to be very high for water (374°C; 220.6 bar), avoiding the use of this liquid in the CPD. Indeed, biological samples would be completely destroyed due to high temperature and pressure values. To overcome this problem, water is commonly replaced by liquid carbon dioxide (CO_2), whose critical point is more appropriate: (31.10°C;73.7 bar). Even-though CO_2 is a good alternative to water, one of its disadvantage is its immiscibility with water, which is present in the samples. Therefore, water has to be exchange with an organic solvent, such as ethanol or acetone, which are miscible with both water and liquid CO_2. To this end, before to be charged in the CPD, the samples are plunged in consecutive baths of growing concentrations of the selected organic solvent. Once done, the samples can be charged in the machine, where the solvent is substituted by liquid CO_2. As a result, the samples are dried, without damaging their structure. [42]

Technically speaking, the CPD is provided with a temperature chamber where the samples, beforehand placed in sample holders to distinct them easily, are introduced (Fig. 5.4). This chamber is linked to two valves: one inlet valve connected to a CO_2 tank (*Inlet Chamber*, Fig. 5.4), in order to let the gaseous CO_2 come in, and an output valve leading to the outside, which allows the evacuation of liquid ethanol and water (*Exhaust valve*, Fig. 5.4). This device is also provided with gauges to control the temperature and the pressure inside the chamber (*Chamber temperature gauge, Chamber pressure gauge*, Fig. 5.4). [38]

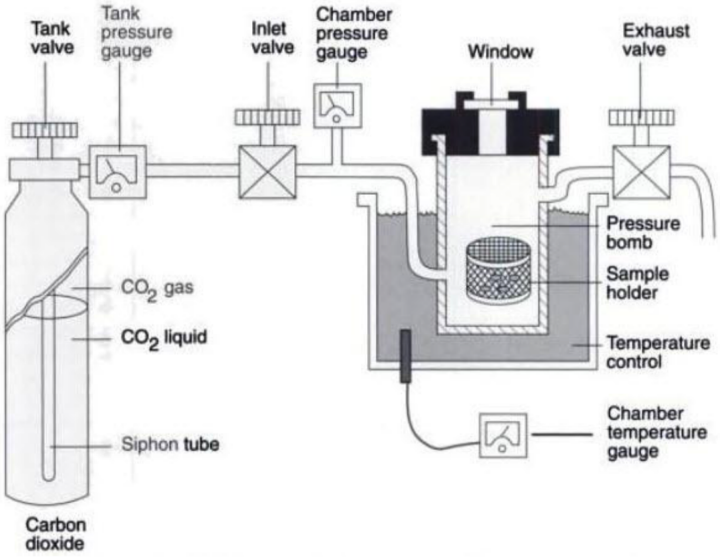

Figure 5.4: Simplified representation of a critical point dryer. [38]

Once all the ethanol has been replaced by liquid CO_2, the dehydration process can begin. First, the temperature is increased from 5°C up to 45°C. Simultaneoulsy, the pressure increases until maximum 98 atm (*Point 1* $\rightarrow$ *Point 2*, Fig. 5.3). While the increment of temperature tends to induce the evaporation of the CO_2, the rise in pression tends to do the opposite, namely, condense it. When the critical point has been surpassed, only one phase remains, i.e. the supercritical fluid. The exhaust valve is then gradually opened in order to allow the slow escape of CO_2, resulting in a decrease in pressure (*Point 2* $\rightarrow$ *Point 3*, Fig. 5.3). When the pressure reached the value of the atmospheric pressure ($\sim$1 bar), the chamber can be opened and the

samples, removed. At the end of the process, the chamber temperature is brought back at room temperature (RT) (*Point 3* $\rightarrow$ *Point 4*, Fig. 5.3). [38]

Eventhough this technique is better than air-drying, it's not perfect because a small shrinkage of the samples is still generally observed ($\sim$ 10-20%). [38]

5.2.3 Sputter coater

As explained in section 5.2.1, before their introduction into the SEM, samples need to be coated with a conductive material to reduce charging effects, to increase thermal conduction and also, to improve the secondary electrons signal. Several coating techniques are available on the market but in this study, sputter coating has been chosen. [38, 43]

This technology implies the deposition of a nanometric coating (ranging from 2 to 20 nm) of an electrically-conducting metal such as gold, gold/palladium, chromium, platinum, silver or iridium on a non- or poorly-conductive material. In this study, gold has been chosen to better preserve the morphology of the biological specimens. [43]

Eventhough several designs are available, the working principle stays more or less the same. As represented on Fig. 5.5, the sample is put in the upper chamber. But beforehand, the specimen is mounted on a specimen stub and attached on it through double-sided adhesive tape. Then, the chamber is closed and placed under low-vacuum by a rotary vacuum pump until reaching a pressure of 0.1 Pa, in order to avoid the damaging of the sample's surface. After that, the chamber is filled with an inert gas such as argon (Ar) by an argon carboy linked to the chamber. The idea is to replace to air-atmosphere by an argon-one, while keeping a low-vaccum value of 6-7 Pa.

A high potential difference is then applied in order to create argon cations (Ar^+) and electrons ($e-$) by ionization of Ar atoms. As a consequence, these charged particules are attracted to opposite electrodes, as shown on Fig. 5.5, producing a small current and a self sustaining glow discharge. While the cathode is played by the Au plate on the top of the chamber, the anode one is played by the sample,

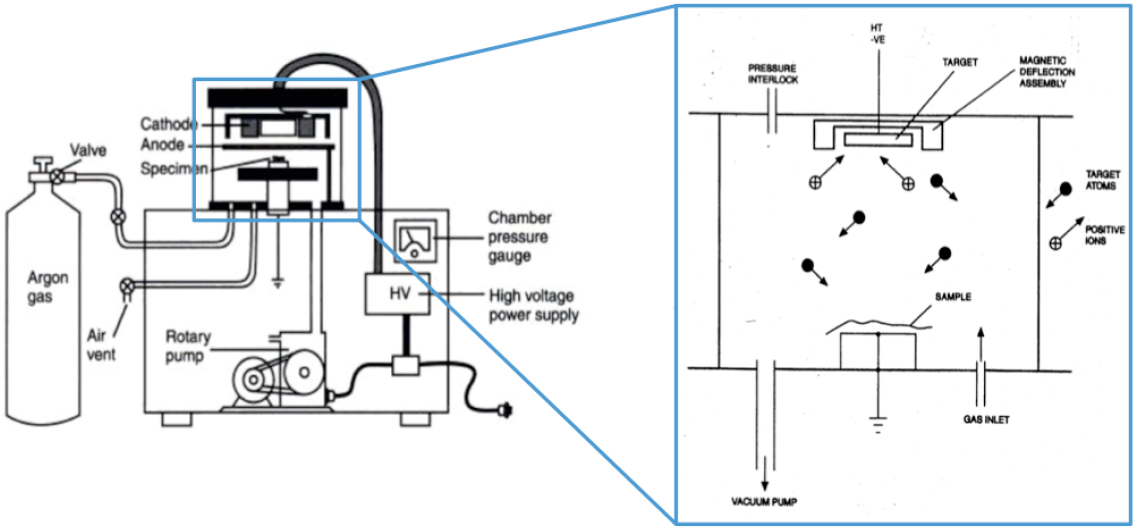

Figure 5.5: Simplified representation of a sputter coater. Picture adapted from [38, 43].

which is grounded to make sure it's at ground potential (0 V). [43]

Finally, this ion bombardment of the cathode induces its erosion and sputtered Au atoms from its surface are deposited on the sample. Due to multiple collisions between charged particules, Au are sent in all directions, which allows them to reach the sample from many different angles, and to coat it approximately with a uniform metallic layer. [38, 43]

The glow discharge depends on several parameters, such as the chamber pressure or the cathode material. For example, Au deposition is quicker than Cr because of its more effective electrical conduction characteristics. Besides, the deposition rate is current dependent while the thickness of the film depends both on the exposition time and induced current. [43]

5.2.4 Rheology

What is rheology? Rheology is a science that studies deformation and flow of materials on which stresses are applied [44]. All kind of materials can be analyzed by rheology. Nevertheless in practice, rheology is used to characterize materials having a behaviour between two theorical models, i.e the Newtonian fluid and the elastic solid. Such materials are called viscoelastic and behave thus both as a fluid and as a solid. These three classes of materials are described in the following paragraphs.

[45, 46]

Newtonian fluids Newtonian fluids are materials that stay deformed when a shear stress (τ in [Pa]) is applied and then removed. Thus, these liquids don't keep in memory their initial shape. A dashpot is generally used to represent the answers of those materials (Fig. 5.6) because, when a constant stress τ_0 is applied for a certain period of time (from $t = 0$ to t_0), the dashpot is deformed but does not come back to its initial position when the stress is released after $t = t_0$ (Fig. 5.6). In other words, the energy injected by the shear deformation (γ), also called shear strain, is almost immediately dissipated by the Newtonian fluid [45].

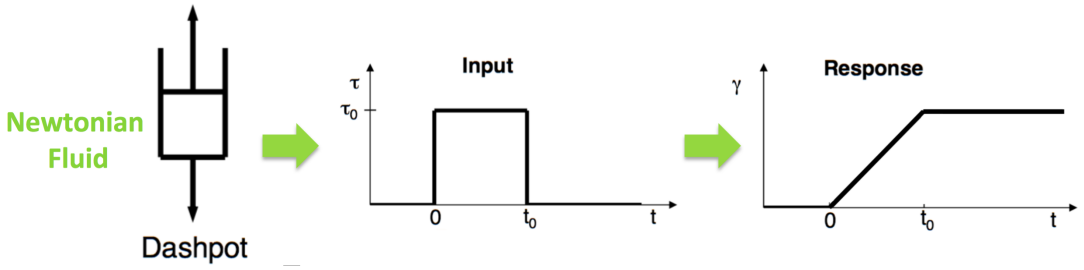

Figure 5.6: Description of the Newtonian fluid model. A dashpot is used to represent this model. If an input shear stress of amplitude τ_0 is applied on such a material from $t = 0$ to t_0, it will deform gradually from $t = 0$ to t_0 and stay deformed, after releasing the stress, by dissipation of the deformation's energy. Picture adapted from [47].

Besides, their behaviour can be modelized by the following equation 5.1 with $\dot{\gamma}$ being the shear rate (in $[s^{-1}]$ and reflecting the speed at which the material is deformed) and η, the constant viscosity of the fluid (in [Pa.s] and represents the fluid's resistance to flow). Thus, according to this equation, if a material has a high viscosity, a higher shear stress must be applied to obtain the same shear rate. This model is well suited for water or air but not for more complex fluids. Indeed, for Newtonian fluids, the hypothesis of a viscosity independent on time and shear rate is made, which does not allow to describe the behaviour of complex fluids. [45, 46]

$$\tau = \eta.\dot{\gamma} \tag{5.1}$$

Elastic solids The other boundary case is the elastic solid model. Unlike Newtonian fluids, when submitted to a shear stress, they recover their initial shape, once this stress released. The deformation is defined as completely reversible. Indeed, these materials can store the deformation's energy without dissipating it, which is the opposite behavior compared to the other boundary case[45]. A good way to modelize those materials is through a spring (Fig. 5.7). Indeed, when a shear stress τ_0 is applied during a time interval $[0; t_0]$, the spring deforms and then comes back to its initial position, when the stress is released (Fig. 5.7).

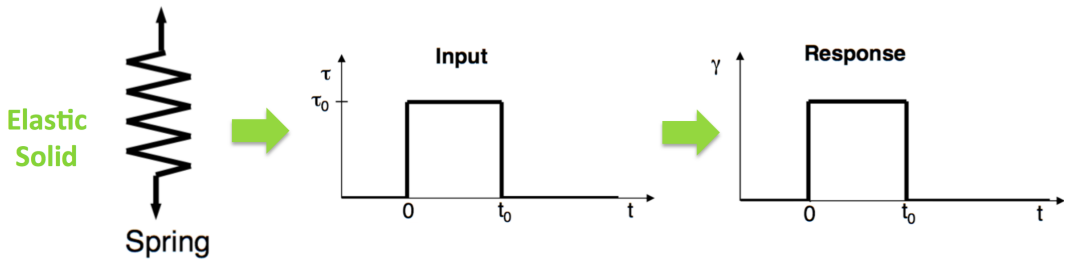

Figure 5.7: Description of the elastic solid model. A spring is used to represent this model. If an input shear stress of amplitude τ_0 is applied on such a material from $t = 0$ to t_0, it will deform directly from $t = 0$ to t_0, but then return at its initial position after the releasing of the stress, by restauring all the deformation's energy. Picture adapted from [47].

Elastic solids are represented by the following equation (Eq. 5.2) with τ, the shear stress (in [Pa]), γ, the shear strain (in [%]) and G, the storage (or elastic) modulus (in [Pa]), which represents the resistance of the solid to the deformation, namely, its rigidity. While Newtonian fluids have a constant viscosity, elastic solids, on the other hand, have a constant storage modulus. This way, according to equation 5.2, if a solid has a high storage modulus, a higher shear stress must be applied to obtain the same shear strain. This model is valid for most solids, like rubbers or metals, but only in specific conditions, such as small deformations, certain temperature or, for solids with a constant storage modulus. [45]

$$\tau = G.\gamma \tag{5.2}$$

Viscoelastic materials For materials which do not fit in one of these two categories, an intermediate one is more suitable, namely the viscoelastic model. Those

materials have variable behaviors according to time. Indeed, just after the application of a shear stress, they will react like solids then, they become more and more viscous with time and finally, after very long times, they behave like Newtonian fluids (Fig. 5.8). Therefore, a combination of a dashpot and a spring is used to describe such materials. The equations characterizing their behaviors are the following (Eq. 5.3), in which the viscosity and the storage modulus are functions of time. [46]

$$\begin{cases} \tau &= \eta(t).\dot{\gamma} \\ \tau &= G(t).\gamma \end{cases} \tag{5.3}$$

Time dependence As explained, the time notion is very important in rheology. Indeed, the behavior of a material will differ according to its relaxation time and the observation time of the experiment (Fig. 5.8). The relaxation time is an intrinsic property of the material and represents the time the material needs to flow, relax and to become more like a liquid. The observation time refers to the experiment time, namely, the time at which the material is observed. [45]

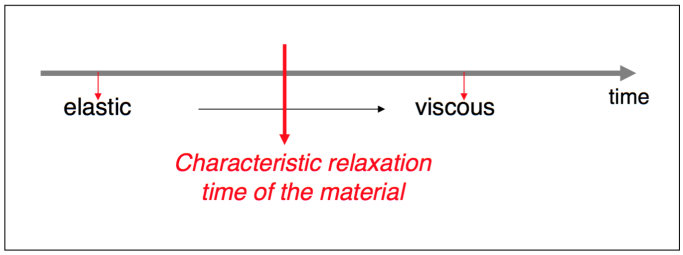

Figure 5.8: Time dependence of the viscoelastic's behavior. If the relaxation time is way bigger than the observation one, soon after the stress application, the material will behave more like an elastic solid. On the opposite, if the relaxation time is way smaller than the observation one, a long time after the stress application, it will have a more viscous behavior. Between those two boundary cases, if the relaxation and the observation times are more or less equal, the material will behave both as a liquid and as a solid, thus as a viscoelastic material. [47]

The Deborah number (De) can be used to compare those two times and thus, to classify the material's behavior. This number is the ratio between the relaxation

time (τ_{rel} in [s]) and the observation one (τ_{obs} in [s]) (Eq. 5.4). [45]

$$De = \frac{\tau_{rel}}{\tau_{obs}} \tag{5.4}$$

According to the De value of a material, it's possible to determine its nature [45]:

- $De \gg 1 \rightarrow$ Elastic behavior,
- $De \ll 1 \rightarrow$ Viscous behavior,
- $De \sim 1 \rightarrow$ Viscoelastic behavior.

Rheometer In this study, all rheological measurements are performed using a rotational rheometer. There are three kinds of rotational rheometer depending on the geometry: either with concentric cylinders (Fig. 5.9(a)), with a cone and a plate (Fig. 5.9(b)) or, with two parallel plates (Fig. 5.9(c)) [46]. In this study, the third configuration has been chosen.

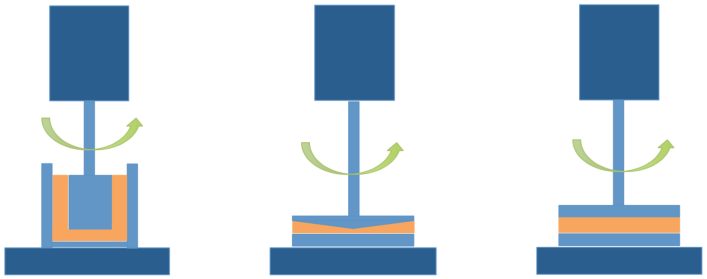

(a) Concentric cylinders. (b) Cone and plate. (c) Parallel plates.

Figure 5.9: Different geometries of rotational rheometer. Picture adapted from [45].

The working principle is the following. The bottom plate is fixed while the upper one is movable. The sample (Fig. 5.9(c) in orange) is loaded on the bottom plate (Fig. 5.9(c) in light blue) and the upper one is moved down in order to trap the specimen between them. The sample is sollicitated, its response is recorded by sensors and finally, the resulting signal is treated to give the experimental data. [45]

In this study, a strain-controlled rheometer is used which means that the sollicatations are essentially shear strains. Indeed, the bottom plate is fixed and the upper one oscillates at controlled amplitude and frequency. [45]

Dynamic moduli G' and G" and phase angle To describe the viscoelastic behaviors of a material, two parameters are generally measured, namely, the dynamic moduli G' and G". To explain those notions, the application of a sinusoidal shear strain γ_{xy} (Eq. 5.5), on the charged sample, is considered.

$$\gamma_{xy}(t) = \gamma_0.sin(\omega t), \tag{5.5}$$

with ω, the frequency at which the sample is deformed and γ_0, the amplitude of the deformation. [45, 46]

Two hypotheses have to be made about this applied strain: first, its amplitude γ_0 needs to be small and second, γ_0 has to be part of the linear regime. Those notions will be explained later. The stress needed to obtain this deformation can be expressed as:

$$\tau_{xy}(t) = \tau_0.sin(\omega t + \delta) \tag{5.6}$$

with δ, the phase angle (the phase between the strain and the stress) and τ_0, the amplitude of the stress. [45, 46]

Indeed, while the stress applied on an elastic solid is in phase with the corresponding deformation (Fig. 5.10.A, $\delta = 0$), in the case of a Newtonian fluid, a phase angle of 90° appears (Fig. 5.10.B, $\delta = 90°$). As a viscoelastic material behaves both like a solid and like a liquid, its phase angle lies between 0 and 90° (Fig. 5.10.C, $0 < \delta < 90°$). Besides, the phase angle of viscoelastic materials is not a constant and varies with the frequency: $\delta(\omega)$. [46]

The equation 5.6 can be easily divided in two parts, one being the elastic part and the other the viscous one. Indeed, by using the trigonometric formula: $\sin(a+b) = \sin(a).\cos(b)+\sin(b).\cos(b)$, by separating viscous and elastic behaviors and knowing that $sin(0°) = cos(90°) = 0$ and $sin(90°) = cos(0°) = 1$, the equation 5.6 becomes:

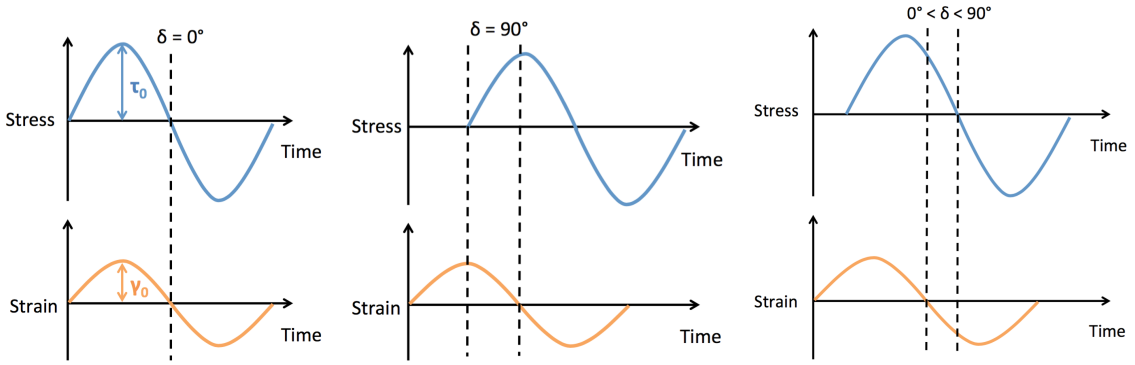

(a) Elastic solid. (b) Newtonian fluid. (c) Viscoelastic material.

Figure 5.10: Comparison between the phase angles, δ, of the different classes of material. Pictures adapted from [46].

$$
\begin{aligned}
\tau_{xy}(t) &= \tau_0 \sin(\omega t + \delta) = \tau_0.[\sin(\omega t).cos(\delta) + \sin(\delta).\cos(\omega t)] \\
\tau_{xy}(t) &= \gamma_0.G'(\omega)[\sin(\omega t).cos(\delta) + \sin(\delta).\cos(\omega t)] \\
&\quad +\gamma_0.G''(\omega)[\sin(\omega t).cos(\delta) + \sin(\delta).\cos(\omega t)] \\
\tau_{xy}(t) &= \gamma_0.G'(\omega)[\sin(\omega t).cos(0°) + \sin(0°).\cos(\omega t)] \\
&\quad +\gamma_0.G''(\omega)[\sin(\omega t).cos(90°) + \sin(90°).\cos(\omega t)] \\
\tau_{xy}(t) &= \underbrace{\gamma_0.G'(\omega).\sin(\omega t)}_{\textbf{Elastic}} + \underbrace{\gamma_0.G''(\omega)\cos(\omega t)}_{\textbf{Viscous}},
\end{aligned}
\tag{5.7}
$$

with G' and G'', respectively the storage (or elastic) and loss (or viscous) moduli. [45]

In other words, G' represents the energy stored by the material during its sollicitation and describes the elastic response, while G'' represents the energy dissipated by the material during the sollicitation and describes the viscous answer. They both depend on the frequency. The phase angle can be linked to those dynamic moduli through the following equation: [45]

$$
\frac{G''(\omega)}{G'(\omega)} = \tan(\delta(\omega)) \tag{5.8}
$$

Rheological tests In this study, different rheological tests are performed to characterize the physical behaviors of the samples. The most used one are the amplitude (or strain) sweep (AS) and the frequency sweep (FS). One other test was also carried

out but to a lesser extend, namely, the temperature sweep (TS).

The amplitude sweep is a dynamic measurement which involves the application of a deformation, which varies from low to high values, at fixed frequency and temperature. This test gives a graph of G' and G'' versus γ. Rheology being mostly used to analyze polymers, Fig. 5.11(a) shows typical G' and G'' curves obtained by applying an AS on a typical viscoelastic polymer. This type of measurement is first used to determine the linear regime. Indeed, as represented on Fig. 5.11(a), at small deformations the moduli are constant. This deformation interval is called the linear regime. Beyond this region, the values of the moduli are functions of the deformation. For this reason, a first AS is generally performed in order to define this region. In other tests such as FS or TS, the strain is fixed at a value included in this interval. But to avoid the damaging of the sample, the AS performed to define the linear regime is generally done at small deformations.

AS are also used to look at the reversibility of the sample's structure. Thus, double amplitude sweeps (AS[x2]) are performed by applying a normal AS from low to high deformations (Fig. 5.11(b), full line), called in this study first round (FR), and directly followed by another AS, from high to low deformations (Fig. 5.11(b), dotted line), defined as second round (SR). If the structure is not entirely reversible, a hysteresis is created between the first and the second round as schematized on Fig. 5.11(b).

The frequency sweep is also a dynamic measurement and consists in sollicitating the sample under fixed strain and temperature and with a frequency varying from high to low values. This test gives a graph of G' and G'' versus ω. As for the AS, a schematic graph of a FS performed on a viscoelastic polymer is shown on Fig. 5.12. FS are interesting tests in order to study the recovery of the material. Indeed, when an AS until high deformations is performed, a FS is generally set after in order to let time to the material to recover its structure. Nevertheless, the disadvantage of this test is its duration. Indeed, it is necessary to wait a least one period of oscillation to get the point corresponding to this frequency [45]. Thus,

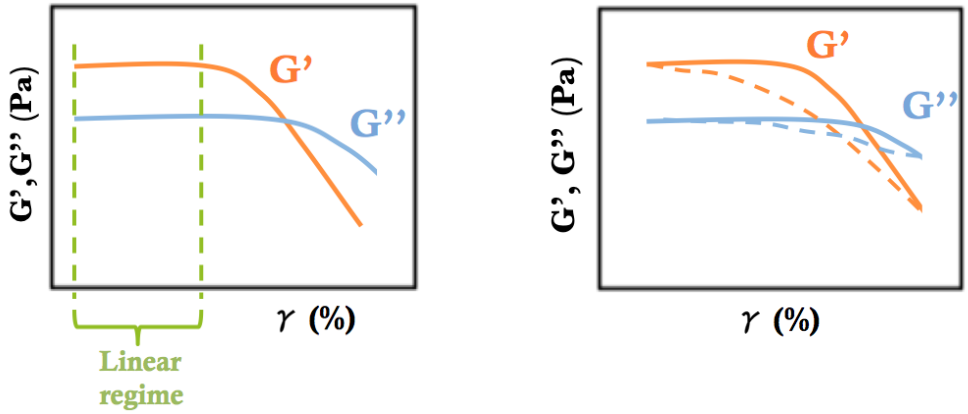

(a) (b)

Figure 5.11: Theoretical graph of amplitude sweeps applied on a viscoelastic polymer with a non fully reversible structure. G' (*Orange*) and G'' (*Light Blue*) in [Pa] versus the strain, γ in [%]. (a) AS in order to define the linear regime. (b) Double AS: first round of G' (G'') low to high deformations in full line and second round of G' (G'') from high to low deformations in dotted line. Pictures adapted from [47].

the smaller the frequency, the higher the precision but the longer the waiting time [45]. Speaking of points, maybe a small explanation is needed. While setting the parameters of the experiment like the frequency, the amplitude or the temperature, the number of points per decade (#Pt./dec) can also be chosen. The more points per decade, the more precise the data but the more longer the experiment time.

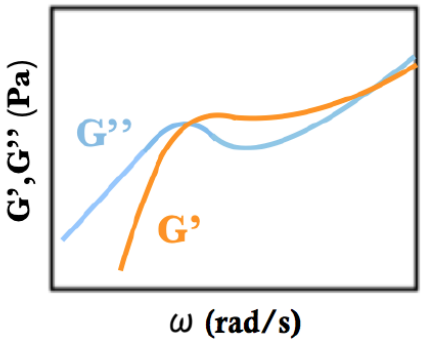

Figure 5.12: Theoretical FS graph of G' (*Orange*) and G'' (*Light blue*) in Pa versus the frequency, ω in rad/s, in order to let time to the material to relax. Picture adapted from [47].

Finally, a temperature sweep can be realized to assess if the temperature has an impact on the sample's behavior. In this case, the strain is set in the linear regime,

the frequency is fixed and the temperature varies. In this study, as bovine and human samples in normal conditions are located in the body, all the experiments were performed at 37°C. For fibrin hydrogels, a TS has been realized to check if major changes occured when the temperature was below 37°C.

Part II

Experimentation

Chapter 6

Characterization of bovine ovarian tissue

6.1 Morphological properties: Scanning electron microscopy

6.1.1 Materials and Methods

Samples Two fresh (Fresh B1 and Fresh B2) and two frozen-thawed (Frozen B3 and Frozen B4) bovine ovarian fragments were analyzed by SEM. All the samples came from four different young cows, all aged between 5 and 8.

Collection Complete ovaries were collected directly at the slaughterhouse, washed in a solution of phosphate-buffered saline (PBS), put in a solution composed of minimum essential medium (MEM) + glutamine[1] and kept at 4°C until reaching the laboratory. Once there, the medulla part of the ovaries was removed with surgical scissors and the cortex was cut into strips. The frozen fragments (Frozen B3 and B4) were cryopreserved while the two other (Fresh B1 and B2) were kept fresh and analyzed the same day. [2]

The freezing procedure was performed according to the protocol established by Amorim et al. [48] using a cryoprotective solution of 10% dimethyl sulfoxide

[1]For more informations, see https://www.thermofisher.com/order/catalog/product/41090028.

(DMSO) and 2% human serum albumine in MEM, in order to avoid the destruction of the tissue due to water crystallization. The samples were then stored at $-80°C$. [2]

Washing For frozen tissues, a preliminary step is achieved in order to defreeze them and to wash away the cryoprotectant solution. In this way, the samples stay 2 minutes at RT, 2 minutes at 37°C in a water bath and are finally washed three times 5 minutes in a fresh solution of MEM.

Fixation The samples are first immersed is a fixative solution, called Karnovsky, composed of glutaraldehyde 2.5%, paraformaldehyde 4% in 0.1M PBS overnight in the fridge (at $\sim 4°C$).

Washing The day after, to remove the Karnovsky's fixative, the samples are washed in 0.1M PBS three times 5 minutes. Each time, fresh PBS is put in new petri dishes.

Post-fixation Then, as explained in section 5.2.1, a post-fixation of the samples in a solution of 2% osmium tetroxide (OsO_4) in 0.1M PBS is carried out 1h in the dark. This step has many goals, such as:

- sprinkling the sample with metallic atoms, making it more conductive,
- rigidifying the specimen,
- staining lipids,
- stabilizing many proteins without destroying structural features and avoiding them to coagulate during the dehydratation step.

OsO_4 being very toxic and volatile, this step needs to be realized under a hod and with gloves.

Washing Once the post-fixation finished, in order to remove the excess in OsO_4, the samples are washed again in 0.1M PBS three times for 5 minutes. As for the previous step, this manipulation needs to be made under a hod and with gloves, as some OsO_4 might remain.

Dehydration After that, a dehydration process occurs to replace the water content by ethanol to be allowed to put the specimens in the CPD. Thus, the replacement is done by successive baths of growing concentrations of ethanol diluted in demineralized water, namely:

1. 15 minutes in ethanol 30%,
2. 15 minutes in ethanol 50%,
3. 15 minutes in ethanol 70%,
4. 15 minutes in ethanol 90%,
5. 10 minutes in ethanol 100%,
6. 10 minutes in ethanol 100%,
7. 10 minutes in ethanol 100%.

At the end, the samples must stay in pure ethanol.

Critical point drying First, the samples are put in small numbered baskets while still lying in the pure ethanol solution to keep them wet. The two outlet valves and the inlet valves are closed. Then the sample chamber is cleaned with a cloth soaked in isopropanol and filled with pure ethanol. The gas cylinder can be opened and the chamber closed.

The CPD is switched on (*Main* button), as well as the thermostat (*Temp* button) in order to decrease the chamber temperature from RT to 5°C. Once the temperature is stabilized at 5°C, the CPD baskets can be introduced in the chamber.

The ethanol is then replaced gradually by liquid CO_2. To do so, the inlet valve is fully opened which implies the increase of the solution's level in the chamber due to the input of CO_2. Once the level reached the top of the chamber, the inlet valve in closed and the outlet ones are opened slowly, to empty the cavity until reaching

the top of the baskets. This emptying takes more or less 10 minutes after what the outlet valves are closed and the inlet one fully opened and those manipulations are repeated. During these cycles, the level must never fall under the baskets to make sure the samples stay wet and intact. Five cycles have been made for fresh and frozen bovine samples.

After the last cycle, when all the ethanol has been removed, the chamber is filled once more and all the valves closed. Then, the temperature is increased degree by degree until reaching 45°C. As explained in section 5.2.2, the purpose of this step is to surpass the critical point of CO_2. While rising the temperature, the pressure simultaneously increases but must stay under 100 bar. Thus, if the pressure becomes to high, the outlet valves can be opened to decrease it. At the end of this step, the (T,p) couple must be around (45°C, 80 bar) then outlet valves are opened to make the pressure fall down at atmospheric pressure ($\sim$1 bar). This step has to be slow and take at least 20 minutes. During this manipulation, as the supercritical point has been surpassed, no gas-liquid interface is visible but the chamber gradually empties.

When the pressure reached 1 bar, the temperature is set at 20°C and once RT has been reached, the chamber can be opened and the baskets removed. Inside the baskets lie the dehydrated samples.

Finally, the outlet valves are fully opened, the gas cylinder closed, the inlet valve fully opened and the device can be switched off (*Temp* and *Main* buttons).

Sputter gold coating To cover the samples with a ultra-thin film of gold, these are first mounted on numbered SEM stubs and fixed on them with double-sided adhevise tape. These assemblies sample/support are then positioned in the machine.

As most of the coating are made with chromium, the cathode needs to be exchange with the gold one. Once done, the machine is closed and the Ar gas is opened with its pressure set around 0.6 bar.

The sputter coater used in this study is a Cressington 208HR (Fig. 6.1). Once the device has been switched on, the following parameters are set: *Tooling* = 1, *Set Point* = 50, *Statut* = 1, *Mode* = MTM + Manual, *current* = 60 mA, *Density* =

19.3 (for gold).

Figure 6.1: Picture of the sputter coater used, namely, a Cressington 208HR. [49]

The chamber is then purged three times with Ar (*Flush* button). The *Leak* button is pressed to stabilize the chamber's pressure between 0.1 and 0.01 mbar.

When all the settings done, the coating process can be activated and the potential difference, applied (*Start/Stop* button). A cache is placed in front of the cathode and removed when the coating rate is sufficient, allowing the coating of the samples to begin. When the film thickness reaches 10 nm, the device is switched off (*Start/Stop* button) and the Ar gas, closed. The machine can thus be opened and the samples, removed. Frozen and fresh bovine samples have been coated respectively with 8 and 10 nm Au films.

Scanning Electron Microscopy Once coated, the samples are analyzed by SEM JSM-7600F (JEOL) (Fig. 6.2) with a potential difference of 15 kV, a working distance of $\sim$ 8 mm and in SEM mode.

6.1.2 Results and discussion

Considering the number of samples studied in this work, Table 2 (Appendix A) provides a summary of all the samples analyzed by SEM.

The SEM pictures obtained after the analyzes of the four samples are compared in Fig. 6.4. They allow to see clearly the fibrous and dense nature of the bovine ovarian cortex and also, the inhomogeneity of its composition.

Figure 6.2: Picture of the scanning electron microscope used, namely, a JEOL 7600F. [50]

The aim of those experiments was to assess if there are any major morphological differences first, between two fresh or two frozen-thawed samples and second, between fresh and frozen-thawed samples. To improve the comparison, four magnifications have been selected. The last one (90 000×) allows to measure approximately the fibers diameter synthetized in the table above (Table 6.1). Different diameters are visible in the same sample principally due to the distance of the fibers from the SEM camera and also, due to sample inhomogeneity.

	Fresh B1	**Fresh B2**	**Frozen B3**	**Frozen B4**
Fiber diameter (nm)	62.6/66.8	64.9/66.6	56.4/62.5	52.9/64.1/64.9

Table 6.1: Fibers diameter (in nm) of four bovine ovarian samples measured by SEM, two fresh (Fresh B1 ad B2) and two frozen-thawed (Frozen B3 and B4) coming from four different cows.

The fibrillar nature of the bovine cortex is mostly due its high content of collagen fibers [7]. Besides, on all SEM pictures, the porosity of the bovine ovarian matrix seems very low due to its dense nature.

While comparing Fresh B1 and Fresh B2 samples, no major difference seems to appear either regarding the fibrillar structure or the fibers diameter, ranging around 65 nm.

On the contrary, Frozen B3 appears more compact and less fibrous than Frozen

B4 and composed of single ($\sim$ 59 nm) and aggregated fibers compared with Frozen B4 which is essentially made of single fibers ranging around 61 nm. Figure 6.3 shows the aggregation of the collagen fibers, whose diameter lies between $\sim$ 0.28 and 0.55 μm, according to the number of aggregated fibers.

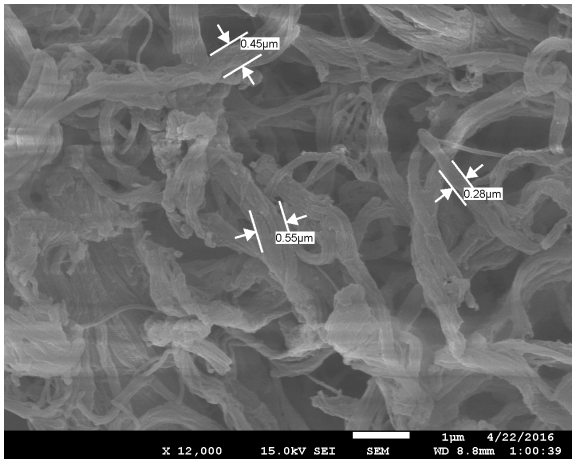

Figure 6.3: SEM picture of frozen-thawed ovarian cortex (Frozen B3) at a magnification of 12 000×.

Regarding those two comparisons, concluding if there is any significant differences between fresh and frozen-thawed bovine ovarian cortex is not possible. Indeed, if comparing samples B1, B2 and B4, no major morphological difference emerges but sample B3 being quite different from B4, there is no way to find out if this difference is due to the freezing-thawing process, or to variability from one cow to another.

Therefore, more samples of fresh and frozen bovine ovarian cortex should be tested. Besides, a more proper way to realize the analyzes would be to cut a cow ovary in two parts in order to keep one half fresh and to freeze the other. This way allows to avoid the problems of variability from one animal to another. Eventhough, it is important to bear in mind the high degree of heterogeneity inside of a single ovary due to pieces of corpus luteum, cells composition, bloods vessels and also due to the risk of some remnants of the medulla during the separation procedure.

Initially, this was the procedure planned for this study but, due to some problems with the SEM analyzes of the first fresh samples and to the lack of time, fresh and frozen ovarian parts do not come from the same ovary.

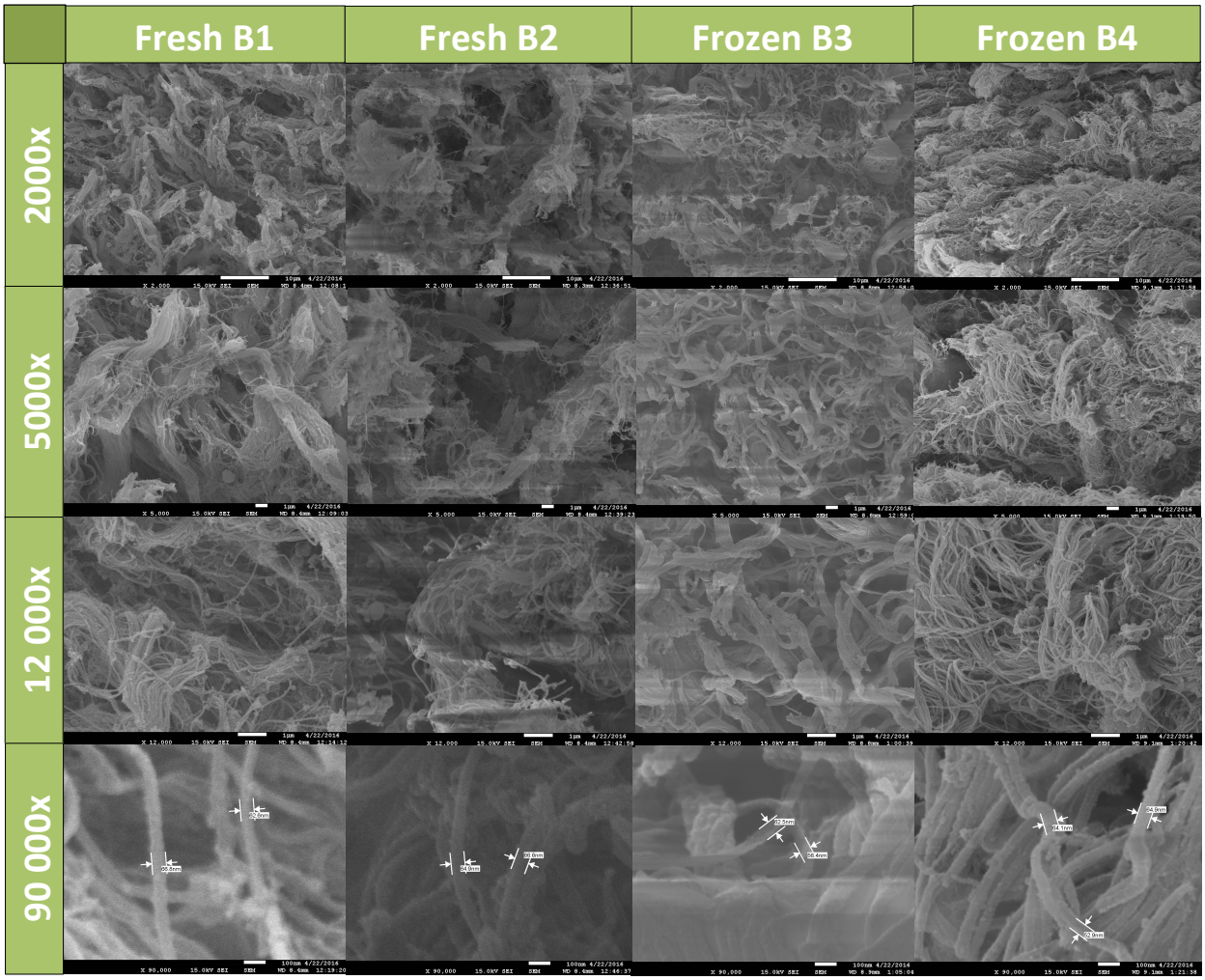

Figure 6.4: SEM pictures of two samples of fresh (Fresh B1 and Fresh B2) and of frozen-thawed (Frozen B3 and Frozen B4) bovine ovarian cortex, at four different magnifications (rows: 2000×, 5000×, 12 000× and 90 000×).

6.2 Physical properties: Rheology

6.2.1 Materials and Methods

Samples In the present study, two bovine ovarian fragments have been analyzed by rheology: a fresh one (Fresh B1) and a frozen one from a different cow (Frozen B3). Those samples came from the same ovaries than those analyzed by SEM, according to their name. Both samples have a minimum size of 8 x 8 mm, i.e. large enough for performing the rheological measurements.

Samples preparation The fresh fragment was analyzed directly after the biopsy collection, while the frozen sample, as previously explained, was stored at $-80°C$ until the day of the experiment. In order to defreeze it, several steps must be followed:

1. Remaining 2 min at RT,
2. Plunging 2 min at $37°C$ in a water bath,
3. Washing in MEM during 5 min, to remove the cryoprotectant, (3 times in a new Petri dish with fresh MEM).

Rheometer In the present study, the rheometer used for all the experiments is an Anton Paar Physica MCR 301. First of all, the sample must be charged into the rheometer. As our samples easily slip and must be kept wet, a special mounting has been worked out (Fig. 6.5(a) and 6.5(b)). Indeed, a Petri dish is pasted on the bottom plate of the rheometer and a piece of sandpaper is in turn pasted in the bottom of this plastic Petri dish. The container is then filled with an aqueous solution of MEM, or PBS, as already performed in previous reports [51]. The sample can be placed in the solution and the upper plate is moved down, in order to trap the specimen without crushing it, defining the gap. Once done, the sample chamber can be closed and the temperature, set at $37°C$. The gap's values for the bovine ovarian fragments are 1.6 and 2.2 mm for Fresh B1 and Frozen B3, respectively. Once the temperature stabilized, the manipulations can begin.

Protocol In order to perform rheological analyzes on all our samples and compare the results, a protocol has been established.

First an AS at very low deformations is performed from 0.1 to 4% and at a constant frequency (1 rad/s). This step is used to define the linear regime and to choose the deformation at which FS and TS will be performed. For fresh and frozen-thawed bovine fragments, a strain of 0.4% has been chosen. This step will be called *AS1* in the following. Then, a FS is carried out from 100 to 0.1 rad/s at 0.4%. This first step of measurement is named *FS2*. Thirdly, a double AS is done at high deformations from 0.1 to 100% (*First Round*) and from 100 to 0.1% (*Second Round*) at a frequency of 1 rad/s (*AS3*). Then, the next step depends on

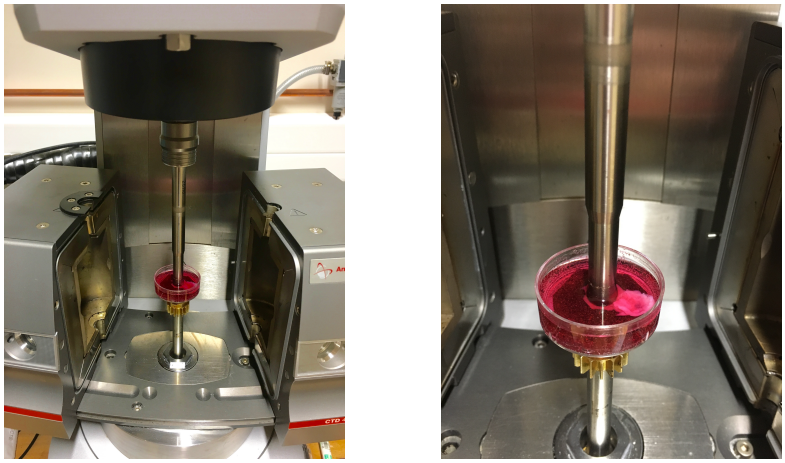

(a) (b)

Figure 6.5: Pictures of the experimental mounting used to analyze all the samples with the Anton Paar rheometer.

the look of AS3. Indeed, if the second round comes back at the G' plateau of the first round (Fig. 6.6(a)), a second double AS with the same parameters as for AS3 is performed (*AS4*). If not (Fig. 6.6(b)), a FS is done in order to let some time to the material to recover and then an AS4 is performed. For both specimens, a FS has be done between AS3 and AS4. After that, a third double AS is realized, still

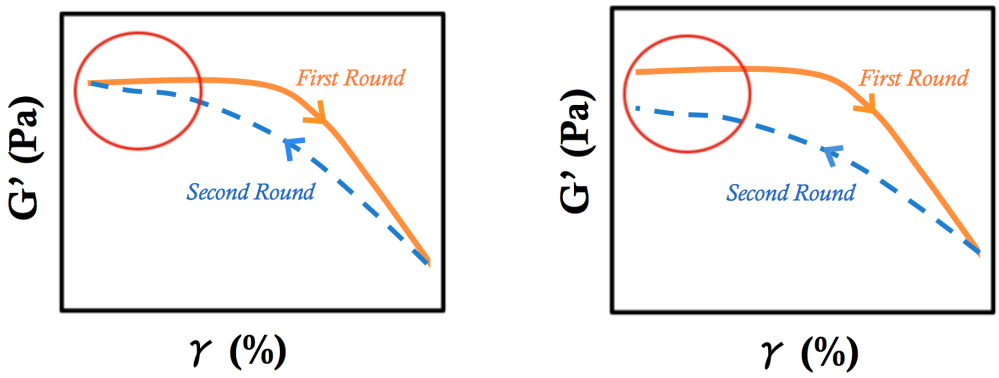

(a) (b)

Figure 6.6: Two possibilities of AS3 graphs. (a) The second round (dotted line) comes back to the storage plateau modulus of the first round (full line). (b) The second round (dotted line) does not come back to the storage plateau modulus of the first round (full line). Pictures adapted from [47].

with the same parameters as for AS3 (*AS5*). After those three AS, a FS is done in order to let some time to the material to recover with the same parameters as FS2

(*FS6*). Finally, a last double AS is performed, still with the same parameters as AS3 (*AS7*). In some cases, for supplementary tests, other AS[x2] have been added with the same parameters as for AS7 but with a different frequency (for example 5, 10 or 30 rad/s in place of 1) or with another maximum deformation (from 0.1 to 600% in place of 0.1 to 100%). The reason of those supplementary tests will be explained later.

Protocols applied to Fresh B1 and Frozen B3 are available in Table 6.2 and Table 6.3, respectively.

	Strain, γ (%)	**Frequency, ω (rad/s)**	**# Pt./dec**
AS1:	$0.01 \rightarrow 4$	1	4
FS2:	0.4	$100 \rightarrow 0.1$	4
AS3:	$0.1 \rightleftarrows 100$	1	10
FS:	0.4	$100 \rightarrow 0.1$	4
AS4:	$0.1 \rightleftarrows 100$	1	10
AS5:	$0.1 \rightleftarrows 100$	1	10
FS6:	0.4	$100 \rightarrow 0.1$	4
AS7:	$0.1 \rightleftarrows 100$	1	10
AS8:	$0.1 \rightleftarrows 100$	5	10

Table 6.2: Protocol followed for rheological analyzes on fresh bovine ovarian fragment (Fresh B1). All the tests were performed at 37°C.

6.2.2 Results and discussion

Once rheological analyzes performed, the results obtained for both bovine samples were plotted. However, in order to simplify the results and discussion, only some of the tests mentioned in Tables 6.2 and 6.3 are presented. Indeed, for all rheological analyzes performed in the present master thesis, only four graphs will be exposed, namely: (1) the first amplitude sweep, AS1, (2) FS2 superimposed to FS6, (3) AS3 superimposed to AS4 and (4) AS3 superimposed to AS7. The reason of this choice will be explicited soon. Furthermore, graphs (3) and (4) have been divided in two, one for G' and G" versus γ and another one for δ versus γ in order to lighten the

	Strain, γ (%)	**Frequency, ω (rad/s)**	**# Pt./dec**
AS1:	$0.1 \rightarrow 4$	1	4
FS2:	0.4	$100 \rightarrow 0.1$	4
AS3:	$0.1 \rightleftarrows 100$	1	10
FS:	0.4	$100 \rightarrow 0.1$	4
AS4:	$0.1 \rightleftarrows 100$	1	10
AS5:	$0.1 \rightleftarrows 100$	1	10
FS6:	0.4	$100 \rightarrow 0.1$	4
AS7:	$0.1 \rightleftarrows 100$	1	10

Table 6.3: Protocol followed for rheological analyzes on frozen-thawed bovine ovarian fragment (Frozen B3). All the tests were performed at 37°C.

charts and make them therefore, easier to read.

Moreover, for the ease of the interpretation of these rheological results, histograms will be presented and used for the discussion part. Further informations can be found in appendix B, which presents, for every analyzed sample, the six rheological graphs cited above. Eventhough those graphs won't be explained for each sample, some of them will be discussed, as example to illustrate the protocol and to manage the interpretation of all the other graphs provided in Appendix B. The six rheological graphs obtained from Fresh B1 and Frozen B3 are available in Appendix B, Fig. 2 and 3, respectively. Moreover, considering the number of samples studied in this work, Table 3 (Annexe A) provides a summary of all the samples analyzed by rheology.

AS1

As explained, AS1 (Fig. 6.7) is performed to define the strain at which the FS will be performed, called the working strain. This value needs to stand in the linear regime, meaning, as a reminder, the region where G' modulus is constant. An AS is thus performed at low deformations (from 0.1 to 4%) to avoid damaging the material[2]. As shown in Fig. 6.7, for Fresh B1, a working value of 0.4% has been

[2]While comparing the data presented in Table 6.2 and Fig. 6.7, a difference can be noted between the deformation range of AS1, going from 0.01 to 4% in the table and from 0.075 to 3.8% in the figure. This dissimilarity comes from the fact that on one hand, the points from 0.01 to

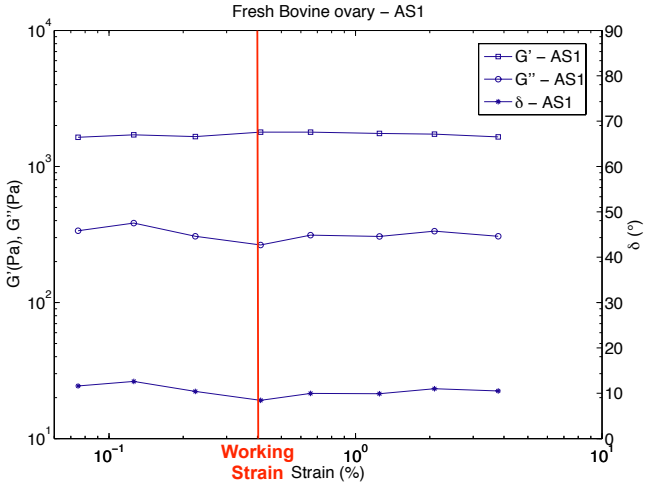

Figure 6.7: Amplitude sweep, AS1, at T =37 °C, $\omega = 1$ rad/s and with a strain going from 0.075 to 3.8%, applied on a fresh fragment of bovine ovarian cortex (Fresh B1). The working strain has been set at 0.4%. Squares stand for G', circles for G" and stars for δ.

chosen. The criterium used to select the right strain is to choose the nearest strain from the end of the linear regime. Indeed, the detection threshold of the rheometer being around 0.01% of deformation, low strains are not advised, in order to assure good and trustworthy results. On the opposite, choosing a value too close to the non-linear regime is risky. For this reason, a compromise is generally done between those two boundary cases. Thus, for all samples is this study, the working strain has been chosen following this reflexion, namely, the nearest as possible from the beginning of the non-linear regime, to ensure a good signal.

FS2/FS6

The second graph brings together FS2 and FS6 (Fig. 6.8). Those two tests have been chosen to visualize the impact of the two AS[x2] which have been performed between FS2 and FS6 (Table 6.2).

This graph can be compared with the theorical one from section 5.2.4 (Fig. 5.12). The similarities between those charts are the presence of a plateau in G' and G" and the parallelism between G' and G" curves. Indeed, while the G' and G"

0.075% were not realistic due to the noise and have therefore been hidden and on the other, the test has been stopped at 3.8% as the data were sufficient to define the working strain, allowing thus to gain time.

moduli go down at low frequencies for theoritical viscoelastic polymer able to flow, it is not the case for the bovine ovarian cortex. The precise structure and composition of the bovine ECM being not well known at present, no real conclusion can be made but a good hypothesis would be that the crosslinkings inside of the ECM avoid it to flow compared to typical viscoelastic polymers. This hypothesis can be reinforced by δ values, lying always between 0 and 15° which means that the material behaves more like a solid and thus, does not tend to flow. Besides this, in Fig. 5.12, a small

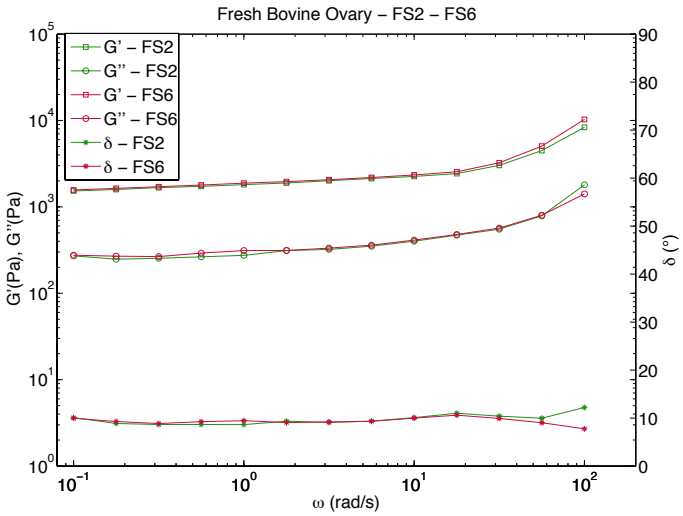

Figure 6.8: Frequency sweeps, FS2 (*Green*) and FS6 (*Red*), applied on a fresh bovine ovarian fragment (Fresh B1) at T = 37 °C, $\gamma = 0.4\%$ and ω = 100-0.1 rad/s. Squares stand for G', circles for G" and stars for δ.

decrease of G' and G" moduli can be observed at high frequencies, as well as in Fig. 6.8. Whereas this decrease is known to be due to friction between monomer units in theorical models, it is, at present, not possible to reach to same conclusion for bovine fragments, even if the same behavior is revealed by Fig 6.8, due to lack of informations regarding the matrix structure.

Finally, the superimposition of FS2 and FS6 allows to see no major difference between G', G" or even δ, respectively. This absence of difference means that the sample did not undergo major structural damages or deformations during the AS[x2] or at least, that it has been able to recover its initial properties.

AS3/AS4 and AS3/AS7

The third interesting graph is the one superimposing AS3 (in orange) and AS4 (in green) (Fig. 6.9(a)). As visible on this picture, the AS3 G' plateau is approximalety at 2.10^3 Pa.

A hysteresis is present between AS3 FR and SR, meaning that some bonds have been broken and can be reformed when decreasing the deformation. Besides this, the SR of G' does not come back at the same G' value as the first FR data which implies that the material did not fully recover its initial properties. In order to

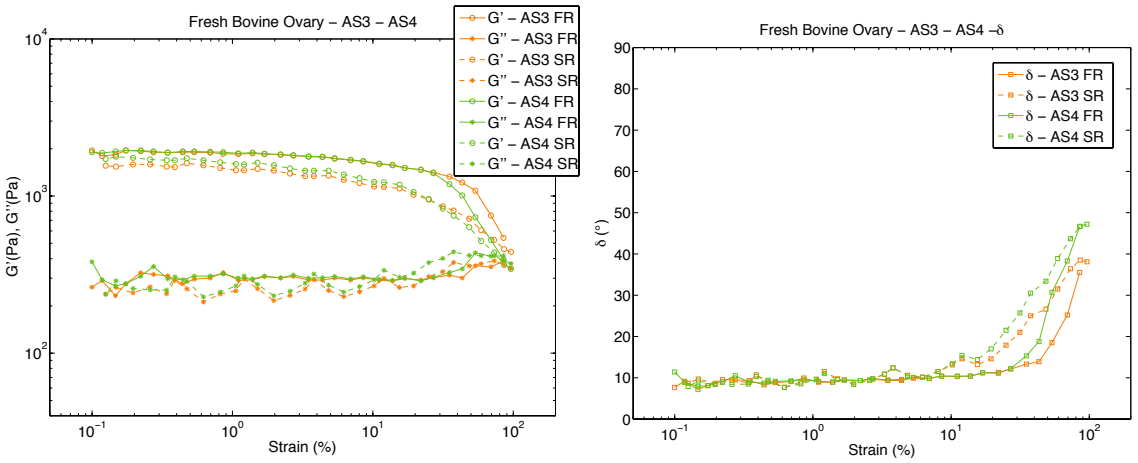

(a) (b)

Figure 6.9: Amplitude sweeps, AS3 (*Orange*) superimposed to AS4 (*Green*), applied on a fresh bovine ovarian fragment (Fresh B1) at T = 37 °C, $\omega = 1$ rad/s and with a strain going from 0.01 to 100% (solid lines, *First Round, FR*) and from 100 to 0.01% (dotted lines, *Second Round, SR*). (a) Circles stand for G' and stars for G", (b) squares stand for δ.

check if those modifications are reversible or not, AS4 is superimposed on the same rheological graph. As mentioned in Table 6.2, a FS has been performed between the two AS to let some time to the matrix to recover, if possible. As a result, the AS4 G' plateau (Fig. 6.9(a) in green) is at the same height as AS3 one meaning that the material has recovered its initial stiffness. However, the decrease of G' occurs at smaller strain amplitude compared to AS3, which involves that the material is less resistant to the deformation than during the first AS[x2].

In addition to the level of the G' plateau and the decrease of G towards the non-linear regime, another interesting factor can be extracted from this figure, namely

the crossover strain, also called relaxation point. Indeed, this event is characterized by the crossing between G' and G" curves both at FR and SR. This point accounts for the relaxing of the polymer because the viscous modulus, standing for the liquid part of the viscoelastic material, surpasses the elastic one, representing the solid part. For this sample, no intersection occurs for AS3. It would probably have occured if the deformation went above 100%. However, this crossover happens for AS4 because the material starts to flow more easily due to AS3 that sollicitated it.

As previously mentioned, the δ curves have been separated from G' and G" graphs (Fig. 6.9(b)). These two graphs (Fig. 6.9(a) and 6.9(b)) are well correlated with each other. Indeed, at small strains, δ lies around 10°, then gradually increases at high strains due to the rising sollicitation of the sample which tends to react more and more like a liquid. Nevertheless, compared to typical viscoelastic polymers, the bovine matrix does not flow, at least at those deformations, which explains the fact that δ does not overcome 50°. This behavior stands as well for AS3 as AS4.

AS3 and AS7 (see Appendix B, Fig. 2(e) and 2(f)) can be compared following the same reflexion.

Finally, a remark could be done about the exactitude of those AS3 and AS4 graphs. Indeed, the zigzag shape of G" SR is not physically possible. To overcome this problem and check if its origin was coming from the sample itself or from the rheometer, a supplementary AS has been performed after AS7 at higher frequency (see AS8 in Table 6.2 and Fig. 6.10). At 5 rad/s, those unexpected variations disappear, meaning that they were due to noise linked to the rheological measurements.

Histograms

Four major criteria of AS graphs have been chosen and presented in histograms to ease the interpretation of the results. Those four factors, already evoked in the paragraph "AS3/AS4 and AS3/AS7", are : (1) the level of G' plateau, called the **Storage plateau modulus**, (2) the strain marking approximately the end of the linear regime and therefore the decrease of G', named the **Yielding strain**, (3) the strain value of the crossover between G' and G" at FR and SR, called **G', G"**

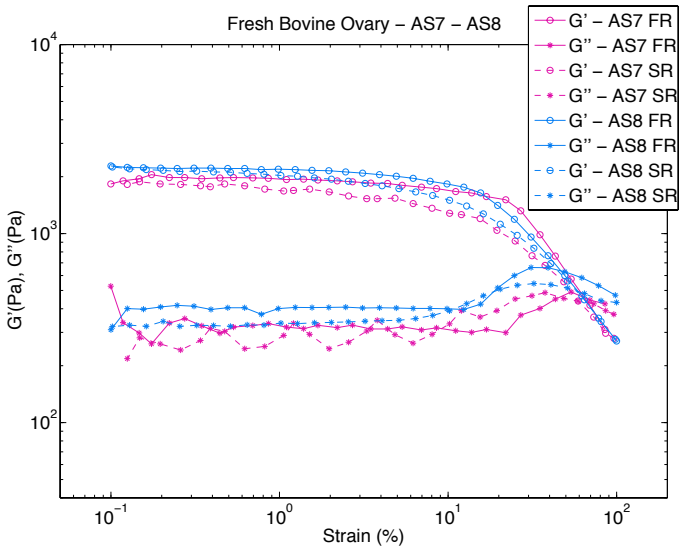

Figure 6.10: Amplitude sweeps, AS8 (*Blue*) with $\omega = 5$ rad/s and AS7 (*Pink*) with $\omega = 1$ rad/s, applied on a fresh bovine ovarian fragment (Fresh B1) at T = 37 °C and with a strain going from 0.01 to 100% (solid lines) and from 100 to 0.01% (dotted lines). Circles stand for G' and stars for G".

crossover and finally, (4) the importance of hysteresis of the considered AS, named **Hysteresis between first and second G' rounds**.

These four notions will be briefly explicited one by one along with the way they were computed.

The first one, namely the storage plateau modulus, represents the constant value of G' in the linear regime (Fig. 6.11, in purple). This value gives an idea of the rigidity of the material.

The yielding strain is represented on this same graph (Fig. 6.11, in blue) and has been systematically calculated as the x-coordinate of the intersection between two lines: the extension of the storage plateau modulus and the slope of the decrease of G', linking the last and the second-to last points of G' FR.

The third factor is the crossover between G' and G" and is described on Fig. 6.12. Two crossovers are represented, the one resulting from the intersection of the two full lines and of the two dotted lines, named crossover FS and crossover

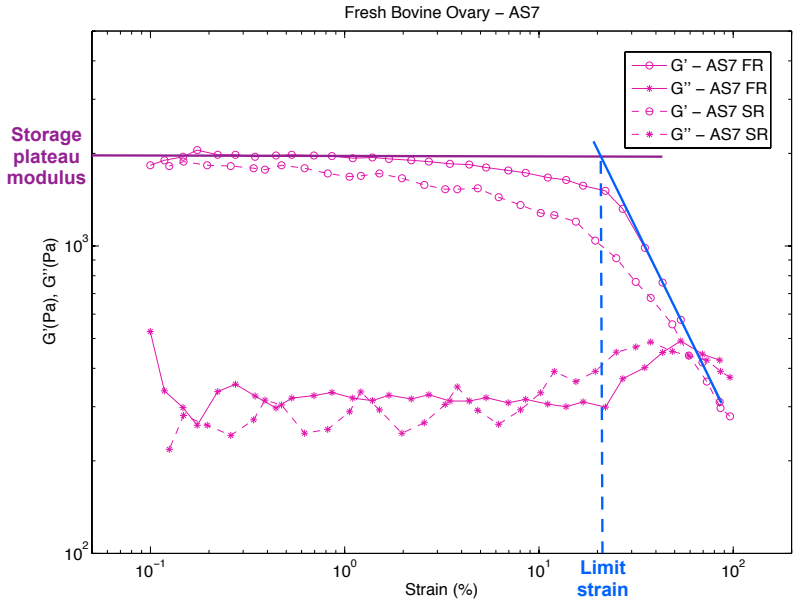

Figure 6.11: Representation of the storage plateau modulus and the yielding strain on an amplitude sweep graph, AS7, applied on a fresh bovine ovarian fragment (Fresh B1) at T = 37 °C, ω = 1 rad/s and with a strain going from 0.01 to 100% (solid lines) and from 100 to 0.01% (dotted lines). Circles stand for G' and stars for G".

SR, respectively. Those points will be used to compare the relaxation points of the different materials.

Finally, the hysteresis between the FR and the SR of an AS is computed as the difference between G'(1) and G'(2) (Fig. 6.13). Those two values are the y-coordinates of the intersection points between G' FR and G' SR and the line M, respectively. This vertical line is right in the middle (in logarithmic coordinates) of the x-coordinates of the yielding strain and the last point (LP) of G' FR.

Comparison between fresh and frozen bovine ovarian samples

Now that all the necessary background has been reviewed, the comparison of the rheological results of the fresh and frozen fragments of bovine ovarian cortex can be performed. The four histograms have been plotted in Fig. 6.14, based on rheological graphs of Fresh B1 (see Appendix B, Fig. 2) and Frozen B3 (see Appendix B, Fig. 3).

While looking at the storage plateau modulus graph (Fig. 6.14(a)), it can be

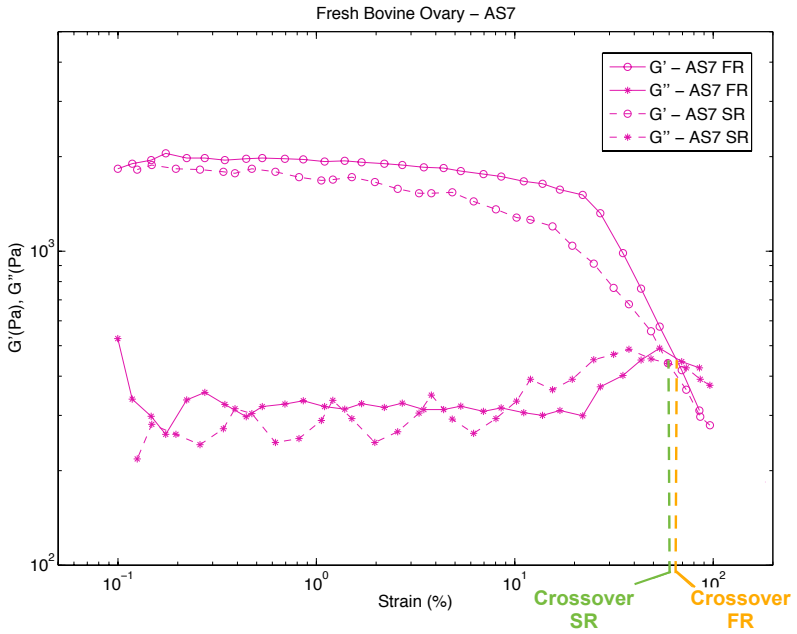

Figure 6.12: Representation of the G'-G" crossovers on an amplitude sweep graph, AS7, applied on a fresh bovine ovarian fragment (Fresh B1) at T = 37 °C, $\omega = 1$ rad/s and with a strain going from 0.01 to 100% (solid lines) and from 100 to 0.01% (dotted lines). Circles stand for G' and stars for G".

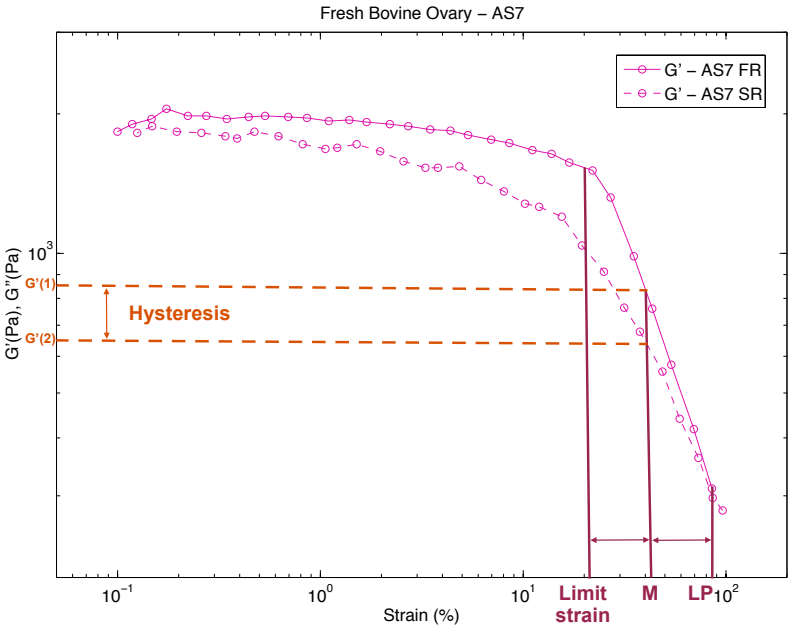

Figure 6.13: Representation of the hysteresis between AS7 FR and SR, applied on a fresh bovine ovarian fragment (Fresh B1) at T = 37 °C, $\omega = 1$ rad/s and with a strain going from 0.01 to 100% (solid lines) and from 100 to 0.01% (dotted lines). Circles stand for G' and stars for G".

easily noticed that the AS3 plateau is higher for Fresh B1 ($\sim$ 1900 Pa) than for Frozen B3 ($\sim$ 1200 Pa), indicating the higher rigidity of Fresh B1. In both cases, these stiffness values are quite low compared to other biological entities, which makes the ovaries defined as soft tissues. In addition to the fact that this dissimilarity is far from being of an order of difference, nothing can prove if it is due to the difference between the fresh or frozen-thawed state of the sample, to the variability from one animal to another, or due to the cortex heterogeneity. Indeed, as demonstrated by Wood et al. [51], the simple presence of pieces of corpus luteum can greatly increase the rigidity of a sample. Moreover, a comparison between two fresh samples, Fresh B1 and Fresh B2, has been realized and an even larger difference regarding storage plateau moduli than between Fresh B1 and Frozen B3 was measured, going from $\sim$ 1900 Pa for Fresh B1 to $\sim$ 4300 Pa for Fresh B2 (see Appendix B, Fig. 1). On the other hand, the small differences between AS3, AS4 and AS7 plateaus of both Bresh B1 and Frozen B3 indicate the good recovery of the material, and the bonds reversibility inside of the matrix, after being deformed at high strains.

While comparing the yielding strains (Fig. 6.14(b)), a great similitude can be noticed between Fresh B1 and Frozen B3 denoting their similar ability to break under a shear deformation. Furthermore, in both cases, a decreasing of yielding strain from AS3 to AS7 is visible. This characteristic can be explained by the fact that, due to previous AS[x2], the material is weakened and begins to break at smaller strains every time.

The same reflexion can be applied to Fig. 6.14(c). For both samples, crossovers happen at smaller strains every time a new AS[x2] is performed, due to the decreasing capacity of the material to resist the deformation. Nevertheless, for AS3 of Fresh B1, no crossover is observed meaning that the material did not yield and that a larger deformation should have been applied in order to break it. Moreover, while comparing the difference between Fresh B1 and Frozen B3, the same conclusion seems to appear as in Fig. 6.14(a): the crossovers occur at smaller deformations for Frozen B3 than Fresh B1.

Finally, the hystereses of the several AS of Fresh B1 and Frozen B3 are compared in Fig. 6.14(d). The hysteresis in AS3 can be explained by the presence reversible bonds inside of the material. The storage plateau moduli of AS3, AS4 and AS7 being of the same amplitude in both cases means that the broken bonds were able to reform and reorganize after a while, when looking at short length scales motions. On the other hand, the decreasing hysteresis amplitudes of AS3, AS4 and AS7 respectively, implies that the more the samples are deformed by consecutive AS[x2], the less they reorganize, due to the breaking of irreversible bonds, which takes place at a larger length scale. One possible explanation for such viscoelastic behavior is the breaking of the network into large clusters, able to move apart from each others. The height differences between Fresh B1 and Frozen B3 hystereses can be interpreted as coming from the fact that Frozen B3 is composed of less reversible bonds either due to the freezing-thawing process or simply due to the matrix composition varying from one sample/animal to another. Supplementary tests on more fresh and frozen bovine ovarian fragments should be performed in order to settle this hypotheses conflict.

Thus, considering the present results, no trustworthy conclusion can be made regarding the significant difference of physical behavior between fresh and frozen-thawed bovine ovarian samples. Indeed, it is not possible to declare, at this stage, either the differences or similitudes are due to the sample state, the matrix heterogeneity or the variability between animals. In order to do so, more samples should be analyzed and a statistical study should be performed. Furthermore, as for SEM analyzes, the fresh and frozen fragments should come from the same ovary, in order to remove the hypothesis of variability between animals. An even proper way to proceed would be to test a fresh bovine ovarian samples, then to freeze it, in order to test the same sample for fresh and frozen-thawed analyses and removind the hypothesis of matrix heterogeneity. But the inconvenient of this methode is that the sample will be deformed by several AS before to be frozen, which can influence the results when it will be tested as frozen sample.

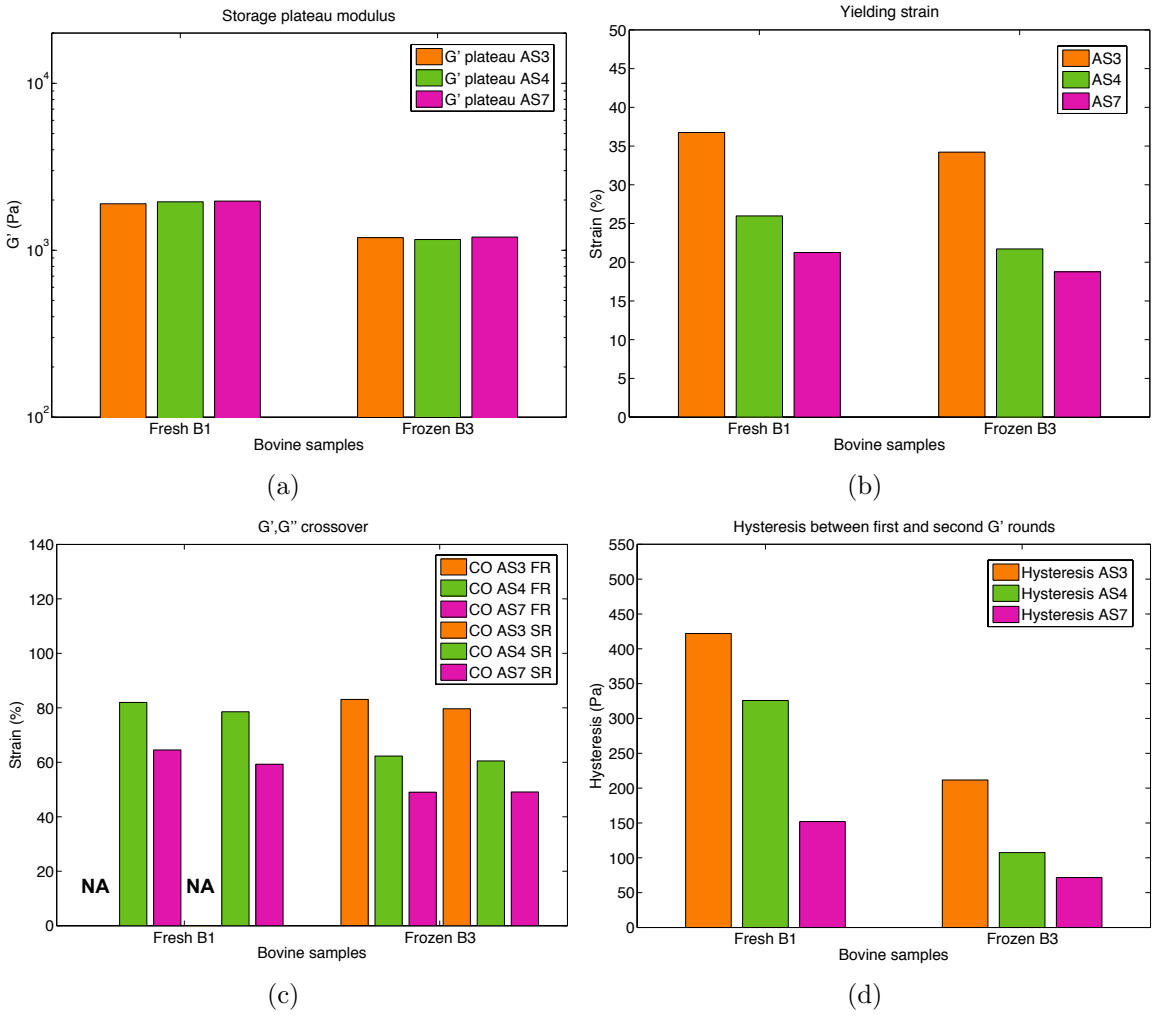

Figure 6.14: Comparison between fresh and frozen samples of bovine ovarian cortex. (a) Comparison of storage plateau moduli of AS3 (Orange), AS4 (Green) and AS7 (Pink). For Fresh B1, no crossover is observed for AS3 (NA stands for not applicable). (b) Comparison of yielding strains of AS3 (Orange), AS4 (Green) and AS7 (Pink). (c) Comparison of crossovers between G' and G" of AS3 (Orange), AS4 (Green) and AS7 (Pink) at first round (FR) or at second round (SR). (d) Comparison between the hysteresis of AS3 (Orange), AS4 (Green) and AS7 (Pink).

Chapter 7

Characterization of human ovarian tissue

7.1 Morphological properties: Scanning electron microscopy

7.1.1 Materials and Methods

Samples Four human ovarian samples were analyzed by SEM. The first patient (H4538) is 28 years old, the second one (H4544) 33, the third one (H4548) 34 and the last one (H4665) 31. Thus, all those unmenopaused patients are defined as young patients in the following.

Fixation See section 6.1.1. The samples were fixed directly after the biopsies collection.

Washing See section 6.1.1.

Cryofracture Human samples were cryofractured to see the intact structures inside. To do so, they are immersed in a solution of 30% glycerol in 0.1M PBS overnight in the fridge (4°C). The day after, they were plunged into liquid nitrogen and fracture.

Washing After that, in order to remove the cryofracture solution, the samples were washed in 0.1M PBS, three times during 5 minutes each. Each time, fresh PBS is put in new petri dishes.

Post-fixation with osmium See section 6.1.1.

Dehydration See section 6.1.1.

Drying with the CPD See section 6.1.1. Human samples underwent 6 cycles.

Gold Coating See section 6.1.1. Human samples were coated with a 10 nm gold film.

Scanning Electron Microscopy See section 6.1.1.

7.1.2 Results and discussion

As a reminder, a summary of all the samples tested by SEM is available in Table 2, Appendix A. The SEM pictures of the four different human ovarian fragments are shown in Fig. 7.2. In each case, a very dense, fibrous and inhomogeneous structure is visible composed of interlaced fibers, which is in correlation with informations found in the litterature [9].

The aim of these analyzes is to assess if there is an important variability from one human patient to another regarding the ovarian cortex's structure. As for SEM bovine pictures, four different magnifications are exposed in order to ease the comparison between the human patients. The fibers diameters measured are listed in the following table (Table 7.1).

	H4538	**H4544**	**H4548**	**H4665**
Fiber diameter (nm)	60.6/72.9/73.7	71.5/73.3	52.3/58.1/59.7/75.1	70.6

Table 7.1: Fibers diameters (in nm) of four human ovarian samples from different young patients, measured by SEM.

Similarly to bovine ovarian samples, the fibrous nature of the samples is mostly due to the high collagen content of the human ovarian cortex. However the precise structure and composition of human ovarian ECM are not well characterized, this matrix is known to be composed of collageneous (collagen type I, III, IV and VI) and noncollageneous proteins (laminin, fibronectin, hyaluronan,...). But the most abundant proteins of the ovarian ECM are fibrillar collagens and fibronectine. Collagen (Col) types I and III are fibrillar proteins, type VI a microfibrillar protein and type IV is the most abundant non-fibril forming collagen type, and lies principally in basement membranes. Fibronectins are insoluble high molecular weight adhesive glycoproteins of the ECM with the ability to bind other components such as collagens, fibrin, integrins or glycosaminoglycans. These proteins form homo- or heterodimers by disulfide bonds. [7, 28, 52, 53]

The most important collagen type, responsible of the fibrous structure of the ovarian ECM, is Col type I and is widely distributed in ovary and organizes in bundles of thick fibers. Col type III is present in blood vessels wall and copolymerizes with Col type I. Col type VI is believed to be involved in cell anchoring and signaling, and can also bind to other ECM proteins. [7, 28, 52, 53]

Fibrillar collagens are able to self-assemble into fibrils. The aggregation process is similar to the fibrin formation process. Indeed, soluble procollagens, which are secreted by ECM cells, are converted into collagen by a specific proteinase. The generated collagen self-assembles into fibrils, stabilized by covalent cross-linking due to the action of lysyl oxidase. Furthermore, it has been proved that collagen fibrils can be either unipolar or bipolar, which affects the mechanical and physical properties of the tissue. The mean diameter of these collagen fibrils has been proved to increase with maturation of the tissue. This last characteristic has not been demonstrated specifically for ovaries but for many other tissues, so it can be interesting to keep it in mind. [7, 28, 52, 53]

Speaking of the matrix composition, some small globular structures can be observed at the surface of the fibers while looking closer at some SEM pictures (Fig. 7.1). These elements are most probably not part of the natural human ovarian cortex

but might presumably be salt cristals coming from the SEM preparation procedure.

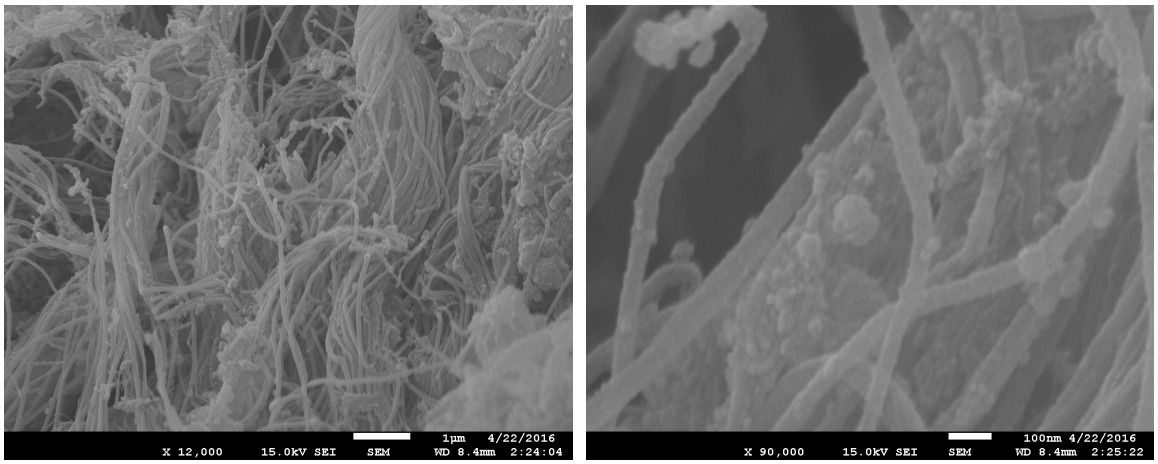

(a) (b)

Figure 7.1: SEM pictures of the human ovarian cortex from patient H4548, on which globular structures at the surface of the fibers are clearly notable, at different magnification: (a) 12 000× and (b) 90 000×.

Regarding the matrix porosity, for all human samples, pores of varying size are visible due to the compact and heterogeneous structure of the human ovarian cortex, avoiding to define an average pore diameter.

No major difference appears according to the fiber diameter of the several patients standing around 69.1, 72.4, 61.3 and 70.6 nm respectively for H4538, H4544, H4548 and H4565.

Considering all these informations, it can be concluded that no significant morphological difference exists from one patient to another. Therefore, the mean fiber diameter consituting the human ovarian cortex can be approximated at ~ 68 nm. Nevertheless, it is important to bear in mind that all the analyzed human fragments had preliminary be cryopreserved and then thawed before the analyzes.

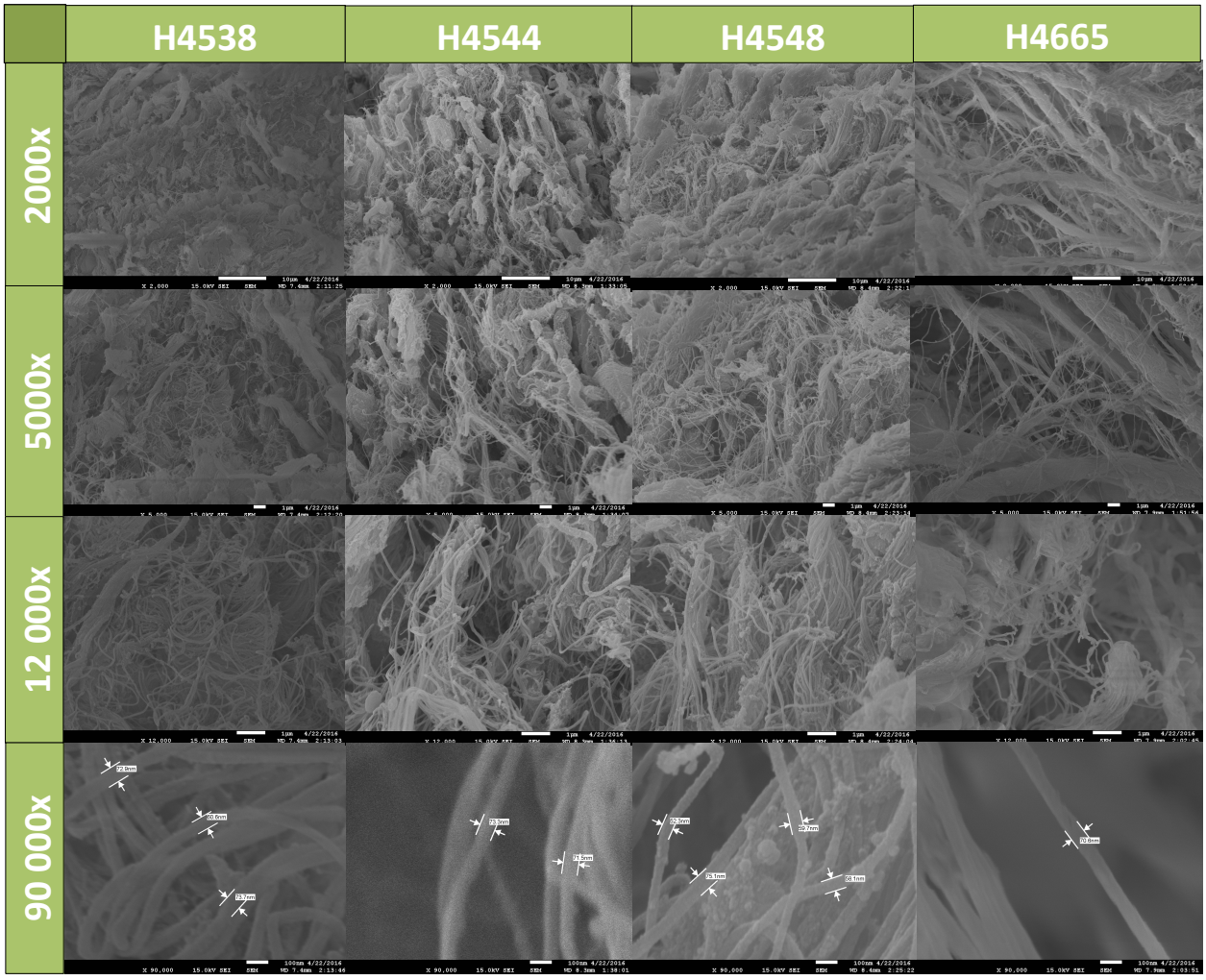

Figure 7.2: SEM pictures of the human ovarian cortex from four different patients (columns) at four different magnifications (rows).

7.2 Physical properties: Rheology

7.2.1 Materials and Methods

Samples As introduced in section 5.1, three kinds of human ovarian samples have been analyzed: small and large samples from a menopaused patient of 49 years old and a large one from a young patient of 25. The term "large" defines samples larger than 8×8 mm^2. The dimensions of the small sample were more or less $5\times6\times2$ mm.

Samples preparation All the samples were cryopreserved and kept at $-80°C$ until the day of the experiment due to the impossibility to perform the rheological analyzes in the same day as the biopsy collection. For the defreezing process, see

section 6.2.1.

Rheometer See section 6.2.1. The gap's values used to trap those samples are respectively, 1.3, 1.05 and 1.6 mm.

Protocol The small and large fragments from the menopaused patient were submitted to protocols summarized in Table 7.2 and 7.3, respectively. The protocol shown in Table 7.4 was applied to the large fragment from the young patient.

	Strain, γ (%)	**Frequency, ω (rad/s)**	**# Pt./dec**
AS1:	$0.1 \rightarrow 4$	1	4
FS2:	0.4	$100 \rightarrow 0.1$	4
AS3:	$0.1 \rightleftarrows 100$	1	10
AS4:	$0.1 \rightleftarrows 100$	1	10
AS5:	$0.1 \rightleftarrows 100$	1	10
FS6:	0.4	$100 \rightarrow 0.1$	4
AS7:	$0.1 \rightleftarrows 100$	1	10

Table 7.2: Protocol followed for rheological analyzes on the small human ovarian fragment from a menopaused patient. All the tests were performed at 37°C.

	Strain, γ (%)	**Frequency, ω (rad/s)**	**# Pt./dec**
AS1:	$0.1 \rightarrow 4$	1	4
FS2:	0.4	$100 \rightarrow 0.1$	4
AS3:	$0.1 \rightleftarrows 100$	1	10
FS:	0.4	$100 \rightarrow 0.1$	4
AS4:	$0.1 \rightleftarrows 100$	1	10
AS5:	$0.1 \rightleftarrows 100$	1	10
FS6:	0.4	$100 \rightarrow 0.1$	4
AS7:	$0.1 \rightleftarrows 100$	1	10

Table 7.3: Protocol followed for rheological analyzes on the large human ovarian fragment from a menopaused patient. All the tests were performed at 37°C.

	Strain, γ (%)	**Frequency, ω (rad/s)**	**# Pt./dec**
AS1:	$0.1 \rightarrow 4$	1	4
FS2:	0.3	$100 \rightarrow 0.1$	4
AS3:	$0.1 \rightleftarrows 100$	1	10
FS:	0.3	$100 \rightarrow 0.1$	4
AS4:	$0.1 \rightleftarrows 100$	1	10
AS5:	$0.1 \rightleftarrows 100$	1	10
FS6:	0.3	$100 \rightarrow 0.1$	4
AS7:	$0.1 \rightleftarrows 100$	1	10

Table 7.4: Protocol followed for rheological analyzes on the large human ovarian fragment from a young patient. All the tests were performed at 37°C.

7.2.2 Results and discussion

As a reminder, a summary of all the samples tested by rheology is available in Table 3, Appendix A. As announced in section 5.1, bovine ovarian fragments have been tested beforehand to ensure the feasibility of the experiments. Considering the consistency of the obtained rheological graphs, tests on human ovarian fragments have been performed. But, against all odds, a large fragment of young ovarian cortex was provided. Thus, in theory, compared to the announced strategy, ovarian fragments from menopaused patients were not useful anymore. Nevertheless, the present study should be performed on more than one young sample to ensure the reproducibility of the results and it is impossible to predict if other large samples from young patients will be, once more, available. For this reason, small and large samples from a menopaused patient have still be tested in order to establish a correction factor. This section will thus be divided in two: the comparison between the small and the large samples from the menopaused patient, and another one between the two larges samples. In order to highlight this section, samples will be called Human SM, Human LM and Human LY respectively for, the small sample, the large sample from the menopaused patient and the large sample from the young one. The six rheological graphs obtained for Human LM, Human SM and Human LY are available in Appendix B, Fig. 4, 5 and 6, respectively.

While comparing the storage plateau modulus of Human SM and Human LM (Fig 7.3(a)), a similitude in AS3/AS4/AS7 ratio[1] can be noticed along with the shifting of the plateau from $\sim$ 1400 Pa for Human LM to lower values for Human SM ($\sim$ 400 Pa). Considering the fact that the samples come from the same ovary, they should have approximately the same storage plateau modulus, bearing in mind the heterogeneous nature of the cortical ovarian ECM. This observation allows to state that the correction factor should raise the value of the storage plateau modulus obtained for small samples of more or less a factor 3-4, in order to fit with the real sample's rigidity. Nevertheless, more tests should be perfomed in order to confirm this number.

If comparing the storage plateau modulus of Human LM and Human LY (Fig 7.3(a)), no major difference is visible. This suggests that samples from menopaused and young ovarian cortex have approximately the same rigidity. This conclusion is in contradiction with the initial hypothesis stated in the strategy. This fact could actually be true as the initial hypothesis was only built up from an intuition and that no study has never proved its reliability. Nevertheless, supplementary tests should be performed to check the reproducibility of this phenomenon and ensure that it is not a one time observation coming from the heterogeneity of the matrix.

In all cases, the small variations between AS3, AS4 and AS7 plateaus suggest the good recovery of the samples and the bonds reversibility inside of the matrix after being deformed at high strains.

The comparison between yielding strains of Human SM and Human LM (Fig 7.3(b)) does not show a significative difference, considering the existing variability from one sample to another. This suggests that the correction factor should not affect the yielding strain.

On the contrary, a difference in yielding strain is noticeable between Human LM and Human LY (Fig 7.3(b)), indicating that the young matrix is less able to

[1]This ratio means the height difference between AS3, AS4 and AS7, within a sample, which is only a qualitative notion based on visual analyzes of the graphs.

resist the deformation than the menopaused one.

Morever, the AS3/AS4/AS7 ratio stays more or less the same for all samples. This means that the material is able to recover rapidly its initial properties after having been largely deformed and therefore forced to flow. This recovery property suggests that large deformations do not create permanent damage in the sample.

If no large difference in crossover values (Fig. 7.3(c)) can be noticed between Human SM and Human LM except for AS3, a quite important dissimilarity can be stated for the AS3/AS4/AS7 ratio. Regarding these data, it is impossible to know if this difference is due to matrix heterogeneity or, if the correction factor should modify this results too.

On the contrary, a large difference can be noticed between Human LM and Human LY (Fig. 7.3(c)). This enhances the hypothesis made for the yielding strain graph according to which the young fragment seems to be less resistant to the deformation than the menopaused one, as it flows at significantly smaller strains. However, this difference could be also due to the slippage of the small sample. Considering the small height difference between the several AS's crossover, the young one seems to recover better than the menopaused one.

Finally, regarding the last graph (Fig. 7.3(d)), a huge difference appears between the Human SM and Human LM hystereses, with a rising of more or less a factor 100. This observation makes the establishment of a correction factor way more complex. Indeed, except for the storage plateau modulus, the other factors do not differ strongly between Human SM and Human LM, therefore a simple correction, such as a shift toward higher values, could have been sufficient in order to correct the size problem. But this hysteresis comparison suggests that another process takes place, which must be taken into account in order to be able to compare the data and therefore, determine the correction factor.

While comparing the hystereses of the two large samples (Fig. 7.3(d)), approximately the same difference can be noticed than between the two samples from the menopaused patient. This could mean that Human LM is made of more breakable

bonds compared to Human LY. On the opposite, Human LY AS4 hysteresis is higher than AS3 one, indicating that the material reorganized better than before, and the small ratio indicates that it would be made of more reversible bonds.

In summary, the present results suggest that, under the well-defined protocol of sample loading used is this study, a raising of the results from low to high G' value of a factor 3-4 should be applied in order to fit with the real small sample properties. Besides, the size modification does not significantly affect the yielding strain or the G'-G" crossover, while it appears to decrease by a factor 100 the hysteresis. Nevertheless, in order to compute a correction factor, more tests need to be performed on more samples.

Regarding the difference between young and menopaused ovarian tissue, the major conclusion is that no rigidity difference is noticed, against all odds. Moreover, the young matrix seems to be less resistant to shear deformations but to recover better than the menopaused one. Finally, both matrices seem to be composed of many reversible bonds.

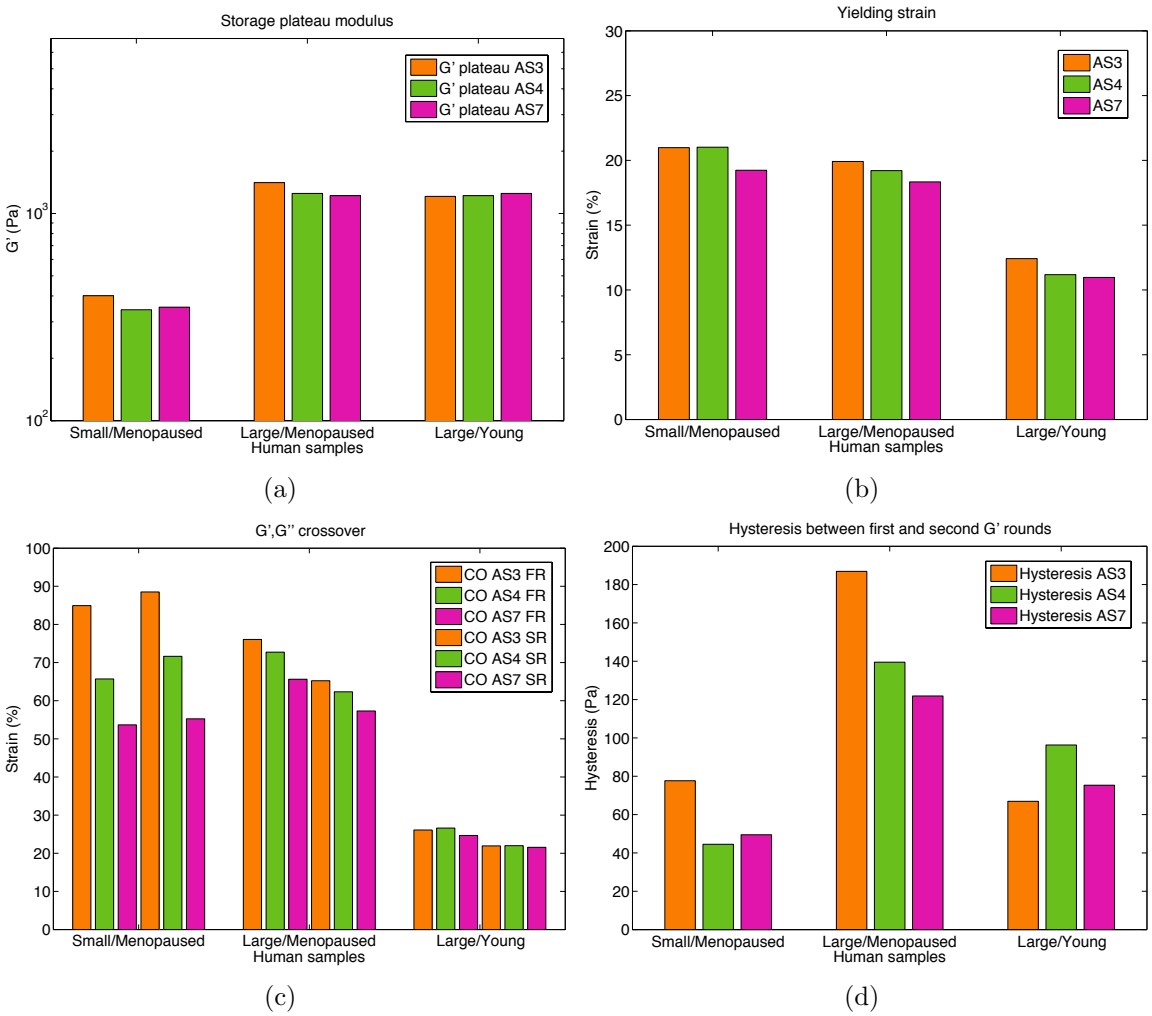

Figure 7.3: Comparison between three fragments of human ovarian cortex. (a) Comparison of the storage plateau modulus of AS3 (Orange), AS4 (Green) and AS7 (Pink). (b) Comparison of the yielding strain of AS3 (Orange), AS4 (Green) and AS7 (Pink). (c) Comparison of the cross-over between G' and G" of AS3 (Orange), AS4 (Green) and AS7 (Pink) at first round (FR) or at second round (SR). (d) Comparison between the hysteresis of AS3 (Orange), AS4 (Green) and AS7 (Pink).

Chapter 8

Development of a matrix: Fibrin gels

8.1 Morphological properties: Scanning electron microscopy

8.1.1 Materials and Methods

Fibrin clot formation The fibrin clots are formed using the Tissucol kit from Baxter. Tissucol is a two-component fibrin sealant that replicates the last step of the natural blood-clotting cascade (Fig. 8.1) [36]. This kit contains several components:

- A powder containing human fibrinogen, human fibronectin, human factor XIII and human plasminogen,
- A solution of bovine aprotonin (3 000 kU/mL), a fibrinolysis inhibitor,
- A powder of human thrombin,
- A solution of $CaCl_2$ (40 mM).

To reconstitute the thrombin and fibrinogen solutions, several steps need to be followed. First the aprotonin solution is mixed with the fibrinogen powder and kept at $37°C$ for 20 minutes in order to obtain a homogeneous solution. A small magnet is also present in the fibrinogen bottle to agitate the two components and thus ease

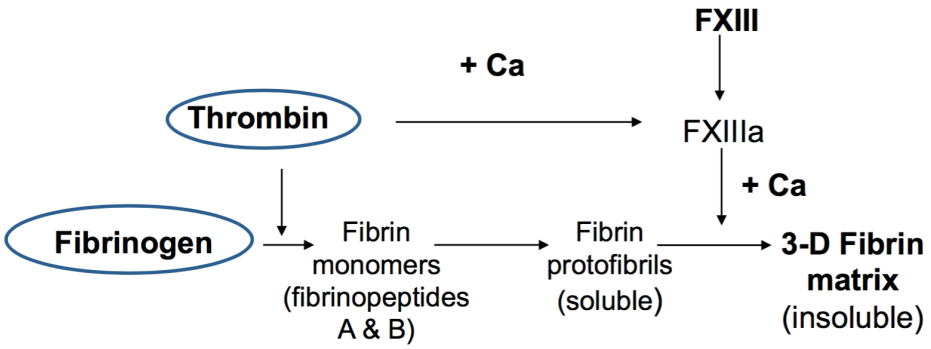

Figure 8.1: Last step of the natural blood-clotting cascade [36].

their mixing. At the end, a solution of fibrinogen 100 mg/ml is obtained (F100). Then, the $CaCl_2$ solution is mixed with the thrombin powder and kept at $37°C$, the concentration of the obtained solution is 500 U/ml (T500). A saline solution containing 9 g/L of sodium chloride (0.9 % $NaCl$) is added to the F100 to reach the final concentrations: 75 mg/ml, 50 mg/ml, 30 mg/ml and 12.5 mg/ml. In the same way, a solution of $CaCl_2$ 40 mM is added to the T500 to dilute it and reach the final concentrations: 75 U/ml, 50 U/ml and 1 U/ml. Then, in order to reach the four different fibrin formulations tested in the present study (Table 8.1) and to make fibrin clots of 200 μl, 100 μl of the desired fibrinogen concentration is withdrew in a pipette and 100 μl of the corresponding thrombin concentration in another one. The two solutions are then ejected at the same time on a glass Petri dish, the formed clot is picked up again and quickly ejected in order to mix the components. Finally, the droplet is incubated for 15 minutes at $37°C$ in an incubator. Considering the small fibrinogen and thrombin concentrations of the F12.5/T1 gel, this one needs to incubate 45 minutes in place of 15. [27]

Sample's name	**Fibrinogen (mg/ml)**	**Thrombin (U/ml)**
F12.5/T1	12.5	1
F30/T50	30	50
F50/T50	50	50
F75/T75	75	75

Table 8.1: Composition of the four different fibrin gels tested by SEM.

Fixation See section 6.1.1.

Washing See section 6.1.1.

Cutting Fibrin samples, once fixed, were cutted with a very sharp blade by shearing them without crushing them.

Post-fixation with osmium See section 6.1.1.

Dehydration See section 6.1.1.

Drying with the CPD See section 6.1.1. Fibrin hydrogels underwent 8 cycles.

Gold Coating See section 6.1.1. Fibrin samples were coated with a 10 nm gold film.

Scanning Electron Microscopy See section 6.1.1.

8.1.2 Results and discussion

As a reminder, a summary of all the samples tested by SEM is available in Table 2, Appendix A. The SEM pictures of the four fibrin gels of different formulations are presented in Fig. 8.4. The aim of this experiment is to compare those four structures and check if the impact of varying fibrinogen and thrombin concentrations is coherent with the one found in the litterature (see section 4). To do so, the fibers diameters are synthetized in the above table (Table 8.2).

	F12.5/T1	**F30/T50**	**F50/T50**	**F75/T75**
Fibers diameter (nm)	100/110/139/201	89/98.4/115	62.9/66.1	44.8/70.9/80.4

Table 8.2: Fibers diameters of fresh four fibrin samples measured by SEM.

First, it can be seen that the fibrillar nature of the fibrin network, formed by the reaction between thrombin and fibrinogen, is well exhibited in all pictures. Moreover, all matrices are highly homogeneous and the fibrin formulation does not have an impact on this homogeneity, which is in agreement with the litterature [54].

Moreover, as for human samples, the fibrin fibers seem to have a globular structure (Fig. 8.2). But, considering the difference in composition between those two samples, this reinforced the hypothesis that those globular structures are probably, salt cristals, due to SEM preparation.

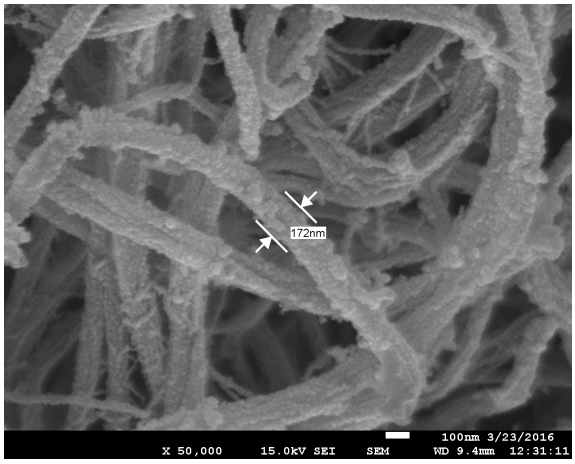

Figure 8.2: SEM picture of a sample of fibrin hydrogel 12.5/T1, on which globular structures at the surface of the fibers are clearly notable. Picture taken at a magnification of 50 000×.

As mentioned in the protocol, the fibrin samples have been cut with a sharp blade in order to see the internal structure. The reason and necessity of this step can be eaily understood while looking at Fig. 8.3, showing a crust a the sample's surface.

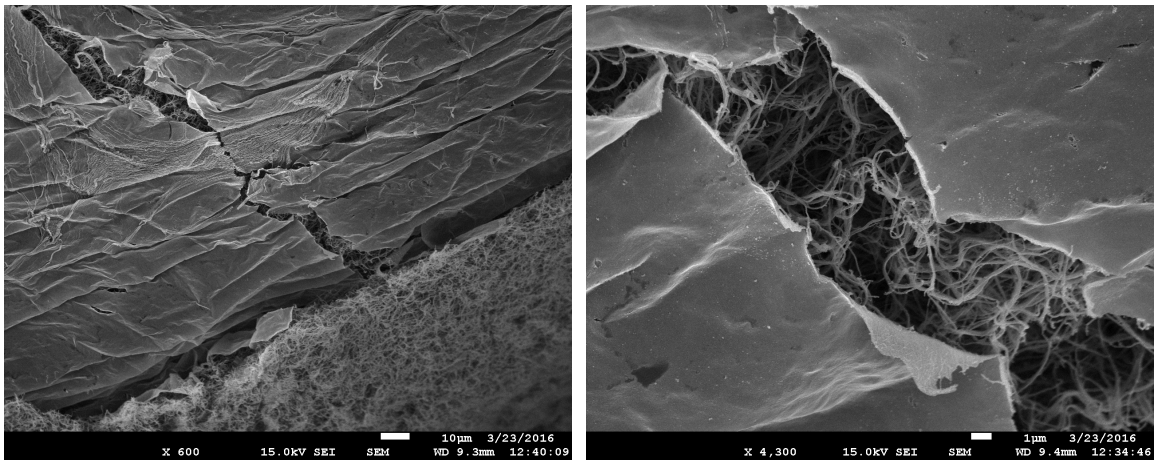

(a) (b)

Figure 8.3: SEM pictures of a fibrin hydrogel F12.5/T1, on which the crust present at the surface is well visible, at different magnifications: (a) 600× and (b) 4300×.

Even though the matrix porosity slighlty varies within a single sample, the observations that can be made about the porosity variation while modifying the fibrin formulation are in perfect correlation with the litterature (see section 4). Indeed, the higher the fibrinogen and thrombin concentrations (from F12.5/T1 to F75/T75), the smaller the porosity.

Moreover, the fibers diameters of the fibrin samples (Fig. 8.4, last row, and Table 8.2) are also correlated with the informations found in many articles: the higher the thrombin concentration, the thiner the fibrin fibers. Indeed, the mean fibers diameter stands around 138, 101, 65 and 58 nm, for F12.5/T1, F30/T50, F50/T50 and F75/T75, respectively. For F75/T75, only a few thick fibers formed by the aggregation of thin fibrin fibers are found (Fig. 8.4, last row, last column, thick fiber of 80 nm).

In summary, many morphological differences appear between the four fibrin formulations, all in agreement with the litterature. First, the porosity is inversely correlated with fibrinogen and thrombin concentrations. Secondly, the thickness of the fibers are inversely correlated with thrombin concentration. Nevertheless, some rare thick fibers are still noticed in the higher formulations. Finally, all formulations show a high homogeneity.

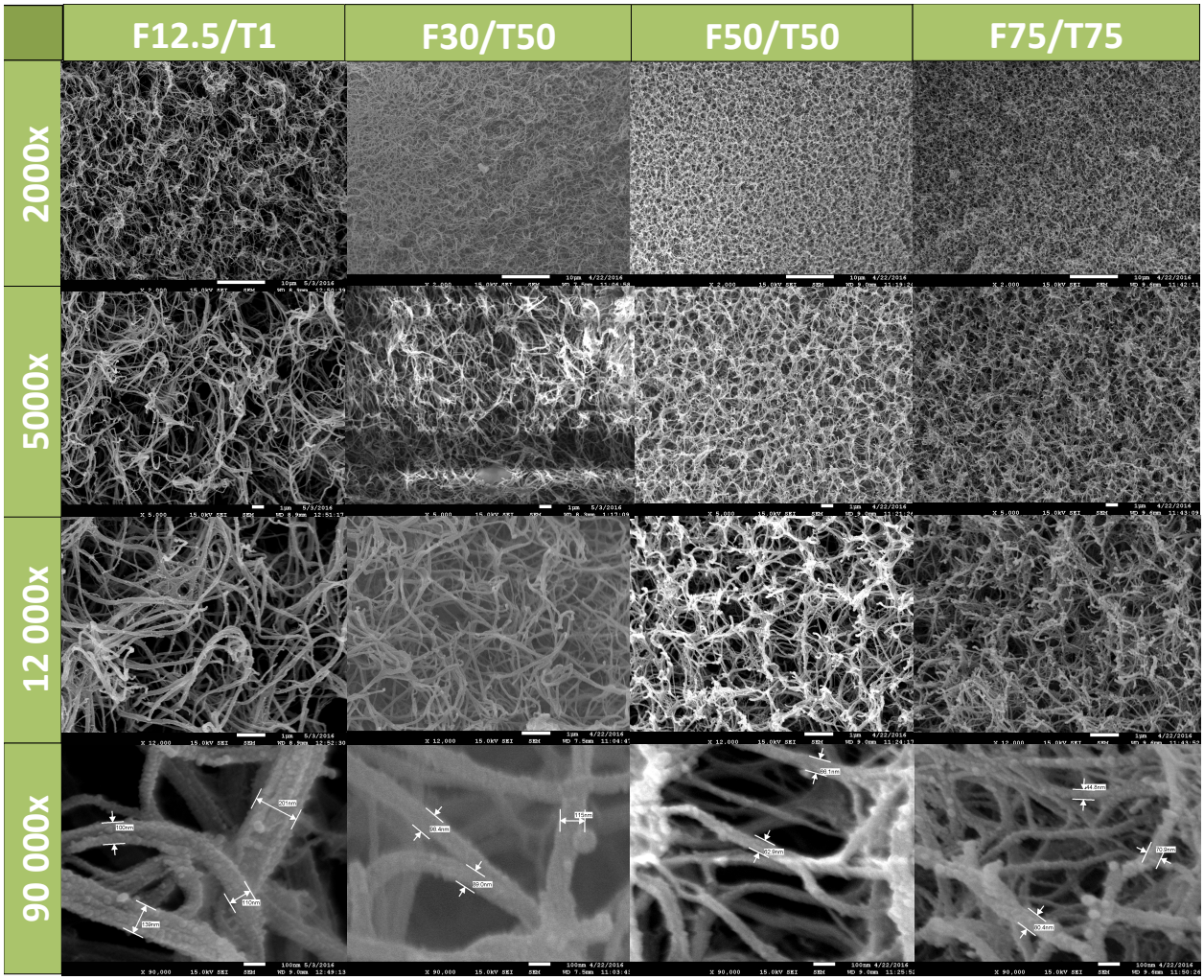

Figure 8.4: SEM pictures of fibrin hydrogels of four different concentrations (columns), at four different magnifications (rows).

8.2 Physical properties: Rheology

8.2.1 Materials and Methods

Samples Five different samples have been analyzed: one clot of F12.5/T1 (200 μl), one clot of F30/T50 (200 μl), one clot of F50/T50 (200 μl), one clot of F75/T75 (200 μl) and one clot of F75/T75 (40 μl). All clots were prepared from fresh components.

Samples preparation The samples were prepared just before the experiment. See section 8.1.1. For F75/T75 40 μl, the preparation is exactly the same as the 200 μl one except that 20 μl of F75 and 20 μl of T75 were mixed together in place of 100 μl each. In summary, the composition of the different fibrin samples tested

rheologically are listed in table 8.3.

Sample's name	**Fibrinogen (mg/ml)**	**Thrombin (U/ml)**
F12.5/T1 (200 μl, fresh)	12.5	1
F30/T50 (200 μl, fresh)	30	50
F50/T50 (200 μl, fresh)	50	50
F75/T75 (200 μl, fresh)	75	75
F75/T75 (40 μl, fresh)	75	75

Table 8.3: Composition of the five fibrin gels rheologically tested.

Rheometer See section 6.2.1. The gap's values used to trap those samples are respectively 0.6, 1.2, 1, 1.5 and 0.9 mm.

Protocol For F12.5/T1 (200 μl), F30/T50 (200 μl) and F75/T75 (200 μl), see table 8.4. For F50/T50 (200 μl), see table 8.5. For F75/T75 (40 μl), see table 8.6. As you can see, in table 8.5, a TS has been added between FS2 and AS3 in order to check the influence of the temperature on the fibrin hydrogel behavior.

	Strain, γ (%)	**Frequency, ω (rad/s)**	**# Pt./dec**
AS1:	$0.1 \rightarrow 4$	1	3
FS2:	0.4	$100 \rightarrow 0.1$	3
AS3:	$0.1 \rightleftarrows 100$	1	5
AS4:	$0.1 \rightleftarrows 100$	1	5
AS5:	$0.1 \rightleftarrows 100$	1	5
FS6:	0.4	$100 \rightarrow 0.1$	3
AS7:	$0.1 \rightleftarrows 100$	1	5

Table 8.4: Protocol followed for rheological analyzes on fibrin hydrogels F12.5/T1, F30/T50. All the tests were performed at 37°C.

	Strain, γ (%)	**Frequency, ω (rad/s)**	Temperature (°C)	**# Pt./dec**
AS1:	$0.1 \rightarrow 4$	1	37	3
FS2:	0.4	$100 \rightarrow 0.1$	37	3
TS:	0.4	1	$37 \rightarrow 25$	/
AS3:	$0.1 \rightleftarrows 100$	1	37	5
AS4:	$0.1 \rightleftarrows 100$	1	37	5
AS5:	$0.1 \rightleftarrows 100$	1	37	5
FS6:	0.4	$100 \rightarrow 0.1$	37	3
AS7:	$0.1 \rightleftarrows 100$	1	37	5

Table 8.5: Protocol followed for rheological analyzes on fibrin hydrogel F50/T50.

	Strain, γ (%)	**Frequency, ω (rad/s)**	**# Pt./dec**
AS1:	$0.1 \rightarrow 4$	1	3
FS2:	0.4	$100 \rightarrow 0.1$	3
AS3:	$0.1 \rightleftarrows 100$	1	5
AS4:	$0.1 \rightleftarrows 100$	1	5
AS5:	$0.1 \rightleftarrows 100$	1	5
FS6:	0.4	$100 \rightarrow 0.1$	3
AS7:	$0.1 \rightleftarrows 100$	1	5
AS8:	$0.1 \rightleftarrows 100$	1	10
AS9:	$0.1 \rightleftarrows 100$	5	10

Table 8.6: Protocol followed for rheological analyzes on fibrin hydrogel F75/T75 (200 μl). All the tests were performed at 37°C.

	Strain, γ (%)	**Frequency, ω (rad/s)**	**# Pt./dec**
AS1:	$0.1 \rightarrow 4$	1	4
FS2:	0.4	$100 \rightarrow 0.1$	4
AS3:	$0.1 \rightleftarrows 100$	1	10
AS4:	$0.1 \rightleftarrows 100$	1	10
AS5:	$0.1 \rightleftarrows 100$	1	10
FS6:	0.4	$100 \rightarrow 0.1$	4
AS7:	$0.1 \rightleftarrows 100$	1	10

Table 8.7: Protocol followed for rheological analyzes on fibrin hydrogels F75/T75 (40 μl). All the tests were performed at 37°C.

8.2.2 Results and discussion

Before starting the graph comparison, some comments have to be made concerning the rheological graphs. These six graphs obtained for F12.5/T1, F30/T50, F50/T50, F75/T75 Large and F75/T75 Small are available in Appendix B, Fig. 7, 8, 9, 10 and 11, respectively. Besides, a summary of the samples rheologically tested is available in Table 3, Appendix A.

First, as announced in section 5.2.4, a TS has been performed in order to check the influence of the temperature. As shown in Table 8.5, this test has only been done on F50/T50 from 37 to 25°C. The result of the experiment (Fig. 8.5) shows that the physical properties of fibrin hydrogels are not modified when varying the temperature in this range. Besides, the experiment has been stopped at 32°C, as no change was noticeable, and considering the time needed to perform this analysis.

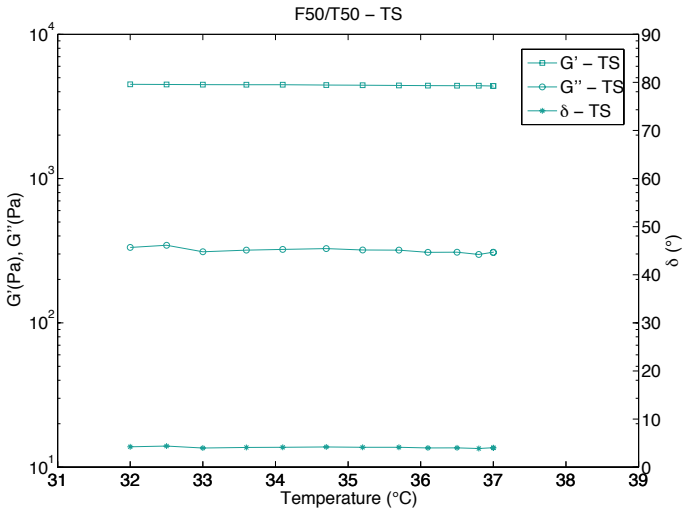

Figure 8.5: Temperature sweep at $\omega = 1$ rad/s, $\gamma = 0.4\%$ and from T= 37 °C to 32 °C, performed on F50/T50.

Secondly, as for bovine samples, unexpected ondulations are observed on fibrin rheological graphs. Indeed, for the four different fibrin formulations and all the AS, a decrease in G' SR along with a peak in G" SR are noticeable. These two phenomena being non physically possible and highly reproducible, supplementary tests have been performed in order to determine their origin. In this way, an AS[x2] has been applied on a F75/T75 Large sample with 10 Pt./dec instead of 5 (Table 8.6, AS8 and Fig. 8.6, in orange). This modification allowed to better follow the

G' and G" variations, but the same behavior was still observed. Therefore, a second AS[x2] has been applied of the same sample, still with 10 Pt./dec, but also with a frequency of 5 rad/s in place of 1 (Table 8.6, AS9 and Fig. 8.6, in green). This way, a smoother graph could be observed, meaning that the unexpected variations in G' and G" were due to empirical noice, alterating the true material response.

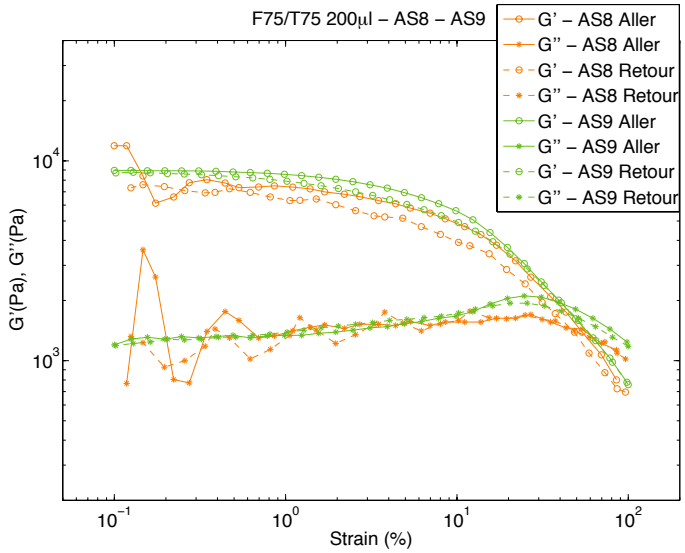

Figure 8.6: Amplitude sweeps applied on F75/T75 200 μl. AS8 (*Orange*) with ω = 1 rad/s superimposed with AS9 (*Green*) ω = 5 rad/s, both at T = 37 °C, 10 Pt./dec and with a strain going from 0.01 to 100% (solid lines) and from 100 to 0.01% (dotted lines). Circles stand for G' and stars for G".

This section will be divided in two parts regarding the graph comparison: (1) a comparison between the four fibrin formulations, and (2) a comparison between small and large F75/T75 fibrin hydrogels.

Comparison between different fibrin formulations

The storage plateau modulus (Fig. 8.7(a)) increases from F12.5/T1 to F75/T75. Indeed, the G' moduli stand around 140, 1100, 3800 and 9300 Pa for F12.5/T1, F30/T50, F50/T50 and F75/T75, respectively. This observation is consistent with this initial hypothesis, claiming that the stiffness of the matrix increases with fibrinogen concentration. Indeed, this phenomemon has been demonstrated in other studies, such as [54], but can also be observed while handling the different samples.

Moreover, except for F12.5/T1 that reorganizes itself even better as shear deformations are applied (AS7 > AS4 > AS3), the other three hydrogels seem to recover nearly completely their initial stiffness, which is, again, in agreement with the fibrin characteristics found in the litterature [30].

Considering the softness of F12.5/T1 hydrogel, the three other factors are non applicable to this gel formulation due to the flat shape of its rheological graphs and the rheometer which is not suitable to perform analyzes on such a soft tissue. Indeed, its storage plateau modulus approaches the detection threshold of the machine, ranging around 10^2 Pa. This gel formulation will not be taken into account for the other comparisons.

Regarding the yielding strain (Fig. 8.7(b)), a similar behavior can be noticed for F30/T50 and F75/T75, but higher yielding strain is observed for F30/T50, meaning that this formulation seems to better resist to the deformation. Moreover, both formulations show a noticeable difference between AS3/AS4/AS7 ratio, suggesting the loss of irreversible bonds inside the fibrin structure. The low values of F50/T50 suggests that the increase in fibrinogen concentration tends to decrease the ability of the fibrin to resist the deformation.It must be noted that this low yielding strain is not related to a larger stiffness of the sample as often observed. Furthermore, the intermediate behavior of F75/T75 could indicate that the increase of thrombin concentration has an inverse effect compared to the increase of fibrinogen concentration.

The general shape of the G'-G" crossover graph (Fig. 8.7(c)) is similar (Fig. 8.7(b)), with CO values being higher for F30/T50, than F75/T75 and finally F50/T50. Therefore, a similar observation can be established for the ability of the fibrin gel to resist to the deformation than for its ability to resist to the flowing.

Finally, the analysis of Fig. 9.2 allows to observe the growing of the hysteresis from left to right. Besides, for the three formulations, a high drop in hysteresis from AS3 to AS4 is observed, along with the slight hysteresis recovering from AS4 to AS7.

These observations suggest that many irreversible bonds have been broken during AS3 and that a better organization inside of the fibrin structure occured during AS7.

In conclusion, in addition to morphological differences, modifications in physical behaviors can also be observed when varying the fibrinogen/thrombin ratio. The major and most important characteristic, is the matrix rigidity, increasing with fibrinogen and thrombin concentrations. Regarding the other factors, a complementary study should be performed to distinct the specific impact of fibrinogen and thrombin concentrations variations. For example, similary rheological analyzes of a fibrin sample of F30/T75 or F50/T75 should be realized.

Comparison between small and large F75/T75

In order to check if the correction factor that should be established for human samples would be the same for other small samples, regardless of its nature, a small F75/T75 fibrin hydrogel has been analyzed and compared with the large one.

While looking at Fig. 8.8(a), the same observation can be made than for human samples, namely, the downard translation of the storage plateau modulus, but this time, of approximately a factor 10 instead of 3-4.

While the yielding strain and G'-G" crossover values did not seem to vary a lot between large and small human samples, this observation can not be made for fibrin. Indeed, in both graphs (Fig. 8.8(b) and 8.8(c)), the values of the small F75/T75 are way larger than the F75/T75 large ones.

Finally, the same relation is noticed for the hysteresis, namely, the decrease of the values of more or less a factor 100.

It is important to bear in mind that, compared to human samples, the fibrin hydrogels are very homogeneous, implying that those differences can not be due to matrix composition from one sample to another of the same fibrin formulation. Therefore, regarding the present results, no generalisation can be reached for the establishment of a common size correction factor. This problem is way more complex

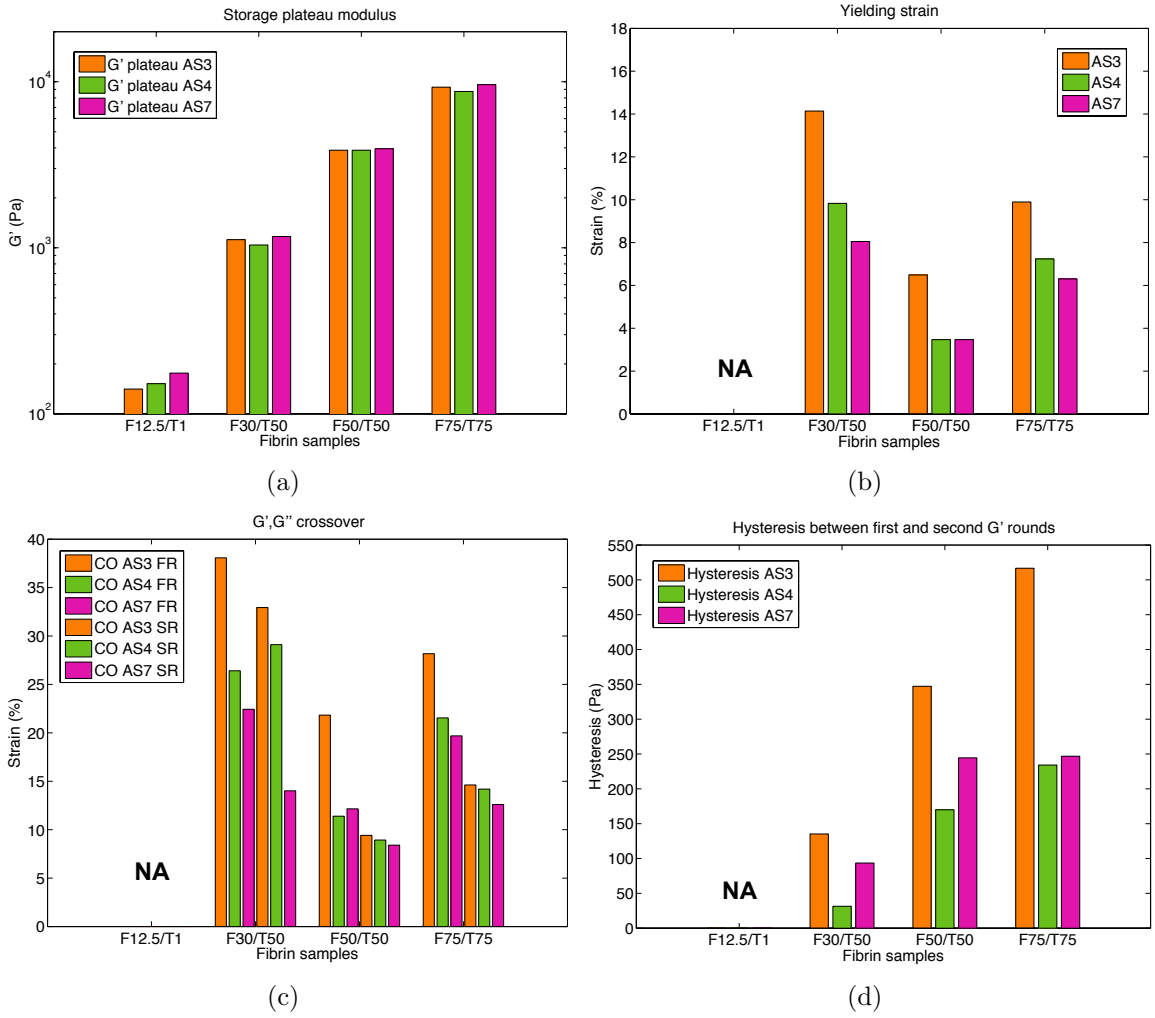

Figure 8.7: Comparison between large (200 μl) samples of fibrin gels of different concentrations, from smaller to higher: F12.5/T1, F30/T50, F50/T50, F75/T75. (a) Comparison of the storage plateau modulus of AS3 (Orange), AS4 (Green) and AS7 (Pink). (b) Comparison of the yielding strain of AS3 (Orange), AS4 (Green) and AS7 (Pink). (c) Comparison of the crossover between G' and G" of AS3 (Orange), AS4 (Green) and AS7 (Pink) at first round (FR) or at second round (SR). (d) Comparison between the hysteresis of AS3 (Orange), AS4 (Green) and AS7 (Pink). NA = Non applicable.

than planned and further investigations need to be perform to establish such a coefficient.

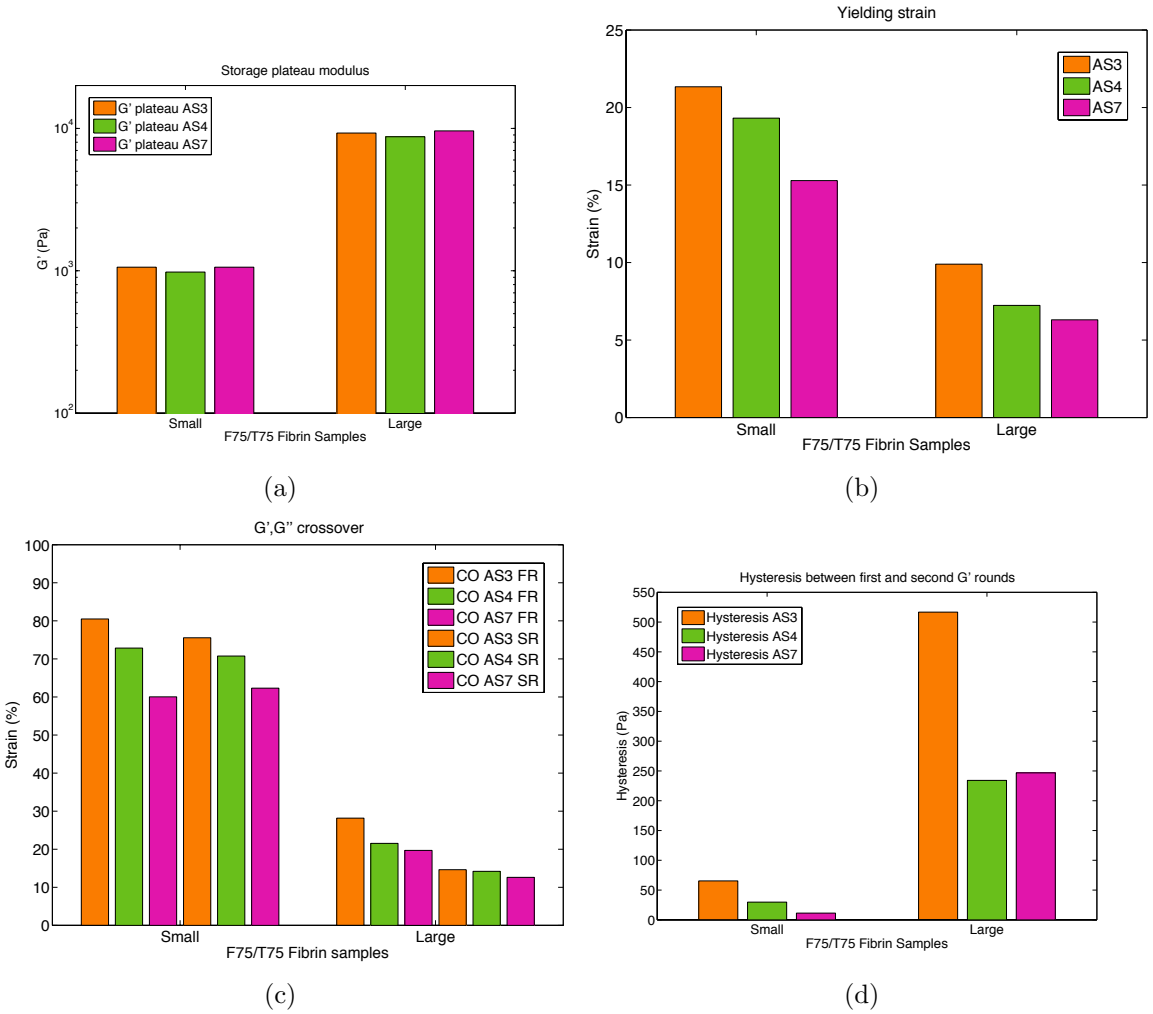

Figure 8.8: Comparison between large (200 μl) and small (40 μl) samples of F75/T75 fibrin gels. (a) Comparison of the storage plateau modulus of AS3 (Orange), AS4 (Green) and AS7 (Pink). (b) Comparison of the yielding strain of AS3 (Orange), AS4 (Green) and AS7 (Pink). (c) Comparison of the cross-over between G' and G" of AS3 (Orange), AS4 (Green) and AS7 (Pink) at first round (FR) or at second round (SR). (d) Comparison between the hysteresis of AS3 (Orange), AS4 (Green) and AS7 (Pink).

Chapter 9

Comparison between human ovarian tissue and fibrin gels

The main goal of this study was to find the most appropriate matrix to achieve the TAO scaffold. In order to do so, a comparison between, first morphological and then, physical properties of both fibrin hydrogels and human ovarian samples from young patients has been performed, and is presented in this section. Besides, as the fibrin formulation F12.5/T1 has shown poor results with human follicles encapsulation followed by mouse transplantation, this matrix will not be compared to human ovarian tissue in the following.

As no major morphological variability has been detected from one patient to another in section 7, one of the four human samples has been arbitrarily chosen for the morphological comparison between human and fibrin matrices.

Several differences can be observed while analyzing Fig. 9.1. On one hand, the human matrix is compact and heterogeneous and, on the other hand, fibrin hydrogels are porous and highly homogeneous.

Regarding the fiber diameter, the F50/T50 formulation is the one that mimics at best the human matrix, with a mean diameter of 65 nm compared to 68 nm. Moreover, although higher fibrin concentrations, such as F50/T50 or F75/T75, showed low fiber diameter, some thicker fibers were also observable, at a lesser extend, mimicing event better the human matrix.

Considering the heterogeneity of the human ovarian matrix, an interesting strategy could be to add other components to the F50/T50 fibrin scaffold. This would allow to build a less homogeneous matrix, reduce the porosity and consequently, make it more dense. Besides, as human matrix, fibrin hydrogels have different pore sizes inside of a single scaffold.

In summary, regarding the morphological properties of the different matrices, F50/T50 appears to be the more suitable fibrin formulation to mimic the human ovarian cortex.

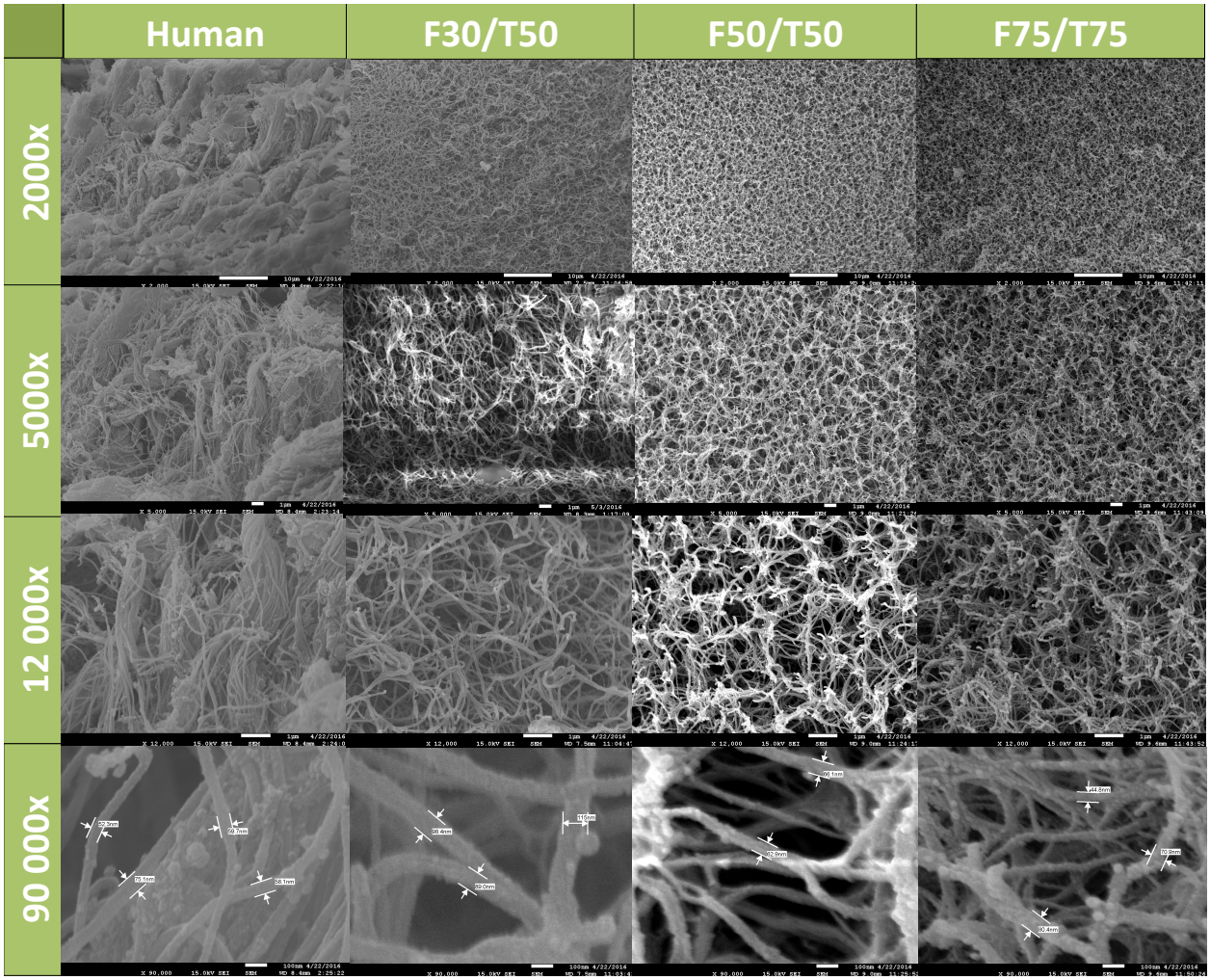

Figure 9.1: Comparison between SEM pictures of fibrin hydrogels of three different concentrations (F30/T50, F50/T50, F75/T75) and a sample of human ovarian cortex from a young patient (columns) at four different magnifications (rows).

The comparison between the morphological properties being more a qualitative approach, a quantitative study needs to be performed. Fig. 9.2 compares the rheological results presented beforehand for three fibrin formulations (F30/T50, F50/T50 and F75/T75) and for the human sample from a young patient (Human LY).

The most important factor for follicular survival and development is the matrix stiffness (Fig. 9.2(a)). Based on the rigidity of the different samples for each AS (Table 9.1), the F30/T50 fibrin formulation seems to be the more appropriate matrix, in order to mimic the human ovarian cortex. The storage plateau moduli of F12.5/T1 have been added to this table to emphasize the explanation proposed by Amorim C.A. to justify the bad results obtained with encapsulated human follicles. Indeed, the stiffness of this matrix is largely lower (more a less a factor 10) than the human cortical one. This suggests than the mouse follicles need a softer matrix than human ones to survive and develop.

G' plateau	**F12.5/T1**	**F30/T50**	**F50/T50**	**F75/T75**	**Human LY**
AS3 [Pa]	140	1120	3870	9280	1210
AS4 [Pa]	150	1040	3870	8740	1220
AS7 [Pa]	176	1170	3950	9610	1250

Table 9.1: Summary of the storage plateau moduli (in Pa) of the four different fibrin hydrogels and a human ovarian sample from a young patient (Human LY).

While comparing yielding strain values (Fig. 9.2(b)), the behavior of Human LY seems to be, once more, more like F30/T50 but, with a lower AS3/AS4/AS7 ratio, suggesting that the human ovarian matrix recovers better its initial ability to resist the deformation.

The comparison of G'-G" crossover values happens to be more complex (Fig. 9.2(c)). Human LY crossover values appear to stand between the F30/T50 and F75/T75 ones. But compared to these artificial matrices, the human one seems, to have a better recovery of its initial physical properties, according to the constancy of the G'-G" crossover values of AS3, AS4, AS7.

Finally, the last graph (Fig. 9.2(d)) leads to the same conclusion at the first one: the hysteresis amplitudes of Human LY look more like the F30/T50 ones. However, while the human matrix seems to be composed essentially of reversible bonds and to reorganize better when submitted to shear deformations, the F30/T50 hydrogel seems to be made of both irreversible and reversible links and to be more affected by shear deformations.

In conclusion, in order to better mimic the physical behaviors of the human cortical ECM, the F30/T50 formulation should be chosen. However, if this matrix is more similar to the human one, at least regarding the physical properties, some improvements should be done to remove the dissimilarities. In particular, the composition of the formulation should be modified to allow a better recovery of the initial state after a large deformation.

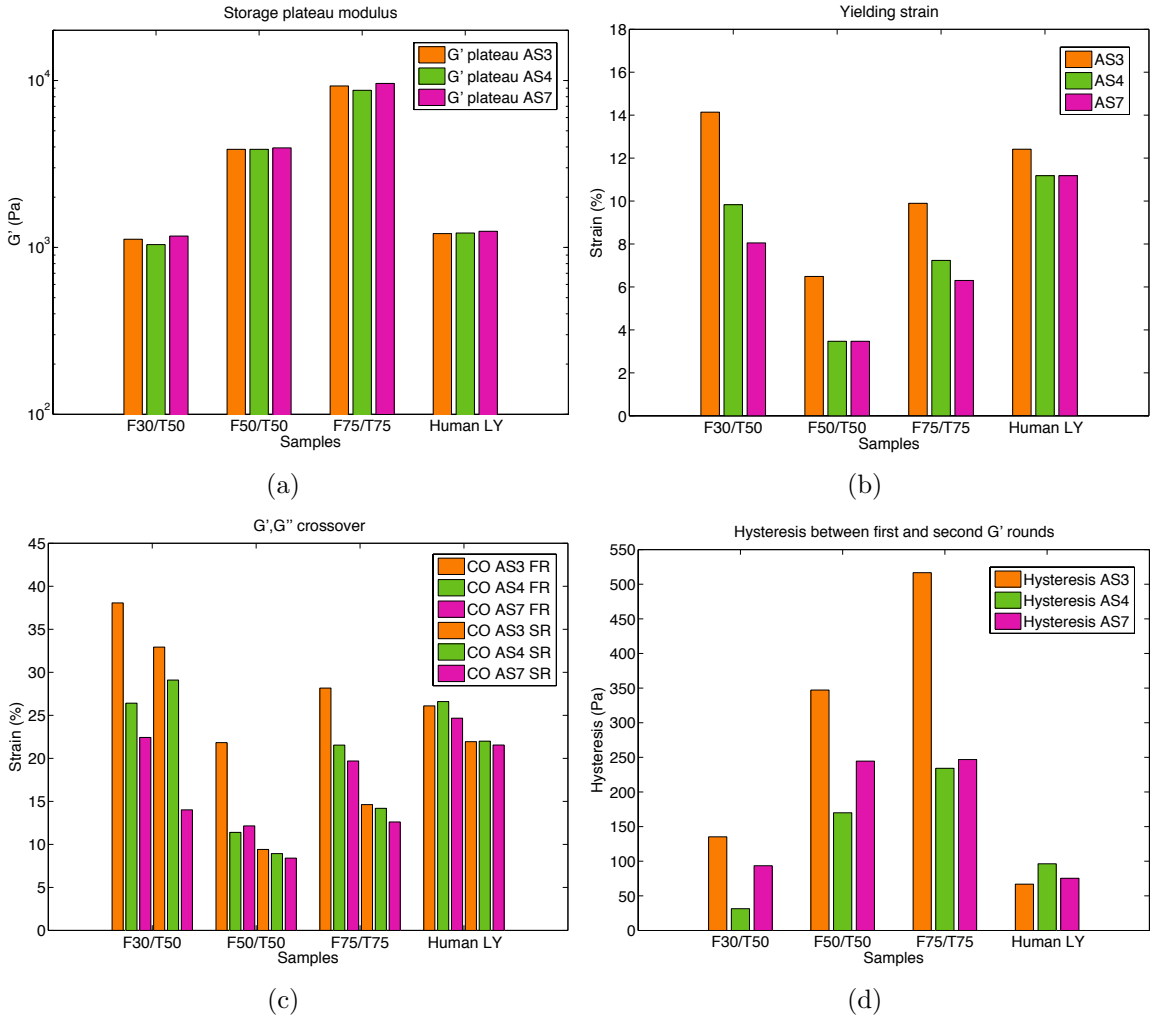

Figure 9.2: Comparison between large (200 μm) samples of fibrin gels of different concentrations (F30/T50, F50/T50, F75/T75) and a large sample of human ovarian cortex from a young patient (Human LY). (a) Comparison of the storage plateau modulus of AS3 (Orange), AS4 (Green) and AS7 (Pink). (b) Comparison of the yielding strain of AS3 (Orange), AS4 (Green) and AS7 (Pink). (c) Comparison of the cross-over between G' and G" of AS3 (Orange), AS4 (Green) and AS7 (Pink) at first round (FR) or at second round (SR). (d) Comparison between the hysteresis of AS3 (Orange), AS4 (Green) and AS7 (Pink).

Chapter 10

Conclusions and perspectives

Due to the risk of reimplanting malignant cells with the cryopreservation and transplantation of ovarian tissue technique, the transplantable artificial ovary is being developed. The purpose of the present study was to assess the morphological and physical properties of the human ovarian cortex. To this end, scanning electron microscopy along with rheology have been performed on samples of different nature.

First, bovine ovarian fragments have been tested for several reasons: to check the feasibility of rheological analyzes on such soft and inhomogeneous tissues, to address the size problem and the limited resources of human samples, and to compare some fresh and frozen-thawed ovarian specimens. Indeed, human samples being difficult to obtain, the analyzes could only be performed on frozen-thawed human ovarian fragments due to the impossibility to plan the biopsies collection.

Both SEM and rheological experiments showed consistent results, being in aggreement with informations found in the litterature. Once the feasibility proved, the second goal of the analyzes was to check if any morphological and/or physical modifications appear between the fresh and frozen-thawed samples. Four samples were analyzed by SEM, two fresh and two frozen-thawed. Some dissimilarities were noticed between the two frozen-thawed samples, avoiding to conclude whether the cryopreservation process has an impact on the morphological properties or not.

The same conclusion was made for physical properties. Indeed, two bovine ovarian samples, one fresh and one frozen-thawed, were rheologically tested. Differ-

ences between physical behaviors of these two fragments were observed, but there was no sufficient proof to define their origin. Indeed, they could be due to matrix heterogeneity, variability between animals or cryopreservation and thawing processes.

To highlight the origin of these dissimilarities, both morphological and physical, more samples should be tested. Moreover, the compared fresh and frozen fragments should arise from the same ovary, to avoid the risk of variability from one animal to another one.

Based on these conclusions on bovine fragments, analyzes on human ones have been performed, keeping in mind the possible existence of a difference between fresh and frozen-thawed specimens.

Considering the fact that collection of large human ovarian biopsies from young patients is complicated, and that the rheometer needs samples of minimum 8×8 mm^2, one of the goal of this study was to define a correction factor to take into account in order to compensate the small size of the samples. This last one could be applied on the rheological results of small specimens, in order to obtain with their real physical properties. To this end, a comparison between rheological data of a small and a large samples from the same patient has been analyzed. Beside this test, the same experiment has been performed for a small and a large fibrin clots made of fibrinogen 75 mg/ml and thrombin 75 U/ml, in order to check if a same correction coefficient could be applied to small samples, regardless of their nature. The conclusion of these two experiments is that the establishment of such a factor appears to be more complex than estimated. Therefore, more analyzes should be realized along with a higher number of samples.

Nevertheless, the impossibility to determine this coefficient has not prevented the determination of the physical properties of young human samples. Indeed, against all odds, a large ovarian fragment from a young patient has been provided. As for bovine fragments, the samples were tested both by SEM and rheology. For SEM, four samples of different young patients were analyzed, in order to assess if there were high morphological differences from the ovarian cortex of one patient to another. The SEM results allowed to conclude that no such dissimilarities were ob-

served. Regarding the rheological analyzes, a fragment from a menopaused patient was compared with one of a young patient. Contrary to the initial hypothesis, no major difference in rigidity was noticed. Nevertheless, some dissimilarities appear regarding other physical characteristics of the matrices and in particular, the ability of the sample to recover its initial state after a deformation. But more samples should be analyzed to highlight their origin. Indeed, as for bovine fragments, those differences could come from the high heterogeneity of the matrix or from the variability from one female patient to another.

Finally, four fibrin formulations were tested and compared to the young human ovarian cortex. Indeed, the major goal of this study was to assess the physical aspects of the human ovary and afterward, to find the best fibrin formulation for the TAO scaffold.

According to morphological properties, the fibrin hydrogel containing 50 mg/ml of fibrinogen and 50 U/ml of thrombin seemed to be the more appropriate. However, this SEM analysis being more qualitative, a comparison between the physical properties has been achieved, by rheology. The rheological results suggested that the more suited fibrin formulation is the one made of 30 mg/ml of fibrinogen and 50 U/ml of thrombin.

Nevertheless, this last one should be improved in order to fit with all the physical behaviors of the human cortical ECM. To this end, the thrombin concentration could be increased a little, in order to slightly rise the matrix stiffness and slightly reduce the matrix porosity, making it morphologically more like F50/T50. Besides, other components could be added to fibrin, in order to add many reversible bonds and, therefore, increase its ability to resist shear deformations and flowing, such as the human cortex. As examples, engineered adhesion and growth factors could be added [28], or fibronectine, as the protein is present in the human ovarian cortex and is able to bind to fibrin [55].

In order to better compare the hysteresis of different samples, a normalization of the hystereses could be performed, giving a better idea of the real difference in reversibility from one sample to another.

Other techniques could be used to analyze human ovarian cortex and fibrin scaffolds. Regarding the structure, 3D and trans-sectional micro-computed tomography could be used on fresh samples, avoiding the effects of the SEM preparation protocol, such as the risk of shrinkage or salt cristals introduction [35]. Furthermore, Cirka H.A et al. developed an eccentric rheometer for viscoelastic characterization of small, anisotropic, soft and irregularly shaped gels and tissue biospies [56]. This technique includes specific experimental settings, allowing to finally apply a correction factor to the results in order to offset the size difference. First, tests on known samples should be realized on this rheometer, which is easily implemented from a standard rotational rheometer. Once the working principle and settings of this new instrument controlled, human and fibrin specimens should also be tested for statistical studies.

Bibliography

[1] C. A. Amorim and A. Shikanov, "The artificial ovary: current status and future perspectives," *Future Oncology*, 2016. In press.

[2] F. Paulini, M. J. Vilela, C. C. Maria, J. Donnez, P. Jadoul, M.-M. Dolmans, and C. A. Amorim, "Survival and growth of human preantral follicles after cryopreservation of ovarian tissue, follicle isolation and short-term xenografting," *Reproductive biomedicine online*, 2016. In press.

[3] J. Donnez and S. S. KIM, "Contributions of ovarian stromal cells to follicle culture," in *Principles and Practice of Fertility Preservation*, ch. 34, pp. 409–420, Cambridge: Cambridge University Press, 1 ed., 2011.

[4] J. Donnez, M.-M. Dolmans, C. Diaz, and A. Pellicer, "Ovarian cortex transplantation: time to move on from experimental studies to open clinical application," *Fertility and Sterility*, vol. 104, no. 5, pp. 1097–1098, 2015.

[5] J. Donnez and M.-M. Dolmans, "Fertility preservation in women," *Nature reviews. Endocrinology*, vol. 9, pp. 1–15, dec 2013.

[6] N. C. Institute, "Seer stat fact sheets: Ovary cancer." Bethesda, MD, http://seer.cancer.gov/statfacts/html/ovary.html. Online resource.

[7] M. M. Laronda, A. E. Jakus, K. a. Whelan, J. a. Wertheim, R. N. Shah, and T. K. Woodruff, "Initiation of puberty in mice following decellularized ovary transplant," *Biomaterials*, vol. 50, pp. 20–29, may 2015.

[8] S. Sivanandane, M. S. Justin, and J. Sunyoung, "Engineered multilayer ovarian tissue that secretes sex steroids and peptide hormones in response to gonadotropins," *Biomaterials*, vol. 34, no. 10, pp. 2412–2420, 2013.

[9] V. Luyckx, *Fertility preservation in cancer patients : from cryopreserved ovarian tissue to isolated follicles.* PhD thesis, Université Catholique de Louvain, 2014.

[10] I. Maystadt, "La rencontre du spermatozoïde et de l'ovocyte," in *Reproduction Humaine et Développement Embryonnaire Précoce*, ch. 1, pp. 1–13, 2016. Université de Namur. University class.

[11] C. Nicaise, "Le système génital femelle," in *Histologie moléculaire et fonctionnelle humaine*, ch. 10, pp. 3–14, 2016. Université de Namur. University class.

[12] A. N., "Histo lab final," 2013. https://www.studyblue.com/notes/note/n/histo-lab-final/deck/6199790. Online resource.

[13] R. J. Rodgers and H. F. Irving-Rodgers, "Morphological classification of bovine ovarian follicles," *Reproduction*, vol. 139, no. 2, pp. 309–318, 2010.

[14] R. J. Rodgers, H. F. Irving-Rodgers, and D. L. Russel, "Extracellular matrix of the developing ovarian follicle," *Reproduction*, vol. 126, pp. 415–424, 2003.

[15] W. H. B. Wallace and T. W. Kelsey, "Human ovarian reserve from conception to the menopause," *PLoS ONE*, vol. 5, no. 1, pp. 1–9, 2010. e8772.

[16] B. M. Koeppen and B. A. Stanten, "The Male and Female Reproductive Systems," in *Berne & Levy Physiology* (M. Elsevier, ed.), ch. 43, pp. 758–798, sixth edit ed., 2010.

[17] T. K. Woodruff and L. D. Shea, "A new hypothesis regarding ovarian follicle development: Ovarian rigidity as a regulator of selection and health," *Journal of Assisted Reproduction and Genetics*, vol. 28, no. 1, pp. 3–6, 2011.

[18] V. Luyckx, M.-M. Dolmans, J. Vanacker, C. Legat, C. Fortuño Moya, J. Donnez, and C. A. Amorim, "A new step toward the artificial ovary: survival and

proliferation of isolated murine follicles after autologous transplantation in a fibrin scaffold.," *Fertility and Sterility*, vol. 101, pp. 1149–1156, apr 2014.

[19] M. M. Dolmans, V. Luyckx, J. Donnez, C. Y. Andersen, and T. Greve, "Risk of transferring malignant cells with transplanted frozen-thawed ovarian tissue," *Fertility and Sterility*, vol. 99, no. 6, pp. 1514–1522, 2013.

[20] J. Vanacker, V. Luyckx, M. M. Dolmans, A. Des Rieux, J. Jaeger, A. Van Langendonckt, J. Donnez, and C. a. Amorim, "Transplantation of an alginate-matrigel matrix containing isolated ovarian cells: First step in developing a biodegradable scaffold to transplant isolated preantral follicles and ovarian cells," *Biomaterials*, vol. 33, no. 26, pp. 6079–6085, 2012.

[21] C. A. Amorim, "Artificial ovary," in *Gonadal Tissue Cryopreservation in Fertility* (N. Suzuki and J. Donnez, eds.), ch. 14, New York, USA: Springer, 2016.

[22] J. Donnez and S. S. KIM, "Artificial ovary," in *Principles and Practice of Fertility Preservation*, ch. 38, pp. 448–458, Cambridge: Cambridge University Press, 1 ed., 2011.

[23] M. M. Dolmans, N. Michaux, A. Camboni, B. Martinez-Madrid, A. Van Langendonckt, S. A. Nottola, and J. Donnez, "Evaluation of Liberase, a purified enzyme blend, for the isolation of human primordial and primary ovarian follicles," *Human Reproduction*, vol. 21, no. 2, pp. 413–420, 2006.

[24] M. M. Dolmans, B. Martinez-Madrid, E. Gadisseux, Y. Guiot, W. Y. Yuan, A. Torre, A. Camboni, A. Van Langendonckt, and J. Donnez, "Short-term transplantation of isolated human ovarian follicles and cortical tissue into nude mice," *Reproduction*, vol. 134, no. 2, pp. 253–262, 2007.

[25] K. Y. Lee and D. J. Mooney, "Alginate: Properties and biomedical applications," *Progress in Polymer Science (Oxford)*, vol. 37, no. 1, pp. 106–126, 2012.

[26] M. Chiti, M. Dolmans, R. Orellana, M. Soares, F. Paulini, J. Donnez, and C. Amorim, "Influence of follicle stage on artificial ovary outcome using fibrin as a matrix," *Human Reproduction*, vol. 31, no. 2, pp. 427–435, 2016.

[27] V. Luyckx, M. M. Dolmans, J. Vanacker, S. R. Scalercio, J. Donnez, and C. a. Amorim, "First step in developing a 3D biodegradable fibrin scaffold for an artificial ovary," *Journal of Ovarian Research*, vol. 6, no. 1, pp. 1–10, 2013.

[28] a. Alovskaya, T. Alekseeva, J. B. Phillips, V. King, and R. Brown, "Fibronectin, Collagen, Fibrin-Components of Extracellular Matrix for Nerve regeneration," *Topics in Tissue Engineering*, vol. 3, pp. 1–27, 2007.

[29] C. Yeromonahos, *Nanostructure des fibres de fibrine*. PhD thesis, Université de Grenoble, 2011.

[30] P. A. Janmey, J. P. Winer, and J. W. Weisel, "Fibrin gels and their clinical and bioengineering applications.," *Journal of the Royal Society, Interface*, vol. 6, no. 30, pp. 1–10, 2009.

[31] E. a. Ryan, L. F. Mockros, J. W. Weisel, and L. Lorand, "Structural Origins of Fibrin Clot Rheology," *Biophysical Journal*, vol. 77, no. 5, pp. 2813–2826, 1999.

[32] J. W. Weisel, "The mechanical properties of fibrin for basic scientists and clinicians," *Biophysical Chemistry*, vol. 112, no. 2-3, pp. 267–276, 2004.

[33] J.-P. Collet, H. Shuman, R. E. Ledger, S. Lee, and J. W. Weisel, "The elasticity of an individual fibrin fiber in a clot," *Proceedings of the National Academy of Sciences of the United States of America*, vol. 102, no. 26, pp. 9133–9137, 2005.

[34] S. Münster, L. M. Jawerth, B. a. Leslie, J. I. Weitz, B. Fabry, and D. a. Weitz, "Strain history dependence of the nonlinear stress response of fibrin and collagen networks," *Proceedings of the National Academy of Sciences of the United States of America*, vol. 110, no. 30, pp. 12197–12202, 2013.

[35] B. S. Kim, H. M. Sung, H. K. You, and J. Lee, "Effects of fibrinogen concentration on fibrin glue and bone powder scaffolds in bone regeneration," *Journal of Bioscience and Bioengineering*, vol. 118, no. 4, pp. 469–475, 2014.

[36] Baxter, "Tissucol kit notices," 2012. http://www.baxter.fr/04/produits/ressources/Tissucol-Notices.pdf. Online resource.

[37] S. Demoustier, G. Leloup, and C. Dupont, *MAPR2030 - Biomaterials*. 2014. Université Catholique de Louvain. University class.

[38] L. Germain, *Influence de la concentration en fibrinogène et en thrombine des hydrogels de fibrine sur la survie et la prolifération de cellules souches dentaires*. Master thesis, Université Catholique de Louvain, 2013.

[39] R. F. Egerton, *Physical Principles of Electron Microscopy : An Introduction to TEM, SEM and AEM*. No. 1, New York, USA: Springer, 2005.

[40] C. Roy, "Utilisation de bactériophages comme "templates" pour la synthèse guidée de nanofils de polymère conjugué," Master's thesis, Université Catholique de Louvain, 2007.

[41] J. Atteberry, "How scanning electron microscopes work," 2009. http://science.howstuffworks.com/scanning-electron-microscope.htm. Online resource.

[42] A. Agrawal, A. Aliyan, J. J. Allen, and A. R. Barron, *Physical Methods in Chemistry and Nano Science*. 2014.

[43] Quorum Technologies, "Sputter Coating Technical Brief," Tech. Rep. 2, Kent, 2002.

[44] J.-F. Stoltz, "Sang : Écoulement." http://www.universalis.fr/encyclopedie/sang-ecoulement/. Online resource.

[45] Q. Voleppe, *Rheology of supramolecular systems based on linear poly(ethylene oxide) and metal-ligand interactions : experiments and modeling*. Master thesis, Université Catholique de Louvain, 2011.

[46] E. van Ruymbeke, *Relationship between linear viscoelastic properties and molecular structure for linear and branched polymers*. PhD thesis, Université Catholique de Louvain, 2005.

[47] A. Jonas, S. Demoustier, and E. van Ruymbeke, *MAPR2019 - Polymer Science and Engineering*. 2015. Université Catholique de Louvain. University class.

[48] C. A. Amorim, A. Van Langendonckt, A. David, M. M. Dolmans, and J. Donnez, "Survival of human pre-antral follicles after cryopreservation of ovarian tissue, follicular isolation and in vitro culture in a calcium alginate matrix," *Human Reproduction*, vol. 24, no. 1, pp. 92–99, 2009.

[49] Cressington, "Cressington 208HR: High Resolution Sputter Coater." http://cressington.com/spec_208hr.html. Online resource.

[50] JEOL, "JSM-7600F Schottky Field Emission Scanning Electron Microscope." http://www.jeol.co.jp/en/products/detail/JSM-7600F.html. Online resource.

[51] C. D. Wood, M. Vijayvergia, F. H. Miller, T. Carroll, C. Fasanati, L. D. Shea, L. Catherine Brinson, and T. K. Woodruff, "Multi-modal magnetic resonance elastography for noninvasive assessment of ovarian tissue rigidity in vivo," *Acta Biomaterialia*, vol. 13, pp. 295–300, 2015.

[52] K. E. Kadler, D. F. Holmes, J. A. Trotter, and J. A. Chapman, "Collagen fibril formation," *Journal of Biochemistry*, vol. 316, no. 1, pp. 1–11, 1996.

[53] C. Ricciardelli and R. J. Rodgers, "Extracellular matrix of ovarian tumors," *Seminars in Reproductive Medicine*, vol. 24, no. 4, pp. 270–282, 2006.

[54] L. Germain, P. De Berdt, J. Vanacker, J. Leprince, A. Diogenes, D. Jacobs, G. Vandermeulen, C. Bouzin, V. Préat, C. Dupont-Gillain, and A. des Rieux, "Fibrin hydrogels to deliver dental stem cells of the apical papilla for regenerative medicine," *Regenerative Medicine*, vol. 10, no. 2, pp. 153–167, 2015.

[55] M. Hada, M. Kaminski, P. Bockenstedt, and J. Mcdonagh, "Covalent Crosslinking of von Willebrand Factor to Fibrin," *Blood*, vol. 68, no. 1, pp. 95–101, 1986.

[56] H. A. Cirka, S. A. Koehler, W. W. Farr, and K. L. Billiar, "Eccentric rheometry for viscoelastic characterization of small, soft, anisotropic, and irregularly shaped biopolymer gels and tissue biopsies," *National Institutes of Health*, vol. 40, no. 8, pp. 1654–1665, 2012.

[57] E. Telfer, C. Torrance, T. Place, and E. E. H. Ag, "Morphological study of cultured preantral ovarian follicles of mice after transplantation under the kidney capsule," *J. Reprod. Fert.*, vol. 89, pp. 565–571, 1990.

[58] R. Gosden, "Restitution of fertility in sterilized mice by transferring primordial ovarian follicles," *Human Reproduction*, vol. 5, no. 5, pp. 499–504, 1990.

[59] J. Carroll and R. G. Gosden, "Transplantation of frozen-thawed mouse primordial ovarian follicles," *Human Reproduction*, vol. 8, no. 8, pp. 1163–1167, 1993.

[60] M.-M. Dolmans, W. Y. Yuan, A. Camboni, A. Torre, A. Van Langendonckt, B. Martinez-Madrid, and J. Donnez, "Development of antral follicles after xenografting of isolated small human preantral follicles.," *Reproductive biomedicine online*, vol. 16, no. 5, pp. 705–711, 2008.

[61] A. Viswanath, L. Germain, and K. Shakesheff, "Hydrogel derived from decellularized bovine ovarian extracellular matrix," 2015. Presented at the 4th TERMIS World Congress, September 8, 2015, Boston, MA, USA.

[62] J. Vanacker, M.-M. Dolmans, V. Luyckx, J. Donnez, and C. a. Amorim, "First transplantation of isolated murine follicles in alginate," *Regenerative Medicine*, vol. 9, pp. 609–619, sep 2014.

[63] R. M. Smith, A. Shikanov, E. Kniazeva, D. Ramadurai, T. K. Woodruff, and L. D. Shea, "Fibrin-Mediated Delivery of an Ovarian Follicle Pool in a Mouse Model of Infertility," *Tissue engineering. Part A*, vol. 20, no. 21-22, pp. 3021–3030, 2014.

[64] A. R. Rajabzadeh, H. Eimani, H. M. Koochesfahani, A. H. Shahvardi, and R. Fathi, "Morphological study of isolated ovarian preantral follicles using fibrin gel plus platelet lysate after subcutaneous transplantation," *Cell Journal*, vol. 17, no. 1, pp. 145–152, 2015.

[65] E. Kniazeva, A. N. Hardy, S. A. Boukaidi, T. K. Woodruff, J. S. Jeruss, and L. D. Shea, "Primordial Follicle Transplantation within Designer Biomaterial

Grafts Produce Live Births in a Mouse Infertility Model," *Scientific Reports*, vol. 5, no. 17709, pp. 1–11, 2015.

[66] J. Kim, A. Perez, and O. Nelson, "Engineering artificial ovarian tissue using multi-arm poly(ethylene glycol) hydrogel," *Tissue engineering*, vol. 21, no. 1, p. 29, 2015.

Appendix A: Supplementary informations

Matrix	Species	Follicles	Grafting	Main results
Collagen [57]	Mouse to mouse	Preantral	10 days	Embryos
Plasma clot [58]	Mouse to mouse	Primordial	4-12 weeks	Offspring
Plasma clot [59]	Mouse to mouse	Primordial	6-12 weeks	Offspring
Plasma clot [24]	Human to mouse	Preantral	7 days	Secondary follicles
Plasma clot [60]	Human to mouse	Preantral	5 months	Antral follicles
Bovine DOM [7]	Mouse to mouse	Primary	2-4 weeks	Puberty
Human DOM [7]	Mouse to mouse	Primary	2-4 weeks	Puberty
Bovine DOM [61]	Mouse to mouse	Primary	10 days	Viable follicles
Alginate [62]	Mouse to mouse	Preantral	1 week	Antral follicles
Fibrin [18] (F12.5/T1; F25/T4)	Mouse to mouse	Preantral	1 week	Antral follicles
Fibrin (F12.5/T1) [26]	Mouse to mouse	Preantral	1 week	Antral follicles
Fibrin (F40/T50) [63]	Mouse to mouse	Preantral	3 weeks	Antral follicles
Fibrin [64]	Mouse to mouse	Preantral	2 weeks	Antral follicles
Fibrin (F40/T50) [65]	Mouse to mouse	Preantral	$>$ 9 days	Offspring
Fibrin (F50/T10) [2]	Human to mouse	Preantral	1 week	Follicle growth
PEG [66]	Mouse to mouse	Pirmordial	30 days	Antral follicles

Table 1: Studies on transplantation of isolated ovarian follicles in different matrices (lines). The columns correspond to the type of matrix, the species (the origin of the follicles and the graft host), the stage of the isolated and transplanted follicles, the grafting time and the main results of the study, respectively. Table adapted from [1].

Sample's name	**Nature**	**Source**	**State**	**Age**
Fresh B1	Bovine cortex	Cow 1	Fresh	Young
Fresh B2	Bovine cortex	Cow 2	Fresh	Young
Frozen B3	Bovine cortex	Cow 3	Frozen-thawed	Young
Frozen B4	Bovine cortex	Cow 4	Frozen-thawed	Young
H4538	Human cortex	Patient 1	Frozen-thawed	Young
H4544	Human cortex	Patient 2	Frozen-thawed	Young
H4548	Human cortex	Patient 3	Frozen-thawed	Young
H4565	Human cortex	Patient 4	Frozen-thawed	Young
F12.5/T1	Fibrin	Tissucol kit	Fresh	/
F30/T50	Fibrin	Tissucol kit	Fresh	/
F50/T50	Fibrin	Tissucol kit	Fresh	/
F75/T75	Fibrin	Tissucol kit	Fresh	/

Table 2: Summary of the samples analyzed by SEM. All samples were small, to allow the osmium penetration and their introduction inside the SEM.

Sample's name	**Nature**	**Source**	**State**	**Age**	**Size**
Fresh B1	Bovine cortex	Cow 1	Fresh	Young	Large
Fresh B2	Bovine cortex	Cow 2	Fresh	Young	Large
Frozen B4	Bovine cortex	Cow 4	Frozen-thawed	Young	Large
Human SM	Human cortex	Patient 5	Frozen-thawed	Menopaused	Small
Human LM	Human cortex	Patient 5	Frozen-thawed	Menopaused	Large
Human SM	Human cortex	Patient 6	Frozen-thawed	Young	Large
F12.5/T1	Fibrin	Tissucol kit	Fresh	/	200 μl
F30/T50	Fibrin	Tissucol kit	Fresh	/	200 μl
F50/T50	Fibrin	Tissucol kit	Fresh	/	200 μl
F75/T75 Large	Fibrin	Tissucol kit	Fresh	/	200 μl
F75/T75 Small	Fibrin	Tissucol kit	Fresh	/	40 μl

Table 3: Summary of the samples used for rheological analyzes.

Appendix B: Rheological results

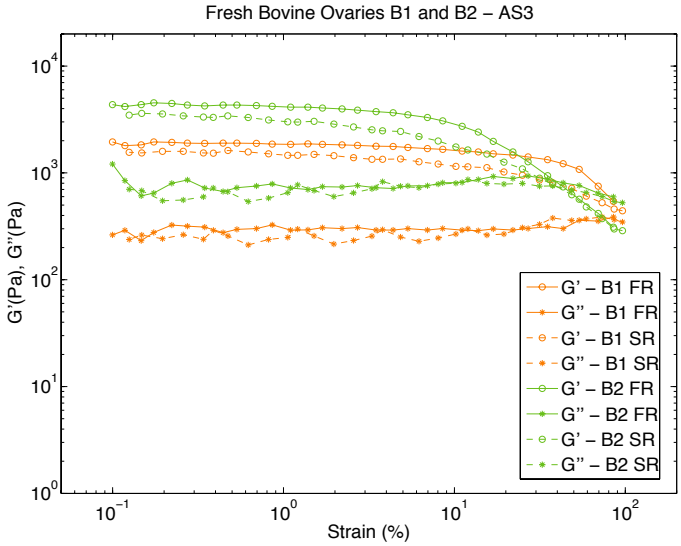

Figure 1: Comparison of AS3 between two fresh bovine ovarian fragments, Fresh B1 and Fresh B2. These AS were performed at T = 37 °C, $\omega = 1$ rad/s and with a strain going from 0.01 to 100% (solid lines) and from 100 to 0.01% (dotted lines). Circles stand for G' and stars for G".

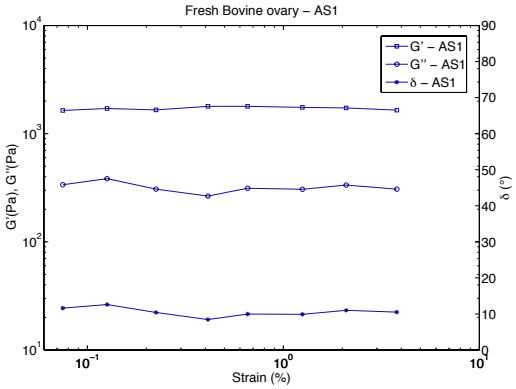

(a) Amplitude sweep at T =37 °C, $\omega = 1$ rad/s and with a strain going from 0.075 to 3.8%.

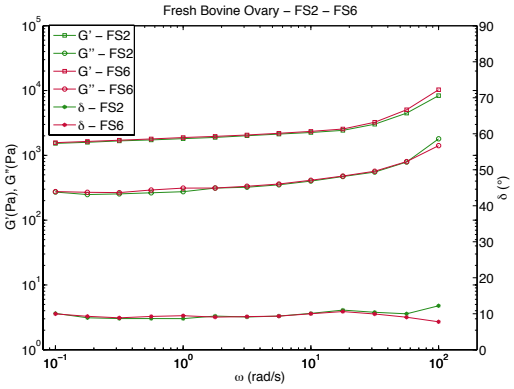

(b) Frequency sweeps, FS2 (*Green*) and FS6 (*Red*) at T = 37 °C, $\gamma = 0.4\%$ and ω = 100-0.1 rad/s. Squares stand for G', circles for G" and stars for δ.

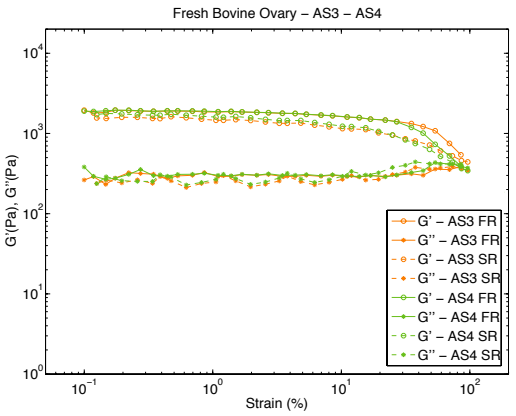

(c) Amplitude sweeps, AS3 (*Orange*) and AS4 (*Green*) at T = 37 °C, $\omega = 1$ rad/s and with a strain going from 0.01 to 100% (solid lines) and from 100 to 0.01% (dotted lines). Circles stand for G' and stars for G".

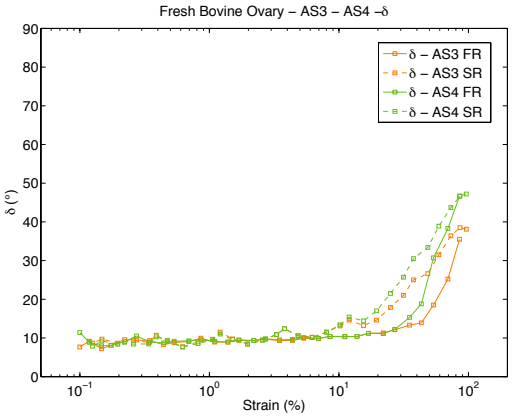

(d) Amplitude sweeps, AS3 (*Orange*) and AS4 (*Green*) at T = 37 °C, $\omega = 1$ rad/s and with a strain going from 0.01 to 100% (solid lines) and from 100 to 0.01% (dotted lines). Squares stand for δ.

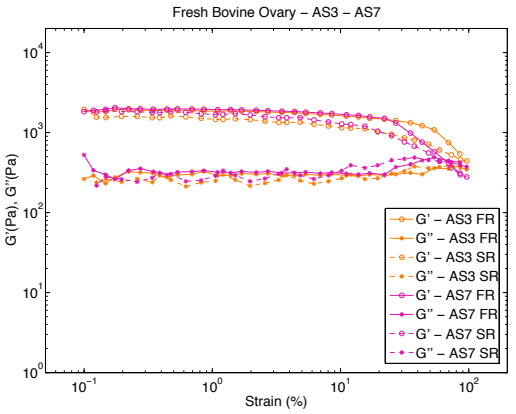

(e) Amplitude sweeps, AS3 (*Orange*) and AS7 (*Pink*) at T = 37 °C, $\omega = 1$ rad/s and with a strain going from 0.01 to 100% (solid lines) and from 100 to 0.01% (dotted lines). Circles stand for G' and stars for G".

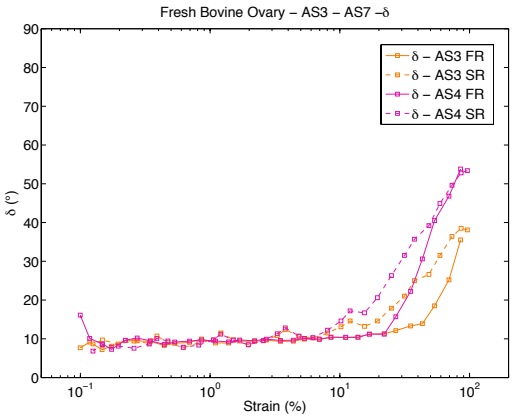

(f) Amplitude sweeps, AS3 (*Orange*) and AS7 (*Pink*) at T = 37 °C, $\omega = 1$ rad/s and with a strain going from 0.01 to 100% (solid lines) and from 100 to 0.01% (dotted lines). Squares stand for δ.

Figure 2: Rheological results for a sample of fresh bovine ovarian cortex.

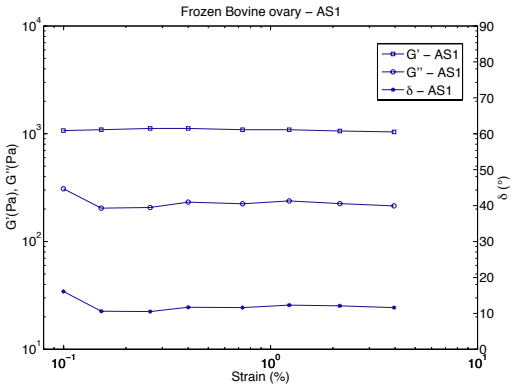

(a) Amplitude sweep at T =37 °C, $\omega = 1$ rad/s and with a strain going from 0.1 to 4%.

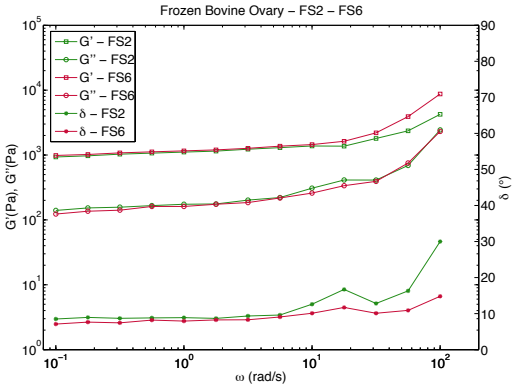

(b) Frequency sweeps, FS2 (*Green*) and FS6 (*Red*) at T = 37 °C, $\gamma = 0.4\%$ and ω = 100-0.1 rad/s. Squares stand for G', circles for G" and stars for δ.

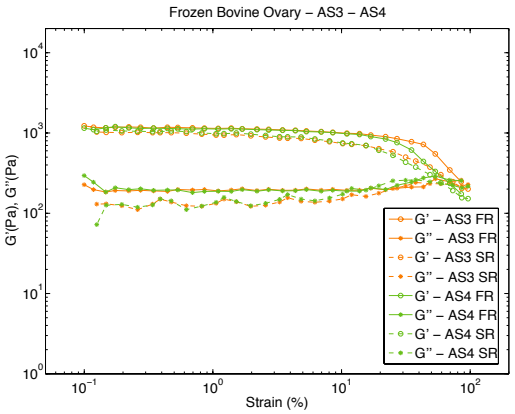

(c) Amplitude sweeps, AS3 (*Orange*) and AS4 (*Green*) at T = 37 °C, $\omega = 1$ rad/s and with a strain going from 0.01 to 100% (solid lines) and from 100 to 0.01% (dotted lines). Circles stand for G' and stars for G".

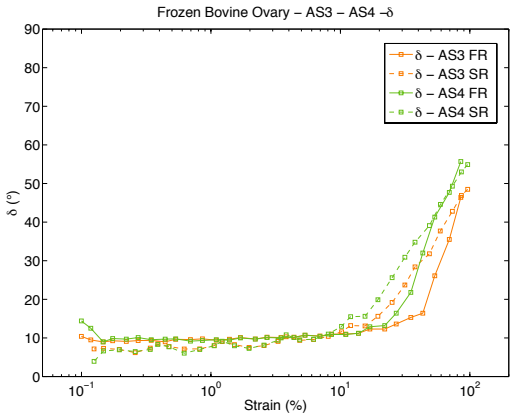

(d) Amplitude sweeps, AS3 (*Orange*) and AS4 (*Green*) at T = 37 °C, $\omega = 1$ rad/s and with a strain going from 0.01 to 100% (solid lines) and from 100 to 0.01% (dotted lines). Squares stand for δ.

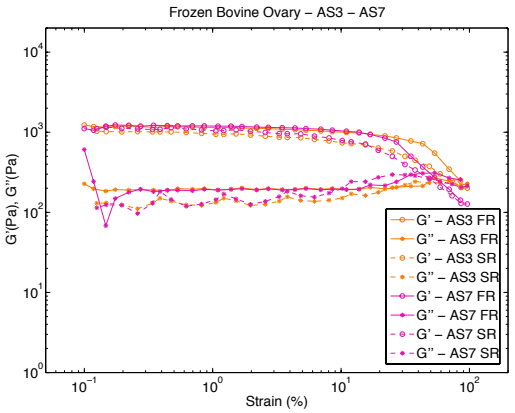

(e) Amplitude sweeps, AS3 (*Orange*) and AS7 (*Pink*) at T = 37 °C, $\omega = 1$ rad/s and with a strain going from 0.01 to 100% (solid lines) and from 100 to 0.01% (dotted lines). Circles stand for G' and stars for G".

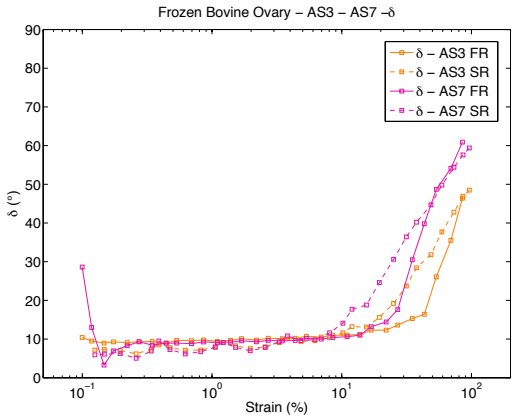

(f) Amplitude sweeps, AS3 (*Orange*) and AS7 (*Pink*) at T = 37 °C, $\omega = 1$ rad/s and with a strain going from 0.01 to 100% (solid lines) and from 100 to 0.01% (dotted lines). Squares stand for δ.

Figure 3: Rheological results for a sample of frozen bovine ovarian cortex.

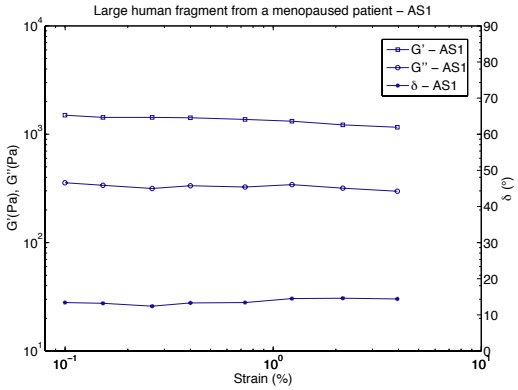

(a) Amplitude sweep at T =37 °C, $\omega = 1$ rad/s and with a strain going from 0.1 to 4%.

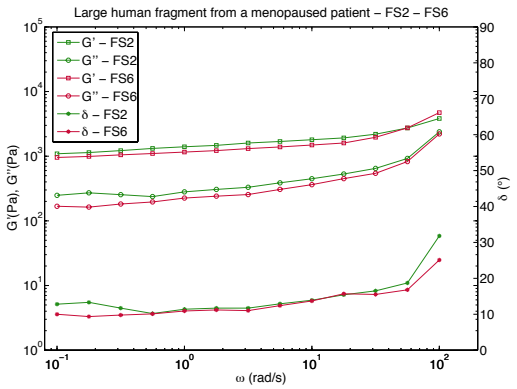

(b) Frequency sweeps, FS2 (*Green*) and FS6 (*Red*) at T = 37 °C, $\gamma = 0.4\%$ and ω = 100-0.1 rad/s. Squares stand for G', circles for G" and stars for δ.

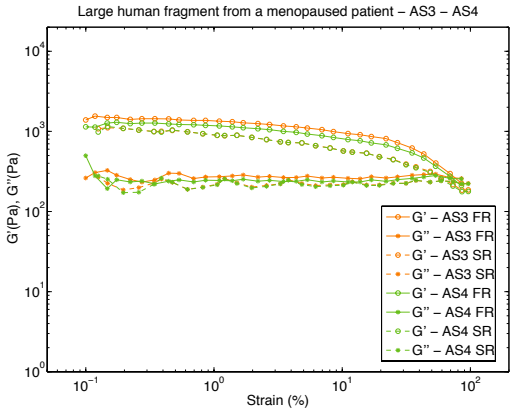

(c) Amplitude sweeps, AS3 (*Orange*) and AS4 (*Green*) at T = 37 °C, $\omega = 1$ rad/s and with a strain going from 0.01 to 100% (solid lines) and from 100 to 0.01% (dotted lines). Circles stand for G' and stars for G".

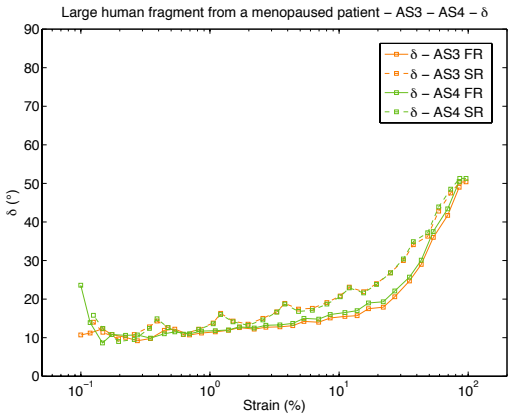

(d) Amplitude sweeps, AS3 (*Orange*) and AS4 (*Green*) at T = 37 °C, $\omega = 1$ rad/s and with a strain going from 0.01 to 100% (solid lines) and from 100 to 0.01% (dotted lines). Squares stand for δ.

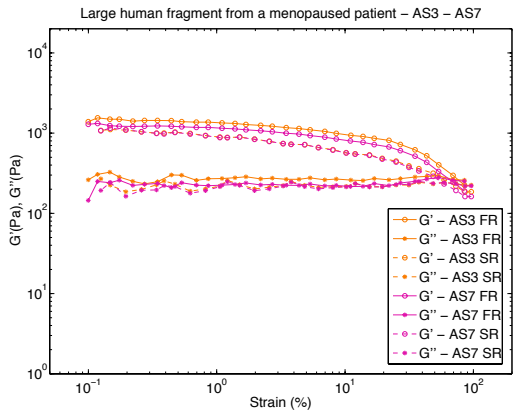

(e) Amplitude sweeps, AS3 (*Orange*) and AS7 (*Pink*) at T = 37 °C, $\omega = 1$ rad/s and with a strain going from 0.01 to 100% (solid lines) and from 100 to 0.01% (dotted lines). Circles stand for G' and stars for G".

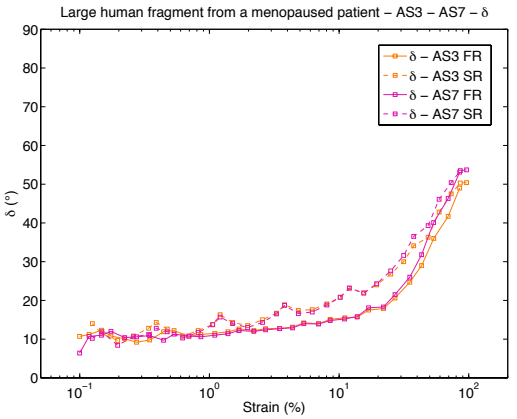

(f) Amplitude sweeps, AS3 (*Orange*) and AS7 (*Pink*) at T = 37 °C, $\omega = 1$ rad/s and with a strain going from 0.01 to 100% (solid lines) and from 100 to 0.01% (dotted lines). Squares stand for δ.

Figure 4: Rheological results of a large sample of human ovarian cortex from a menopaused patient.

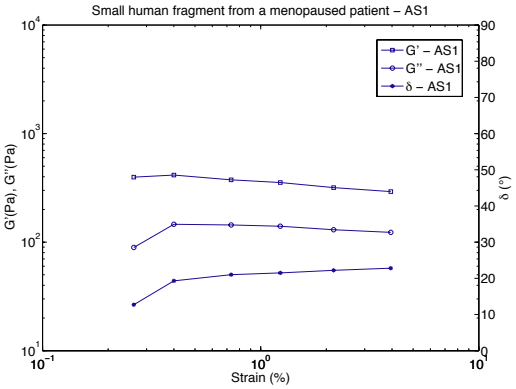

(a) Amplitude sweep at T =37 °C, $\omega = 1$ rad/s and with a strain going from 0.1 to 4%.

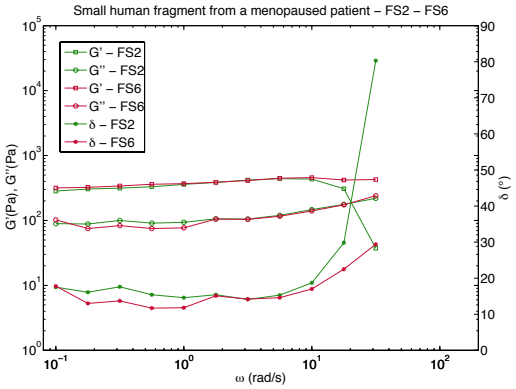

(b) Frequency sweeps, FS2 (*Green*) and FS6 (*Red*) at T = 37 °C, $\gamma = 0.4\%$ and ω = 100-0.1 rad/s. Squares stand for G', circles for G" and stars for δ.

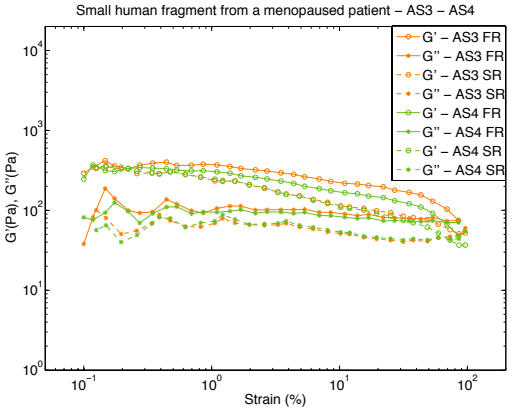

(c) Amplitude sweeps, AS3 (*Orange*) and AS4 (*Green*) at T = 37 °C, $\omega = 1$ rad/s and with a strain going from 0.01 to 100% (solid lines) and from 100 to 0.01% (dotted lines). Circles stand for G' and stars for G".

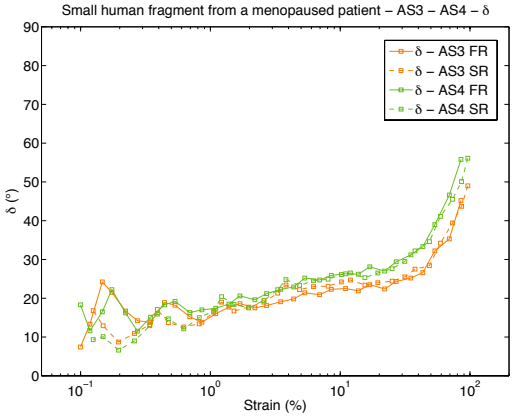

(d) Amplitude sweeps, AS3 (*Orange*) and AS4 (*Green*) at T = 37 °C, $\omega = 1$ rad/s and with a strain going from 0.01 to 100% (solid lines) and from 100 to 0.01% (dotted lines). Squares stand for δ.

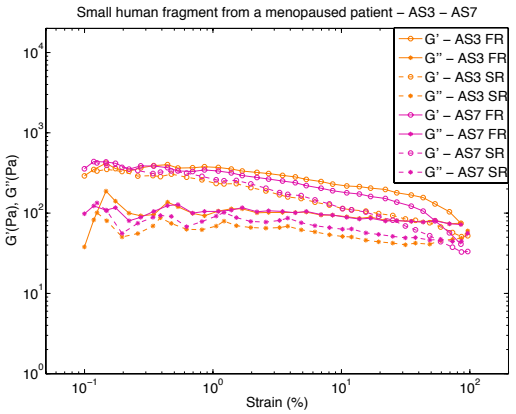

(e) Amplitude sweeps, AS3 (*Orange*) and AS7 (*Pink*) at T = 37 °C, $\omega = 1$ rad/s and with a strain going from 0.01 to 100% (solid lines) and from 100 to 0.01% (dotted lines). Circles stand for G' and stars for G".

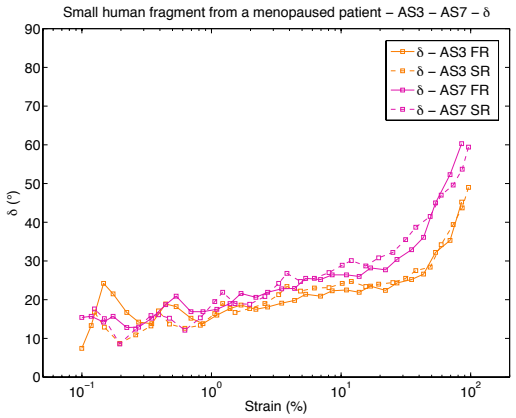

(f) Amplitude sweeps, AS3 (*Orange*) and AS7 (*Pink*) at T = 37 °C, $\omega = 1$ rad/s and with a strain going from 0.01 to 100% (solid lines) and from 100 to 0.01% (dotted lines). Squares stand for δ.

Figure 5: Rheological results of a small sample of human ovarian cortex from a menopaused patient.

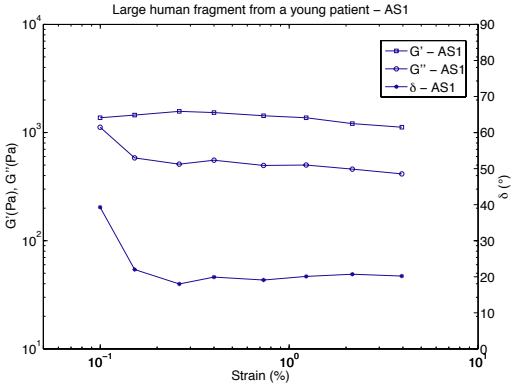

(a) Amplitude sweep at T =37 °C, $\omega = 1$ rad/s and with a strain going from 0.1 to 4%.

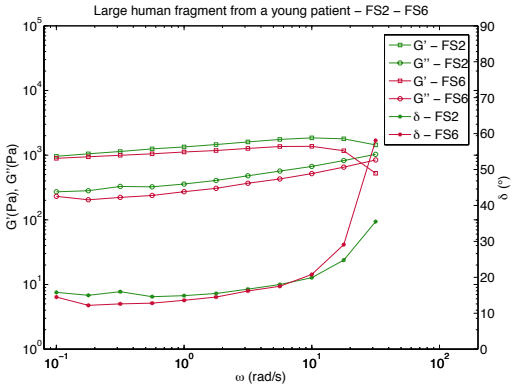

(b) Frequency sweeps, FS2 (*Green*) and FS6 (*Red*) at T = 37 °C, $\gamma = 0.3\%$ and ω = 100-0.1 rad/s. Squares stand for G', circles for G" and stars for δ.

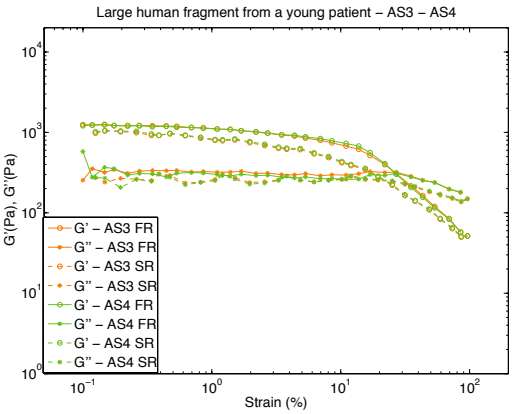

(c) Amplitude sweeps, AS3 (*Orange*) and AS4 (*Green*) at T = 37 °C, $\omega = 1$ rad/s and with a strain going from 0.01 to 100% (solid lines) and from 100 to 0.01% (dotted lines). Circles stand for G' and stars for G".

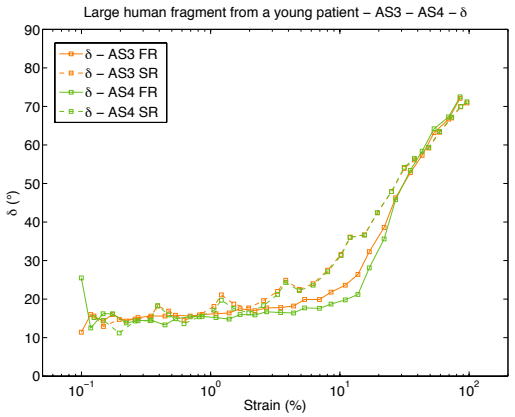

(d) Amplitude sweeps, AS3 (*Orange*) and AS4 (*Green*) at T = 37 °C, $\omega = 1$ rad/s and with a strain going from 0.01 to 100% (solid lines) and from 100 to 0.01% (dotted lines). Squares stand for δ.

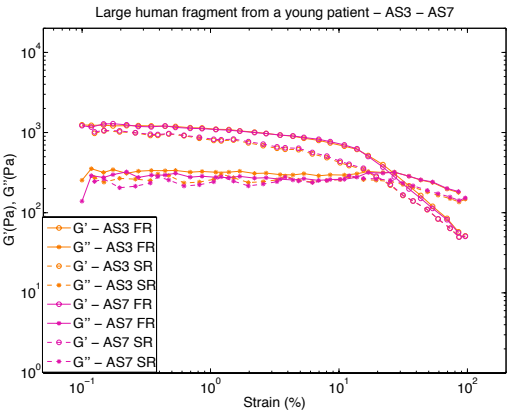

(e) Amplitude sweeps, AS3 (*Orange*) and AS7 (*Pink*) at T = 37 °C, $\omega = 1$ rad/s and with a strain going from 0.01 to 100% (solid lines) and from 100 to 0.01% (dotted lines). Circles stand for G' and stars for G".

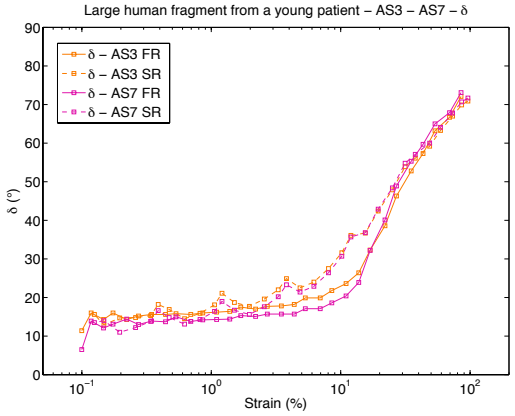

(f) Amplitude sweeps, AS3 (*Orange*) and AS7 (*Pink*) at T = 37 °C, $\omega = 1$ rad/s and with a strain going from 0.01 to 100% (solid lines) and from 100 to 0.01% (dotted lines). Squares stand for δ.

Figure 6: Rheological results of a large sample of human ovarian cortex from a young patient.

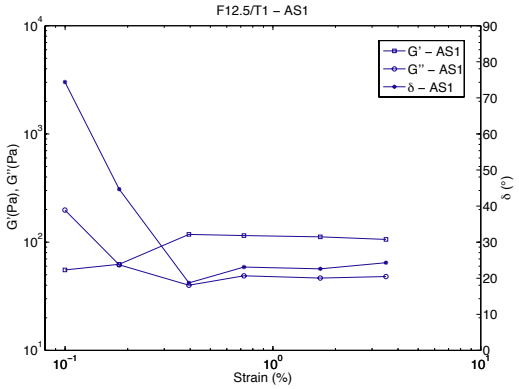

(a) Amplitude sweep at T =37 °C, $\omega = 1$ rad/s and with a strain going from 0.1 to 3.5%.

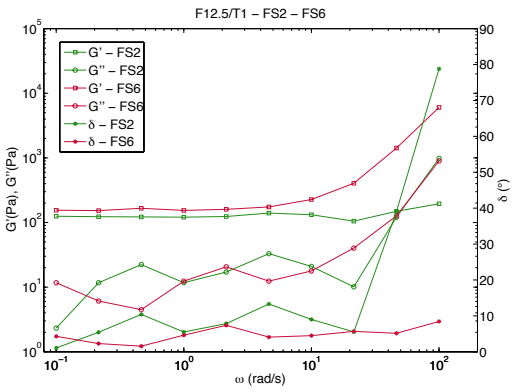

(b) Frequency sweeps, FS2 (*Green*) and FS6 (*Red*) at T = 37 °C, $\gamma = 0.4\%$ and ω = 100-0.1 rad/s. Squares stand for G', circles for G" and stars for δ.

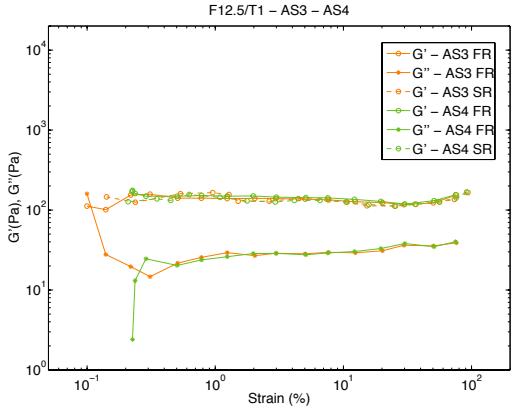

(c) Amplitude sweeps, AS3 (*Orange*) and AS4 (*Green*) at T = 37 °C, $\omega = 1$ rad/s and with a strain going from 0.01 to 100% (solid lines) and from 100 to 0.01% (dotted lines). Circles stand for G' and stars for G".

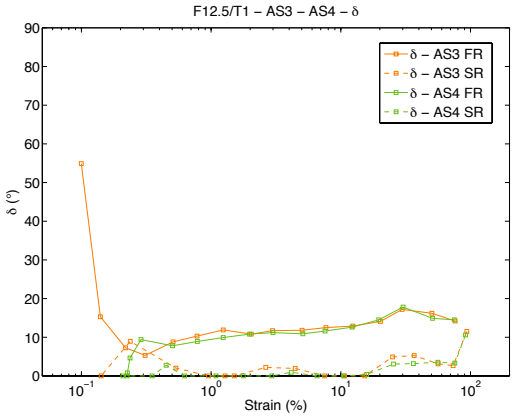

(d) Amplitude sweeps, AS3 (*Orange*) and AS4 (*Green*) at T = 37 °C, $\omega = 1$ rad/s and with a strain going from 0.01 to 100% (solid lines) and from 100 to 0.01% (dotted lines). Squares stand for δ.

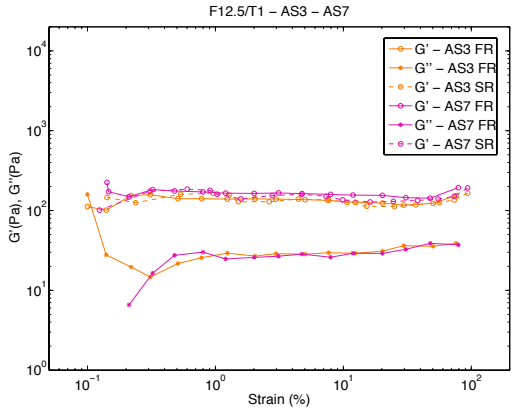

(e) Amplitude sweeps, AS3 (*Orange*) and AS7 (*Pink*) at T = 37 °C, $\omega = 1$ rad/s and with a strain going from 0.01 to 100% (solid lines) and from 100 to 0.01% (dotted lines). Circles stand for G' and stars for G".

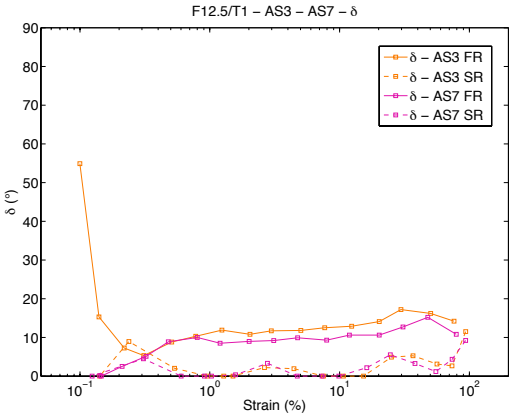

(f) Amplitude sweeps, AS3 (*Orange*) and AS7 (*Pink*) at T = 37 °C, $\omega = 1$ rad/s and with a strain going from 0.01 to 100% (solid lines) and from 100 to 0.01% (dotted lines). Squares stand for δ.

Figure 7: Rheological results for F12.5/T1. G" SR for AS3, AS4 and AS7 have been hidden due to their non physically possible shape, certainly caused by experimental noise.

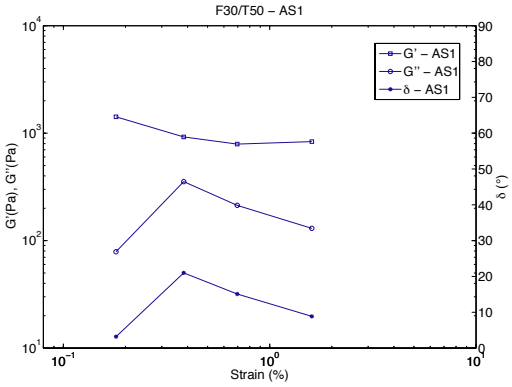

(a) Amplitude sweep at T =37 °C, $\omega = 1$ rad/s and with a strain going from 0.18 to 3.3%.

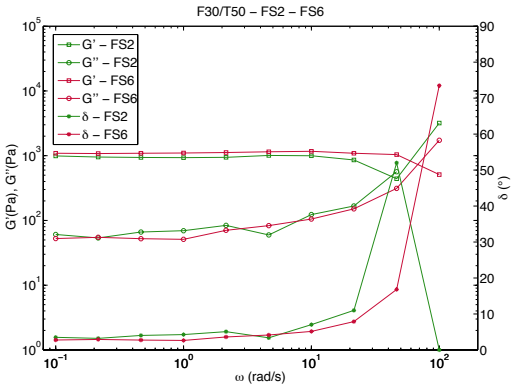

(b) Frequency sweeps, FS2 (*Green*) and FS6 (*Red*) at T = 37 °C, $\gamma = 0.4\%$ and ω = 100-0.1 rad/s. Squares stand for G', circles for G" and stars for δ.

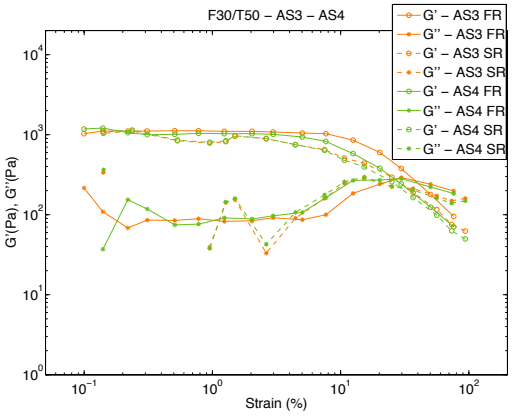

(c) Amplitude sweeps, AS3 (*Orange*) and AS4 (*Green*) at T = 37 °C, $\omega = 1$ rad/s and with a strain going from 0.01 to 100% (solid lines) and from 100 to 0.01% (dotted lines). Circles stand for G' and stars for G".

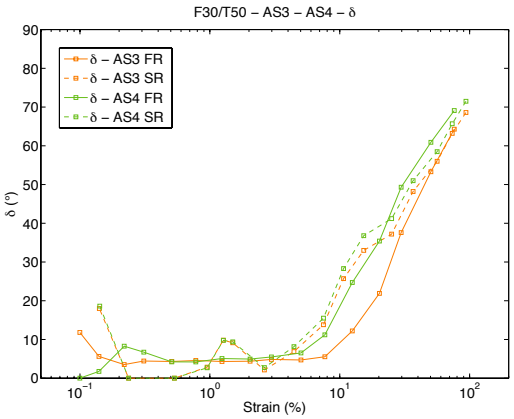

(d) Amplitude sweeps, AS3 (*Orange*) and AS4 (*Green*) at T = 37 °C, $\omega = 1$ rad/s and with a strain going from 0.01 to 100% (solid lines) and from 100 to 0.01% (dotted lines). Squares stand for δ.

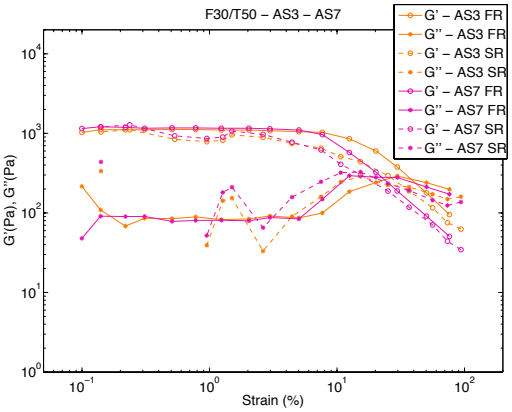

(e) Amplitude sweeps, AS3 (*Orange*) and AS7 (*Pink*) at T = 37 °C, $\omega = 1$ rad/s and with a strain going from 0.01 to 100% (solid lines) and from 100 to 0.01% (dotted lines). Circles stand for G' and stars for G".

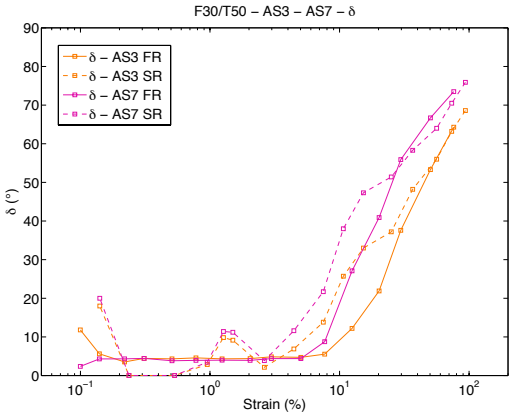

(f) Amplitude sweeps, AS3 (*Orange*) and AS7 (*Pink*) at T = 37 °C, $\omega = 1$ rad/s and with a strain going from 0.01 to 100% (solid lines) and from 100 to 0.01% (dotted lines). Squares stand for δ.

Figure 8: Rheological results for F30/T50.

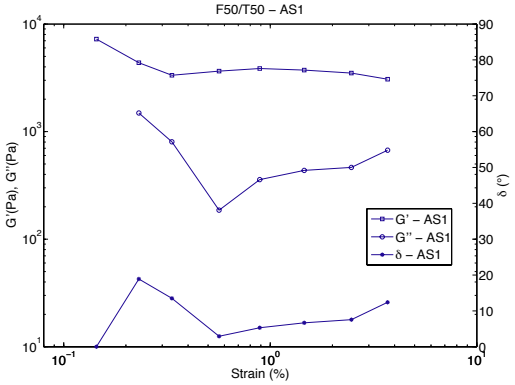

(a) Amplitude sweep at T =37 °C, $\omega = 1$ rad/s and with a strain going from 0.15 to 4%.

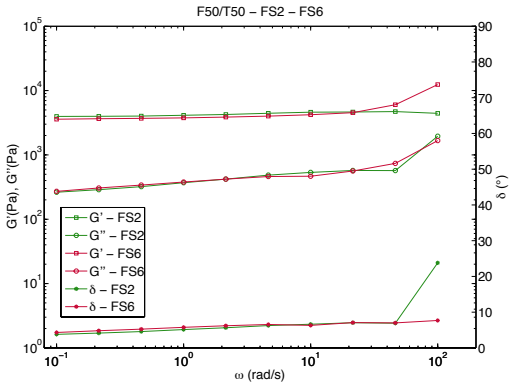

(b) Frequency sweeps, FS2 (*Green*) and FS6 (*Red*) at T = 37 °C, $\gamma = 0.4\%$ and ω = 100-0.1 rad/s. Squares stand for G', circles for G" and stars for δ.

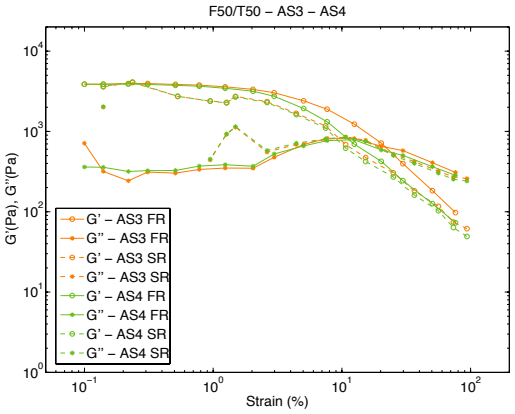

(c) Amplitude sweeps, AS3 (*Orange*) and AS4 (*Green*) at T = 37 °C, $\omega = 1$ rad/s and with a strain going from 0.01 to 100% (solid lines) and from 100 to 0.01% (dotted lines). Circles stand for G' and stars for G".

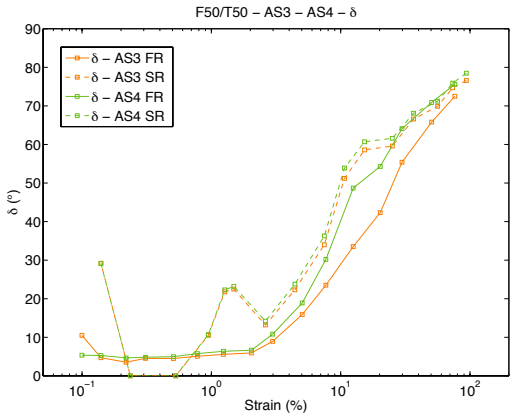

(d) Amplitude sweeps, AS3 (*Orange*) and AS4 (*Green*) at T = 37 °C, $\omega = 1$ rad/s and with a strain going from 0.01 to 100% (solid lines) and from 100 to 0.01% (dotted lines). Squares stand for δ.

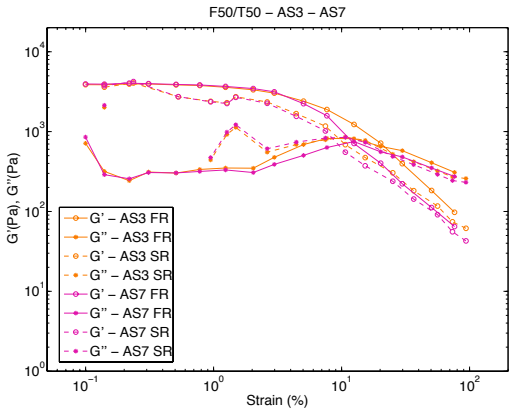

(e) Amplitude sweeps, AS3 (*Orange*) and AS7 (*Pink*) at T = 37 °C, $\omega = 1$ rad/s and with a strain going from 0.01 to 100% (solid lines) and from 100 to 0.01% (dotted lines). Circles stand for G' and stars for G".

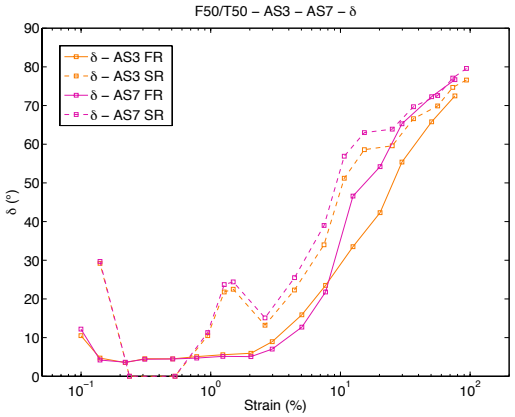

(f) Amplitude sweeps, AS3 (*Orange*) and AS7 (*Pink*) at T = 37 °C, $\omega = 1$ rad/s and with a strain going from 0.01 to 100% (solid lines) and from 100 to 0.01% (dotted lines). Squares stand for δ.

Figure 9: Rheological results for F50/T50.

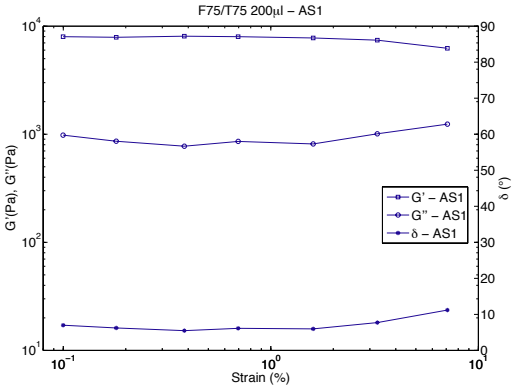

(a) Amplitude sweep at T =37 °C, $\omega = 1$ rad/s and with a strain going from 0.1 to 7%.

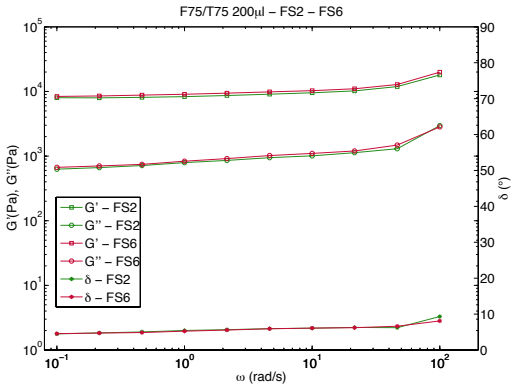

(b) Frequency sweeps, FS2 (*Green*) and FS6 (*Red*) at T = 37 °C, $\gamma = 0.4\%$ and ω = 100-0.1 rad/s. Squares stand for G', circles for G" and stars for δ.

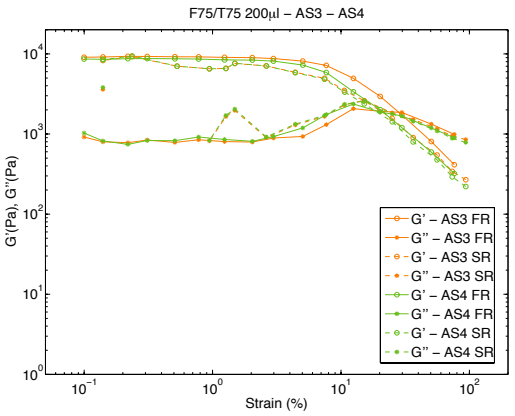

(c) Amplitude sweeps, AS3 (*Orange*) and AS4 (*Green*) at T = 37 °C, $\omega = 1$ rad/s and with a strain going from 0.01 to 100% (solid lines) and from 100 to 0.01% (dotted lines). Circles stand for G' and stars for G".

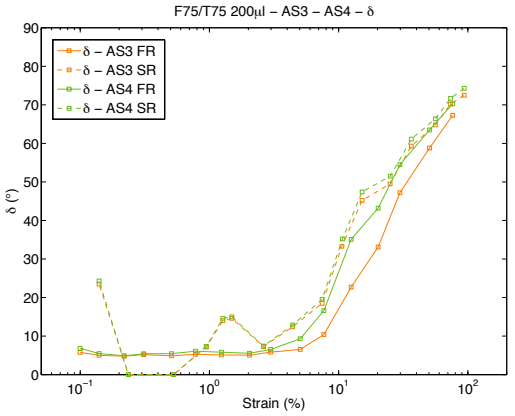

(d) Amplitude sweeps, AS3 (*Orange*) and AS4 (*Green*) at T = 37 °C, $\omega = 1$ rad/s and with a strain going from 0.01 to 100% (solid lines) and from 100 to 0.01% (dotted lines). Squares stand for δ.

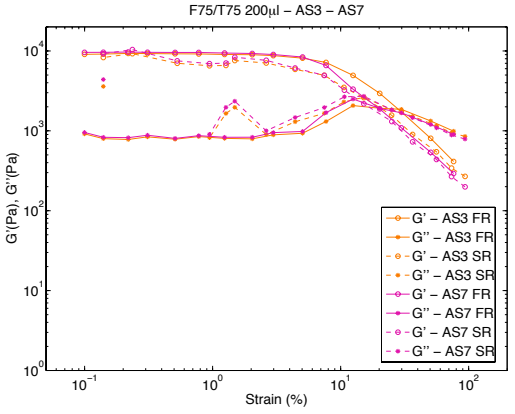

(e) Amplitude sweeps, AS3 (*Orange*) and AS7 (*Pink*) at T = 37 °C, $\omega = 1$ rad/s and with a strain going from 0.01 to 100% (solid lines) and from 100 to 0.01% (dotted lines). Circles stand for G' and stars for G".

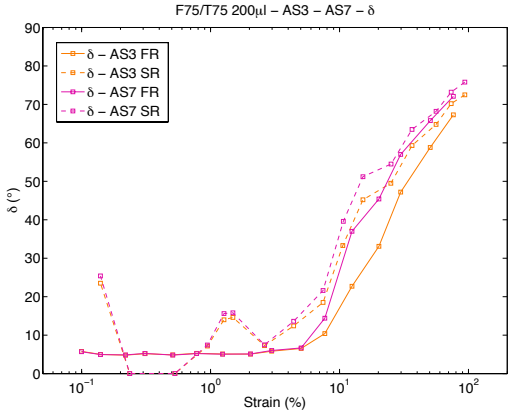

(f) Amplitude sweeps, AS3 (*Orange*) and AS7 (*Pink*) at T = 37 °C, $\omega = 1$ rad/s and with a strain going from 0.01 to 100% (solid lines) and from 100 to 0.01% (dotted lines). Squares stand for δ.

Figure 10: Rheological results for F75/T75, 200 μl.

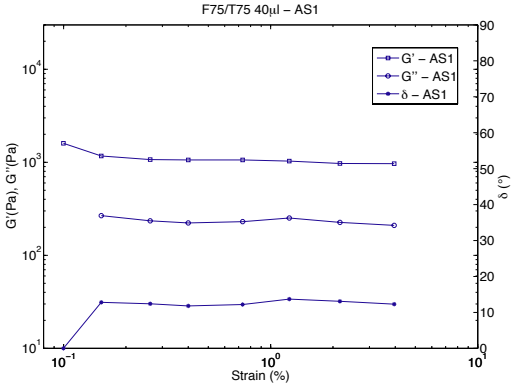

(a) Amplitude sweep at T =37 °C, $\omega = 1$ rad/s and with a strain going from 0.1 to 4%.

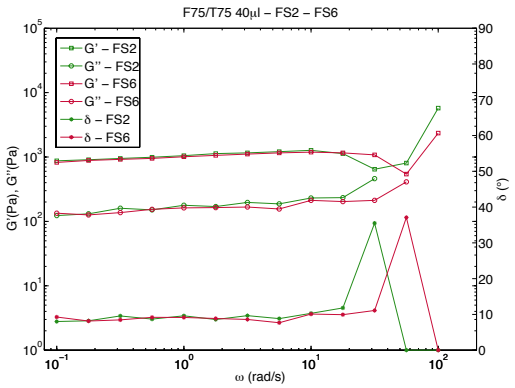

(b) Frequency sweeps, FS2 (*Green*) and FS6 (*Red*) at T = 37 °C, $\gamma = 0.4\%$ and ω = 100-0.1 rad/s. Squares stand for G', circles for G" and stars for δ.

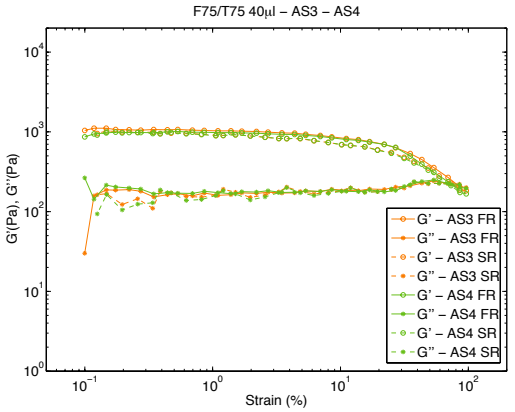

(c) Amplitude sweeps, AS3 (*Orange*) and AS4 (*Green*) at T = 37 °C, $\omega = 1$ rad/s and with a strain going from 0.01 to 100% (solid lines) and from 100 to 0.01% (dotted lines). Circles stand for G' and stars for G".

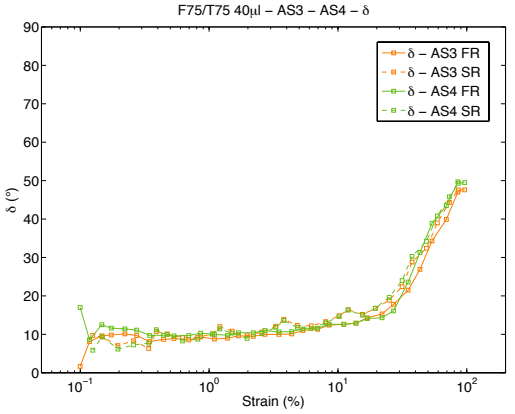

(d) Amplitude sweeps, AS3 (*Orange*) and AS4 (*Green*) at T = 37 °C, $\omega = 1$ rad/s and with a strain going from 0.01 to 100% (solid lines) and from 100 to 0.01% (dotted lines). Squares stand for δ.

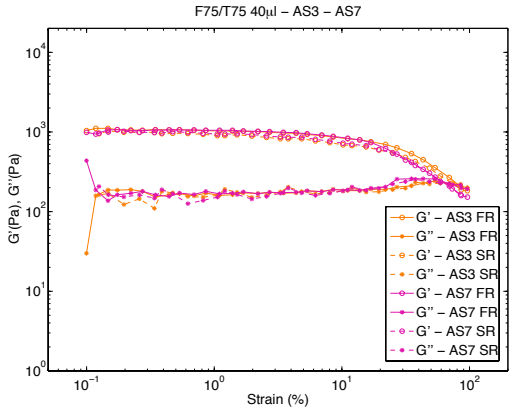

(e) Amplitude sweeps, AS3 (*Orange*) and AS7 (*Pink*) at T = 37 °C, $\omega = 1$ rad/s and with a strain going from 0.01 to 100% (solid lines) and from 100 to 0.01% (dotted lines). Circles stand for G' and stars for G".

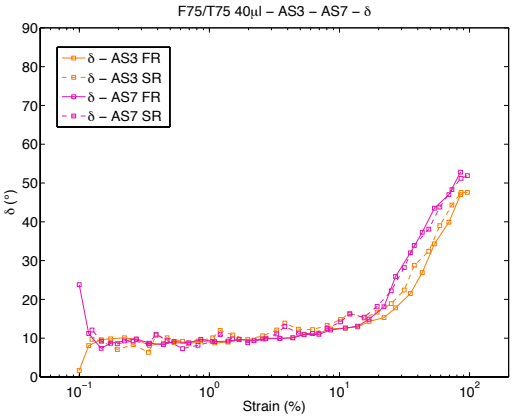

(f) Amplitude sweeps, AS3 (*Orange*) and AS7 (*Pink*) at T = 37 °C, $\omega = 1$ rad/s and with a strain going from 0.01 to 100% (solid lines) and from 100 to 0.01% (dotted lines). Squares stand for δ.

Figure 11: Rheological results for F75/T75, 40 μl.

Rue Archimède, 1 bte L6.11.01, 1348 Louvain-la-Neuve **www.uclouvain.be/epl**